QUANTIFYING THE URCA COOLING IMPACT OF MASS 61 NUCLEI IN X-RAY BURSTING SYSTEMS

By

Wei Jia Ong

A DISSERTATION

Submitted to
Michigan State University
in partial fulfillment of the requirements
for the degree of

Physics — Doctor of Philosophy

2018

ABSTRACT

QUANTIFYING THE URCA COOLING IMPACT OF MASS 61 NUCLEI IN X-RAY BURSTING SYSTEMS

By

Wei Jia Ong

Early-time observations of cooling crusts of neutron stars in Quasi-persistent X-ray transients cannot be explained by current astrophysical models, suggesting an incomplete understanding of the physical and nuclear processes that occur in the crust. An as yet unidentified strong, shallow heat source has been postulated to account for these discrepancies. Complicating this issue is the recent discovery of Urca cooling, β decay-electron capture cycles that release neutrinos, in neutron star crusts. The strength of Urca cooling depends critically on the magnitude of the ground state to ground state transition between the parent-daughter pair, because the electron degeneracy under neutron star crustal conditions forbids β decay transitions to excited states. Current predictions of Urca cooling in neutron star crusts are highly reliant on theoretical QRPA predictions. Experimental data are needed to test these predictions and characterise their uncertainties. Of particular importance is the possible existence of strong ground state to ground state electron capture and β decay transitions, and the strength of these transitions.

This work reports an experimental measurement of the transition strength for the β decay of the ground state of ^{61}V to states in ^{61}Cr. Most importantly, the ground state to ground state transition strength was determined to be $7.4^{+13.8}_{-5.8}$% (corresponding to a log ft value of $5.5^{+0.8}_{-0.6}$). This result confirms the existence of a considerable ground state to ground state transition that enables Urca cycle cooling in accreted neutron star crusts at the boundary of the ^{61}Cr and ^{61}V layers. However, the log ft value is significantly larger

than the theoretically predicted log ft value of 4.35, resulting in a slower than expected Urca cycle. This result was achieved through the measurement of the β-delayed γ rays using the total absorption spectrometer SuN and the measurement of the β-delayed neutron branch using the neutron long counter system NERO at the National Superconducting Cyclotron Laboratory (NSCL) at Michigan State University. The use of the combination of SuN and NERO helps to mitigate the impact of the Pandemonium effect that tends to significantly skew studies using more traditional high-resolution, low-efficiency detectors.

The impact of this experimental result on the cooling strength of the A = 61 mass chain was investigated using a nucleosynthesis network evolved under neutron star crustal conditions. The results show that the mass 61 chain is amongst the strongest cooling chains in crusts composed of X-ray burst ashes. Updated cooling strengths using the latest state of experimental knowledge were also folded over realistic crust compositions for X-ray bursting systems to identify other strong cooling chains, as well as to pinpoint Urca pairs of particular interest for future studies using the same technique as developed in this work.

In memory of Frank and Ernst, without whom I would never have begun this journey.

ACKNOWLEDGMENTS

There is a proverb that says that it takes a village to raise a child, and the same can be said about completing a PhD- Thank you to everyone who played a role in helping me throughout graduate school, no matter how small. I unfortunately cannot name everyone here, but please know I sincerely appreciate your time and help. Thanks must go out to everyone who keep the lab running, and who help to make experiments happen.

I must especially thank my advisor Hendrik Schatz, who was an incredible mentor to me. He constantly challenges me to be a better scientist, and his guidance helps me to become a better one. I can only hope that I do not disappoint him too much. I would also like to thank members of Team Schatz, in particular: Christoph Langer, for his patience and mentorship during my first years in graduate school; Fernando Montes, for many interesting conversations and for his invaluable help preparing for my thesis experiment; Zach Meisel, for being an outstanding example to a younger graduate student (I learnt my backronym skills from the very best); as well as "Cowboy" Tony Ahn, Konrad Schmidt, Jin Shilun, Justin Browne, and Sara Ayoub for making the lab a fun and welcoming place to work.

I am also grateful to the members of my committee: Artemis Spyrou, who served as a semi-advisor and who also did her best to ensure my well-being as a graduate student; Alexandra Gade, with whom I was able to discuss scientific topics of any kind and whose unrelenting work ethic always inspired me to work harder; Ed Brown, for his extraordinarily clear explanations of any question I had for him, no matter how silly, and his constant encouragement; and Carl Schmidt, for being a kind and patient teacher to a young graduate student.

Thanks also to: members of the SuN and Beta groups, especially Professor Sean Liddick

and Alexander Dombos, for their help preparing for my experiment and with my analysis; Professor Vladimir Zelevinsky for always letting me bounce ideas off him and for not laughing at them; Jill Berryman and Carol Lentz for being good listeners and even better friends.

I have been very lucky throughout graduate school to have the support of amazing friends. Amy "Bear Hunter" Lovell and "Becky" Lewis, whom I cannot thank enough for their friendship. I would not have been able to do this without them. Thanks for all the fun cooking/baking and football days, and for providing surrogate (if competing) teams to cheer for when the Rams abandoned St Louis. Josh "Brad" Bradt and Chris "no relation to Tom" Izzo, for their great company and senses of humour. Walter Buhro, who made me a better person. Juan Manfredi, Katie Childers, Zach "Batman" Matheson and other transient residents of office 1022, for being the very best officemates and fellow Guardians of the Sign I could ask for. To the lovely Nanyang girls who've had my back for more than a decade, you guys are the best, most enthusiastic cheer squad ever.

I have to thank Christine Floss, whose encouragement kept me going even when I was struggling the most, and who always opened her home to me when I needed somewhere to go.

Finally, none of this would have been possible without the support and love of my family. Mum, Dad, 大姐, 二姐, and Brian, thanks for always believing in me and for helping me chase my dreams. As mum loves to say: "~~吃饱饭，没事做。~~ 船到桥头自然直。"

TABLE OF CONTENTS

LIST OF TABLES

LIST OF FIGURES

Chapter 1

Introduction

1.1 Neutron Stars

Neutron stars are compact stellar objects which are formed when the core of an evolved star implodes. With masses of $\sim 1 M_{\odot}$ and radii of $\sim$10km, they have densities roughly equivalent to a billion tonnes per teaspoon, and are thus good laboratories for the way that nuclear material behaves at extreme densities. Neutron stars can be partitioned into layers (Fig. 1.1). The outermost layer of a neutron star is the neutron star atmosphere, which is on the order of a centimetre thick, where the atmospheric material behaves like a gas and there are no correlations between nuclei. Below the atmosphere is the envelope, which behaves like an ideal gas. Further beneath is the ocean where densities are sufficient such that the behaviour of a nucleus is correlated with other nuclei in close proximity to it. Deeper still is the outer crust, in which nuclei exist in a solid lattice with a Fermi gas of degenerate, relativistic electrons that provides most of the pressure supporting the crust against gravitational collapse. As the neutron-richness of the material increases, eventually the extra neutrons cannot bind to the nuclear matter. This is known as neutron drip, and marks the transition of the outer crust to the inner crust. In the inner crust, the neutron pressure exceeds the electron pressure (since the number density of neutrons is much higher at this point than the electron number density) and becomes the dominant resistance against

gravitational collapse. The crust-core transition occurs when the density is $\sim$0.08 nucleons per fm^3 (where 1fm = 10^{-15}m), about half of nuclear saturation density. The state of matter of the inner core of the neutron star is still unknown, and what the equation of state is that governs it is one of the biggest open questions in nuclear physics.

Quasi-persistent transients are a subset of observed neutron stars that exist in low-mass X-ray binaries (LMXBs). They are characterised by particularly long outburst periods powered by accretion from their companion star where their X-ray luminosities are on the order of 10^{37} erg/s, followed by a similarly long quiescent phase where the X-ray luminosity drops many orders of magnitude. It is hypothesised that the transition from the accreting phase to the quiescent phase occurs when the accretion from the companion star slows to a negligible level or stops completely [1, 2]. The mechanism responsible for this accretion turn-off is not yet fully understood, but it is the most likely physical reason for the large drop in X-ray luminosity. As material accumulates on the neutron star surface during the accretion phase, it undergoes nuclear burning. Depending on the accretion rate, the nuclear burning can potentially be unstable, where a layer of fuel accumulates for hours to days before it burns explosively within 10-100s, causing an observable X-ray burst [3]. Burst luminosities can reach 10^{38} erg/s, which is observed on top of the persistent X-ray flux generated by the release of gravitational energy by infalling material during accretion.

X-ray bursts are caused by a thermonuclear runaway where the temperature sensitivity of the nuclear reaction rates leads to an increase in energy production when temperatures increase, creating a positive feedback loop. The thermonuclear runaway is triggered when it becomes hot and dense enough for the 3α reaction to ignite and for breakout from the CNO cycle through the $^{15}\mathrm{O}(\alpha,\gamma)^{19}\mathrm{F}$ reaction to occur. This then triggers the (α, p) and (p, γ) reactions which dominate the rise of the X-ray flux up to the peak of the X-ray

light curve, producing elements in the intermediate mass range ($A \sim 40$). At this point, the Coulomb barrier becomes too high for α-induced reactions to be fast even for the hot and dense conditions of the burning material, and the rapid proton capture process (rp-process) becomes the dominant source of energy powering the X-ray lightcurve [4, 5]. The rp-process is characterised by a series of fast proton captures and slower β decays, with a reaction flow near or at the proton drip line. Depending on the conditions of the burst, it predominantly produces nuclei in the mass $A \sim 60$–70 range, potentially up to Tellurium, Tin and Antimony [5]. These ashes will be pushed down into the ocean and then the crust under the weight of continued accretion, and replaces the ocean and crust completely. Thus, understanding the ashes of the bursting phase nucleosynthesis is important for a correct determination of the properties of the neutron star ocean and crust.

During the accreting phase, the nuclear reactions heat the crust of the neutron star and bring it out of thermal equilibrium with the core. During the quiescent phase, when accretion has 'turned off', the star cools through neutrino and radiative emission. The surface luminosity as a function of time of the neutron star, known as the cooling curve, probes the thermal structure of the crust at increasing depth as the crust cools. This is because the thermal relaxation time of the material depends on its matter properties and depth. At a given time, the thermal profile can be understood as two separate parts: the innermost material has not yet cooled, and its thermal character is essentially equivalent to the steady-state condition during the accretion phase. The outer part of the material has thermally relaxed and has an approximately constant outward flux. Therefore, a series of observations following the beginning of quiesence will probe increasingly deeper layers of the neutron star (Fig. 1.1). Observations of transient neutron stars present a unique opportunity to probe the inner layers of the neutron star crust because the cooling timescales are on the order of

years, as opposed to the expected thousands of years for the entire neutron star.

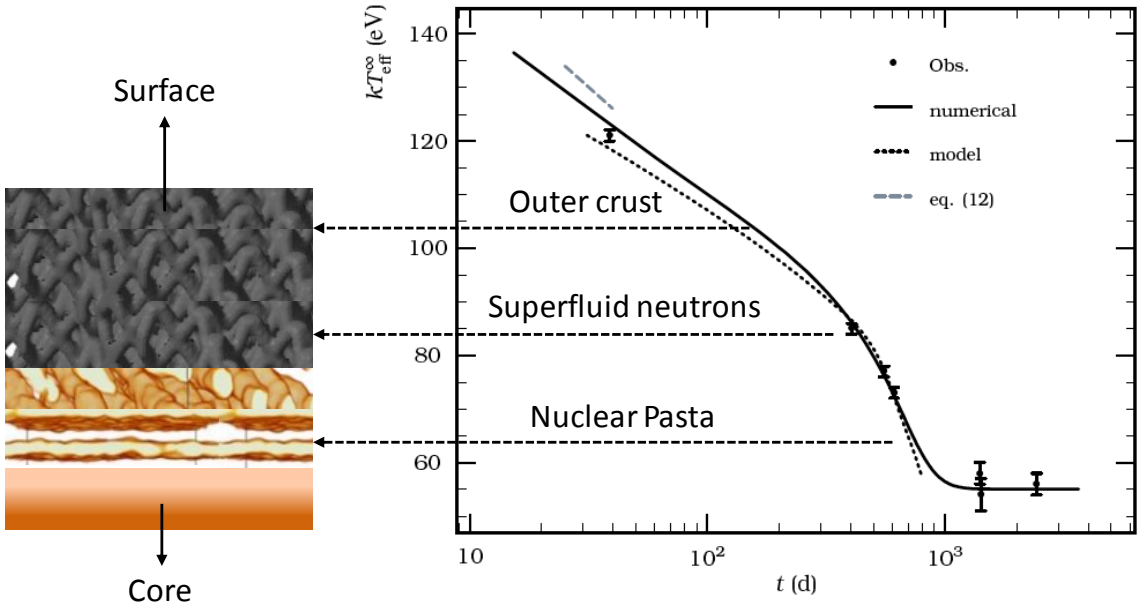

Figure 1.1: Left: Structure of a neutron star (layers not to scale) [6, 7]. Right: The light curve with the corresponding portion of the star that is probed. (Adapted from [8].)

1.2 Open questions in neutron star crustal physics

Several major mysteries remain that suggest our understanding of neutron star crust physics is incomplete. Present models of neutron star crust cooling systematically produce lower temperatures in the early stages of cooling, right after the beginning of quiescence [8, 9]. To produce temperatures consistent with observations, a shallow heat source is required. Though nuclear reactions in the neutron star crust do produce heat, it has been shown that the heat produced by nuclear reactions (further discussed in section 1.3) is insufficient in the most-observed quiescent quasi-persistent transients to explain the cooling profile [9].

Another big question is that of superburst ignition. Superbursts are similar to X-ray bursts but last for hours to days with a recurrance period of months to years. They are about three orders of magnitude more energetic than X-ray bursts (10^{42} ergs compared to

10^{39} ergs), and therefore cannot be the product of explosive He burning. Hence, superbursts are theorised to be powered by C burning [10]. Observed superburst light curves have constrained the superburst ignition depth to much shallower layers than neutron star crust models predict [11, 12], and require a shallow heat source (likely the same heat source that explains hotter-than-expected crusts discussed above) for ignition to occur at shallow depths.

Together with a sound understanding of the astrophysics of quasi-persistent transients, precise knowledge of the nuclear processes that heat and cool neutron star crusts is required to provide stringent constraints on the strength and origin of the shallow heat source, as well as superburst ignition. These nuclear processes are discussed in the following section.

1.3 Nuclear processes in neutron star crusts

Several nuclear heating processes can occur in the crust of neutron stars during the accretion phase when ashes of burning are pushed deeper into the star [13,14]. With increasing depth, the Fermi energy of the relativistic degenerate electrons becomes high enough for electron captures to occur on increasingly neutron-rich nuclei in the solid lattice. In even-A chains, due to the odd-even mass stagger, when the electron capture of A, Z (where Z is even) to $A, Z-1$ becomes energetically possible, the electron capture of $A, Z-1$ to $A, Z-2$ is also possible because $Q_{\rm EC}(A, Z \rightarrow A, Z-1)$ is larger than $Q_{\rm EC}(A, Z-1 \rightarrow A, Z-2)$. In the case shown in Fig. 1.2, the difference between the electron Fermi energy and the electron capture Q-value is shared between deposited heat ($\sim$25%) and the emitted neutrino ($\sim$75%) which carries its energy away. However, if there is an excited state in the $A, Z-2$ nucleus that is populated by the electron capture, heat deposition increases as all the energy from the electromagnetic de-excitation of the excited state is deposited as heat [14].

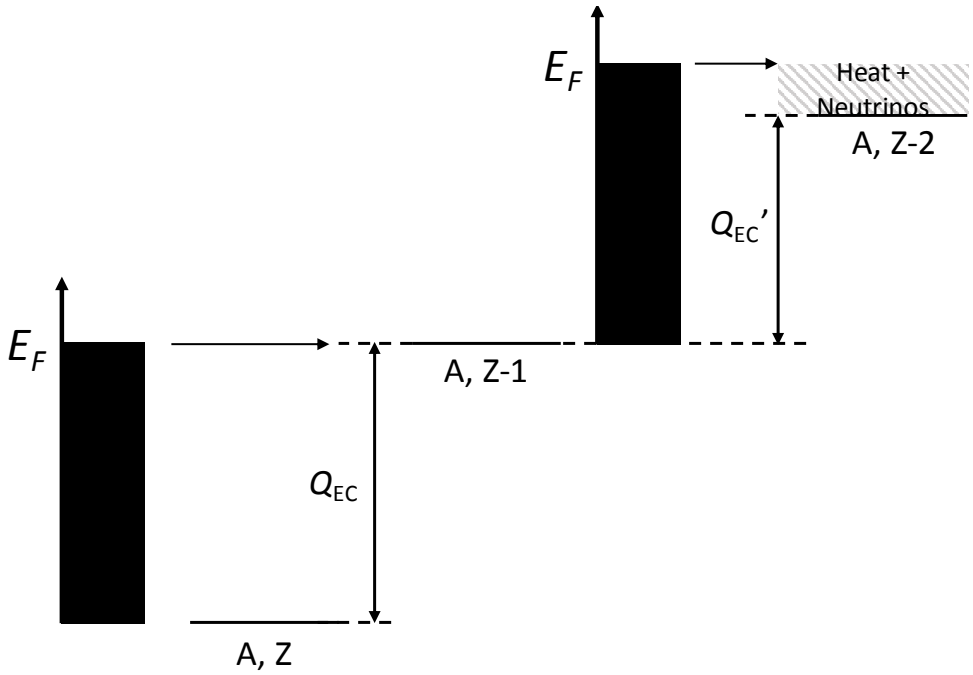

Figure 1.2: Cartoon showing the source of crustal heating from consequtive electron captures in even-A, even-Z nuclei.

Another source of heat is pycnonuclear, or density-driven, fusion in the inner crust [15]. Continued electron captures in the inner crust lower the Coulomb barrier for fusion reactions. This, combined with the decreasing distance between nuclei in the solid lattice of the crust, can trigger fusion reactions that release heat into the crust.

In addition to pycnonuclear fusion and electron capture heating which release on the order of a few MeV/u into the crust, observations of early cooling indicate that there is a yet-unidentified strong heat source near the surface of the neutron star [8]. Depending on the observed source, current models of early cooling require on the order of 1 MeV per accreted nucleon [16, 17], up to 10 MeV per accreted nucleon [9]. One hypothesis for the physical origin of this heat source is accretion-induced shear [18]. Infalling material carries angular momentum to the neutron star which is mostly deposited at shallow depths, leading to shear between differentially rotating layers and potentially viscous heating.

Most recently, it has been proposed that there is heating from the decay of charged pions produced by high-energy nuclear reactions on the surface of the neutron star during the accretion phase [19]. Strong gravitational acceleration of infalling material can lead to nuclear collisions with nuclei at the surface of the neutron star. If the kinetic energy of the incident particle is above the pion production threshold (~ 290 MeV), such that the centre-of-mass energy of the collision is higher than the pion rest mass, then it is possible for pions to be produced. The decay of π^+ produces a muon neutrino and an anti-muon, which itself decays to a positron, an electron neutrino, and an anti-muon neutrino. The muon neutrinos are thought to mostly leave the star, but the electron neutrinos are absorbed and heat the deep crust.

1.4 Urca cooling

In certain cases, electron capture-β decay cycles can form which cool the crust and core through neutrino emission, or Urca cooling. Urca cooling was first proposed by Mario Schenberg and George Gamow during a visit to the *Cassino da Urca* in Rio De Janerio as an explanation for the rapid cooling of neutron stars following their formation [20]. The direct Urca process that occurs in neutron stars can be described in Eqn. 1.1. The produced neutrinos and anti-neutrinos barely interact with the star, and stream freely out of the system, thus cooling it.

$$p + e^- \rightarrow n + \nu_e \tag{1.1a}$$

$$n \rightarrow p + e^- + \bar{\nu_e} \tag{1.1b}$$

The direct Urca process is possible when the protons, neutrons and electrons are highly degenerate, such as in the dense environment of the neutron star core, and their Fermi energies are such that momentum conservation is possible. In certain cases, depending on the mass of the neutron star and the equation of state, the direct Urca process is forbidden even in the core because the fermion number densities are not high enough, and the modified rather than direct Urca process occurs. In the modified Urca process, spectator particles (denoted A in Eqn. 1.2) are required to fulfil momentum conservation.

$$A + p + e^- \rightarrow A + n + \nu_e \tag{1.2a}$$

$$A + n \rightarrow A + p + e^- + \bar{\nu_e} \tag{1.2b}$$

Finally, the nuclear Urca process [21] has been understood to occur in white dwarves, but has recently been reported to occur in the crust of neutron stars [22].

$$^{Z}_{N}A + e^- \rightarrow ^{Z-1}_{N+1}A + \nu_e \tag{1.3a}$$

$$^{Z-1}_{N+1}A \rightarrow ^{Z}_{N}A + e^- + \bar{\nu_e} \tag{1.3b}$$

In the accreted crust of the neutron star, electron capture processes cause nuclei to become increasingly neutron-rich as they get pushed deeper into the crust. For a given isobar A in a zero-temperature crust, at a certain depth, it will exist as a single species $^{Z}_{N}A$. As it sinks, eventually the electron Fermi energy will equal and then exceed the Q-value for electron capture, and the species will transition to $^{Z-1}_{N+1}A$, which will have a distinct and sharp boundary separating it from the layer of $^{Z}_{N}A$ material.

However, at non-zero temperature, the electron Fermi surface is no longer mono-energetic

and there exists some phase space (within $\sim k_{\rm B}T$ of the Fermi energy) for electrons produced by β decay, thus allowing for β decays of ${}^{Z-1}_{N+1}A$ nuclei back to ${}^{Z}_{N}A$. For this to happen, the β decay has to go to the ground state (or a very low-lying state), and the neutrino has to carry away a small portion of energy so that the electron can be produced at or just below the Fermi energy, within this window. Instead of a sharp boundary separating the two layers, there now exists a thin layer of material where ${}^{Z}_{N}A$ and ${}^{Z-1}_{N+1}A$ co-exist (Fig. 1.3). This layer is known as an Urca shell, where repeated cycles of Urca processes can occur and emit a potentially large neutrino luminosity. The Urca cooling rate scales with T^5, therefore with sufficiently strong heating the Urca shell will effectively lead to a thermal decoupling of the layers above and below it, acting as a heat sink. This prevents heat produced by the outer layers to reach the interior of the star, and prevents any heat from deep crustal processes to reach the surface.

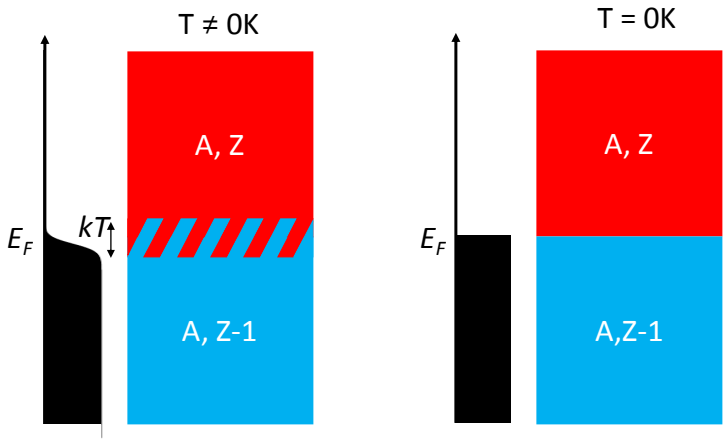

Figure 1.3: Left: Crust composition change boundary at non-zero temperature, showing the co-existance of A, Z nuclei and $A, Z-1$ nuclei in the Urca shell. Right: Crust composition change boundary at zero temperature, showing the sharp transition boundary with no Urca shell.

1.5 Impact of Urca cooling on neutron star observables

The impact of Urca cooling on superburst ignition has been assessed [23]. Because the Urca layer prevents heat produced by nuclear processes deeper in the crust from reaching the layer of C ignition in the neutron star ocean, it drives the layer of C ignition deeper into the ocean. The limitation on the amount of nuclear heating that increases the temperature of the ocean also places a lower limit on the strength of the shallow heat source. Ref. [24] has also shown that the observed light curve of source MAXI J0556-332 cannot be fit by current crust models if Urca cooling in present at the strengths expected from the composition of typical X-ray burst ashes. This was used to constrain the total accreted mass from the companion star during the accretion phase.

The magnitude of crust Urca cooling can be approximated as

$$L_\nu \approx L_{34} \times 10^{34} \text{ ergs s}^{-1} X T_9^5 \left(\frac{g_{14}}{2}\right)^{-1} R_{10}^2 \tag{1.4}$$

where T_9 is the temperature in GK, g_{14} is the surface gravity in 10^{14} cm^{-2}, R_{10} is the neutron star radius in units of 10 km, and L_{34} is a function only of nuclear properties:

$$L_{34} = 0.87 \left(\frac{10^6 \text{s}}{ft}\right)\left(\frac{56}{A}\right)\left(\frac{Q_{\text{EC}}}{4 \text{ MeV}}\right)^5 \left(\frac{\langle F \rangle^*}{0.5}\right), \tag{1.5}$$

and ft is the comparative half-life of the β-decaying transition, Q_{EC} is the electron capture

Q-value, $\langle F \rangle^*$ is

$$\langle F \rangle^* = \frac{F^+ F^-}{F^+ + F^-}, \tag{1.6}$$

$$\text{and } \langle F \rangle^{\pm} \approx \frac{2\pi\alpha Z}{|1 - e^{(\mp 2\pi\alpha Z)}|} \tag{1.7}$$

and α is the fine structure constant ($\approx 1/137$).

In terms of nuclear physics, Eqn. 1.5 shows that the two chief requirements for strong crust Urca cooling are: (1) a large abundance of the isobar in the ashes of the burst phase (i.e. a large X); (2) a low ft value, or strong ground state to low-lying state transition during the β decay. Urca cycles are hindered from forming in even-A nuclei due to the occunce of two consecutive electron captures. For the second electron capture, the Fermi energy of the electrons is higher than the β decay Q-value of the $A, Z-2$ nucleus, and β decay in this case is phase space blocked. Hence, though even-A nuclei are typically more abundant in X-ray burst ashes, Urca pairs tend to form most strongly in odd-A chains [23, 24]. [24] also demonstrated that Urca cooling has an observable impact on the light curves of quiescent neutron stars if the crust achieved a temperature of $\sim 10^9$ K for nuclei with ground state to ground state electron capture and β-decay transitions with log ft of around 5.

1.6 Motivation for the measurement

The goal of this thesis is to provide nuclear data that allow us to more reliably determine the strength of Urca cooling in accreting neutron star systems that exhibit X-ray bursts. Mass 61 nuclei are among the most abundant odd-A isobaric chains produced by the *rp*-process, largely due to the waiting point at ^{64}Ge, and can be present in X-ray burst ashes up to

β decay parent	Measured log ft	Reference	QRPA prediction
^{61}Ti	-	-	5.9
^{61}V	-	-	4.35
^{61}Cr	5.1	[26]	no transition predicted
^{61}Mn	4.7	[27]	4.84
^{61}Fe	7.1	[28]	4.69

Table 1.1: Measured log ft values for $A = 61$ nuclei and the QRPA predicted log ft for the ground state to ground state transitions.

several %. Measured log ft values for ground state to ground state β decay transitions among the neutron-rich mass 61 nuclei suggest that the $A = 61$ chain has the potential to significantly cool the neutron star crust. The experimentally-determined ground state to ground state log ft values to date and corresponding QRPA predictions [25] are given in Tab. 1.1. Data are not available for the decays of ^{61}V and ^{61}Ti, and QRPA calculations predict that the ground state to ground state decay of ^{61}V is the strongest transition in the chain with the lowest log ft value. However, there are large discrepancies of many orders of magnitude between measurements and QRPA predictions for ^{61}Fe and ^{61}Cr. Therefore, experimental data are mandatory to reliably estimate Urca cooling.

The ground-state spins of the neutron-rich mass 61 nuclei are given in Tab. 1.2 [29]. The spins for Ti-Cr were taken from shell model calculations using the TBLC8 interaction [30], but are supported by systematics [31]. The spin for Mn was calculated using the extended pairing-plus-quadrupole model with monopole corrections (EPQQM), which supports the log ft result from [27] for the transition from the ^{61}Mn ground state to the ground state of ^{61}Fe, indicating an allowed transition. The spin for Fe is from an experiment and supported by a shell model calculation, both from [32], using a truncated pfg model space [33].

The ground state spins indicate a possible allowed ground state to ground state β decay transition for ^{61}V and therefore a possible ^{61}Cr-^{61}V Urca pair. The next step is to exper-

Element	N	Z	J^π	Reference
Ti	39	22	$(1/2^-)$	[34]
V	38	23	$(3/2^-)$	[34]
Cr	37	24	$(5/2^-)$	[34]
Mn	36	25	$(5/2^-)$	[35]
Fe	35	26	$(3/2^-)$	[32]
Co	34	27	$7/2^-$	[29]

Table 1.2: List of spin/parity assignments for the neutron-rich $A = 61$ isobars. Assignments in parentheses are tentative.

imentally determine the log ft value for the β decay of ^{61}V to the ground state of ^{61}Cr. A previous β-decay study of ^{61}V [36] determined some branchings to excited states in the daughter nucleus ^{61}Cr, but did not derive a branching to the ground state due to incomplete information of the ^{61}Cr excitation scheme. The goal of this experiment is to experimentally determine the ground state to ground state transition strength of the decay of ^{61}V to assess the viability of the $A = 61$ mass chain as a strong Urca cooling chain.

1.7 Outline of dissertation

Chapter 2 discusses the experimental technique for measuring β decays and β-delayed radiation and the experimental set-up (detectors and electronics). Chapter 3 discusses the analysis of the data, including detector calibrations and efficiency measurements, and the data analysis techniques used for the extraction of the ground state branch of the β decay of ^{61}V. Chapter 4 details the results from the experiment, including the β decay half-life, β-delayed neutron emission branch, and the deduced ground state to ground state transition and ft value. Finally, chapter 5 discusses the astrophysical impact of the experimental result, as well as other potential Urca cooling candidates.

Chapter 2

Experimental Method

This experiment studies the β-decay of ^{61}V with the goal of determining the ground-state to ground-state transition strength of the decay of ^{61}V to ^{61}Cr. The ground state to ground state transition is difficult to measure directly because it does not emit any characteristic radiation in the form of γ rays or neutrons that can be used to constrain the number of such decays. Furthermore, β-decay electrons are not monoenergetic and thus cannot be used to discriminate the ground state to ground state transition from other transitions. In contrast, β-decay feeding to excited states can be identified by the sum energy of the γ rays emitted in the de-excitation cascade from the excited state to the ground state. The ground state to ground state feeding intensity can then be determined by subtracting the sum of all feeding to excited states and the total β-delayed neutron emission branch from the known total number of decays.

2.1 Overview of the technique

β decay involves the conversion of a proton to a neutron (β^+), if the nucleus is overly proton-rich, or a neutron to a proton (β^-), if the nucleus is overly neutron-rich. β decay has been extensively used in a large variety of nuclear physics experiments. For instance, it has been used to study the properties of resonances important for astrophysical reaction rates (e.g. [37]). β decay end-point studies utilise the fact that the electron energy spectrum

ranges from 0 keV to the energy difference between the mass of the parent nucleus and sum of the masses of the electron, electron neutrino, and daughter nucleus to make mass measurements of nuclei (e.g. [38, 39]). Analysis of the decay radiation also allows for the reconstruction of the ordering of excitation energies, or level scheme, of the daughter nucleus, and provides information about the nuclear properties of the daughter nucleus since the transition strengths depend on the nuclear matrix elements.

There are three different modes of β decay: (1) β^-; (2) β^+; and (3) electron capture (EC) and the underlying processes can be expressed as

$$\begin{aligned} \beta^- &: n \rightarrow p + e^- + \bar{\nu_e}, \\ \beta^+ &: p \rightarrow n + e^+ + \nu_e, \\ \text{and} \quad EC &: p + e^- \rightarrow n + \nu_e, \end{aligned}$$

where p is the proton, n is the neutron, e^- is the electron, e^+ is the position, ν_e is the electron neutrino and $\bar{\nu_e}$ is the electron anti-neutrino.

β decays follow quantum mechanical selection rules (table 2.1). The increasing suppression of of the decays as the difference in angular momentum of the initial and final states, $|J_f - J_i|$, increases is because large changes in angular momentum carried away by the electron require the electron to be localised far from the nucleus since the electron's momentum is relatively small. This scenario is unlikely due to the concentration of the electron wavefunction close to the nucleus.

There are two types of β decay, the Fermi transition, where the spins of the neutrino/anti-neutrino and the positron/electron are anti-parallel ($\Delta I = 0$), and the Gamow-Teller transition, where the spins of the neutrino/anti-neutrino and the positron/electron are parallel

Class	ΔJ	$\Delta\pi$
Allowed	0,1	no
First Forbidden	0,1,2	yes
Second Forbidden	2,3	no
Third Forbidden	3,4	yes

Table 2.1: Angular momentum and parity selection rules for β decay

($\Delta I = 0$ or 1). Most transitions are a mixture of Fermi and Gamow-Teller transitions; however, Fermi transitions only signifiantly contribute to transitions between isobaric analogue states, and β-decay transitions strengths are in general referred to Gamow-Teller strengths. This experiment is concerned with β^- decay:

$$ {}^{Z}_{N}A \rightarrow {}^{Z+1}_{N-1}A' + e^- + \bar{\nu_e}, \tag{2.1} $$

where ${}^{Z}_{N}A$ is referred to as the parent and ${}^{Z+1}_{N-1}A'$ is referred to as the daughter. The decay releases energy equivalent to the difference between the masses of the daughter nucleus, electron, and electron neutrino and the mass of the parent, known as the Q-value. Ignoring the mass of the neutrino and the binding energy of the electron to the daughter nucleus,

$$ Q(\beta^-) = \left[m({}^{Z}_{N}A) - m({}^{Z+1}_{N-1}A') \right] c^2, \tag{2.2} $$

where the masses used are the neutral atomic masses (hence why the electron mass does not appear). The daughter nucleus, electron, and the anti-neutrino share the energy released in the β decay. When the β decay populates the ground state in the daughter nucleus, the energy released is referred to as the reaction Q-value. In the case where the parent nucleus decays to an excited state of the daughter nucleus, the total energy of the electron and

anti-neutrino is simply the difference between the Q-value and the excitation energy

$$K_e + K_{\bar{\nu}} = Q - E_x. \tag{2.3}$$

Because this is a three-body process, the energy spectrum of the electron is not single-valued but rather follows the following distribution (for the simplest case of allowed transitions) [40],

$$N(K_e) = \frac{|M_f|^2}{2\pi^3\hbar^7 c^5} g^2 (K_e^2 + 2K_e m_e c^2)^{1/2} (Q - K_e)^2 (K_e + m_e c^2) F(Z', p_e), \tag{2.4}$$

where $F(Z', p_e)$ is the Fermi function, which takes into account the attraction (repulsion) of the produced electron (position) to the daughter nucleus with charge Z', $|M_{fi}|^2$ is the nuclear matrix element, related to the transition strength, and g is a constant representing the strength of the weak interaction.

In general, β decay will populate a number of states in the daughter nucleus and the strengths of these transitions, or the feedings, depend on the nuclear properties of the parent and daughter, and follow the angular momentum and parity selection rules (Tab. 2.1).

The β-decay strength for a particular transition is often represented in terms of the comparitive half-life or ft value. In terms of the transition half-life t,

$$ft = \ln 2 \frac{2\pi^3\hbar^7}{g^2 |M_{fi}|^2 m_e^5 c^4}. \tag{2.5}$$

The ft value of a specific transition is then

$$ft = f(Z', Q) \times \frac{t_{1/2}}{I_\beta}, \tag{2.6}$$

where $t_{1/2}$ is the parent half-life, $f(Z', Q)$ is the Fermi integral, and I_β is the β branching, or the fraction of total β decays that undergo the specific transition.

The log ft value is a measure of the intrinsic physical properties of the decay and can be determined experimentally from the β-decay branching, I_β, and the Q-value of the transition. Systematic comparisons across many nuclei show that the ft value is an indication of the "forbidden"-ness of the transition [41]. The ft value is often tranformed into $\log(ft)$ because of the large range of ft values.

2.2 Bateman equations

The rate of β-decay of a parent nucleus ${}^{Z}_{N}\mathrm{A}$ to its daughter is described by first-order kinematics, where the decay rate is proportional to the number of parent nuclei, N, at a given time t:

$$\frac{dN(t)}{dt} = -\lambda N(t), \tag{2.7}$$

where λ is defined as the decay constant. Integration of the decay equation gives

$$N(t) = N_0 e^{-\lambda t} \tag{2.8}$$

where N_0 is the initial number of parent nuclei at $t = 0$. The half-life of the nucleus is defined as the time it takes for half of the nuclei to decay and is related to the decay constant λ:

$$t_{1/2} = \frac{\ln 2}{\lambda}. \tag{2.9}$$

For N' daughter nuclei that are being produced by β decays of parent nuclei and are themselves β decaying, the net rate of change is given by the sum of the rate of production by β decay of the parent and the rate of destruction by its own β decay. The rate equation for such a species can be expressed as

$$\frac{dN'}{dt} = \lambda N - \lambda' N'. \tag{2.10}$$

The amount of nuclei of the parent and daughter, and any subsequent decays from the daughter nuclei, are described in general by the Bateman equations [42]:

$$N(t) = N_0 e^{-\lambda t} \tag{2.11}$$

$$N'(t) = N'_0 e^{-\lambda' t} - N_0 \frac{\lambda}{\lambda' - \lambda}\left[e^{-\lambda' t} - e^{-\lambda t}\right], \tag{2.12}$$

The general solution to the k^{th} decaying product is [43]:

$$N_k(t) = \sum_{j=1}^{k} A_j e^{-\lambda_j t} \prod_{l=j}^{l=k-2} \frac{-\lambda_{l+1}}{\lambda_{l+1} - \lambda_j}, \tag{2.13}$$

where A_j are constants related to the initial quantity of the j^{th} species and λ_j are the decay constants of the j^{th} species.

2.3 β-delayed γ decay

β decay of a parent nucleus can populate, in addition to the ground state, excited states in the daughter nucleus. For low-energy states below any particle emission thresholds, the dominant decay mechanism is γ-ray emission to a lower-lying state. Theoretically, the β-

feeding intensities to each excited state in the daughter can be calculated by determining the (efficiency-corrected) number of γ rays emitted from a given state, and the number of γ rays that feed the state. The transition strength to the daughter ground state is then simply 100% less the sum of the transition strengths to the excited states. Practically, this method requires a full understanding of the level scheme of the daughter nucleus so that observed γ rays can be correctly assigned to corresponding transitions between states in the daughter nucleus. To do so, the γ-ray detector used has to have a high-enough resolution to be able to isolate individual γ-ray energies. The use of high-resolution Ge detectors in β decay experiments trades the ability to distinguish individual transitions for efficiency. For nuclei where the level density is low, or where the low Q-value limits the number of possible states which can be populated by β decay, such a trade-off is acceptable. For nuclei which have large β-decay Q-values where the number of possible γ transitions is large, or nuclei where level densities are high, the method fails due to the difficulty in deriving a complete level scheme. For low-efficiency, high-precision detectors, it is likely that only the strongest transitions are detected, and that the weak transitions which can still constitute a non-negligible fraction of the β-decay scheme will be missed. This is especially true in γ decays involving high multiplicity cascades, where the likelihood of detecting the entire cascade diminishes with each additional γ ray, or high-energy γ rays, where the efficiency of detecting each γ-ray is relatively low. The β-feeding intensity to a given state i is determined as the difference between the number of γ rays depopulating i and the number of γ rays that populate i from higher-lying states. A large number of weak β-decay transitions to higher-lying states, which are hard or impossible to detect, can still lead to significant population of i by γ decay. Missing these weak transitions thus leads to a systematic overestimation of the β-feeding intensity to i.

This effect is known as the Pandemonium effect [44], and has been a long-standing problem in β decay studies. The effect was first studied using a Monte Carlo simulation of the β decay creating a fictional nucleus "Pandemonium" in [44], and it was demonstrated that with the exception of light nuclei with low Q-values, it is likely that the Pandemonium effect will manifest itself in high resolution γ ray spectroscopy studies, leading to unreliable determinations of β strengths.

We employ a method called Total Absorption Spectroscopy (TAS) or Total Absorption Gamma Spectroscopy (TAGS) to address this effect, using a large, high-efficiency Summing NaI (SuN) detector to provide 4π coverage of the source of radiation. Though TAS detectors often have low energy resolution, their extremely high efficiency enables the measurement of even the weakest branches in the β decay. This method focuses on measuring the total energy of γ ray cascades rather than indiviual γ transitions. In this case, instead of separately identifying populating and depopulating transitions for a given state, the β-feeding intensity is obtained directly from the number of cascades depopulating a state.

2.4 β-delayed neutron emission

When the decay Q-value is larger than the neutron separation energy S_n, it is possible for the decay to populate states above the neutron separation threshold that subsequently emit neutrons. This is known as β-delayed neutron emission. Because this is a two-body process, the neutron will be emitted with energy

$$E_n = E_{x,i} - E_{x,f} - S_n, \tag{2.14}$$

where $E_{x,i}$ and $E_{x,f}$ are the excitation energies in the emitter and the produced nucleus (hereafter referred to as the neutron daughter) respectively, and S_n is the neutron separation energy. The sum of all neutron-emission probabilities is referred to as the total β-delayed neutron emission branch or P_{n} value. Since the decay to the ground state of the neutron daughter also does not emit any characteristic γ radiation and therefore is otherwise indistinguishable from the decay to the ground state of the daughter, it is imperative to know the P_{n} value to correctly determine the ground state to ground state transition to the daughter.

2.5 Experimental Description

The experiment, NSCL experiment E14041, took place at the National Superconducting Cyclotron Laboratory (NSCL) between the 8^{th} and 15^{th} of August 2015. The purpose of the experiment was to determine the ground state to ground state transition strength in the β decay of ^{61}V to ^{61}Cr; it involves the use of high-efficiency detector systems to determine the total decay strength to the excited states. The set-up to measure the radiation from the beta-decay of ^{61}V consisted of (i) a set of Si PIN detectors, which provided particle identification from energy loss and flight time between the PIN detectors and the Image 2 scintillator of the A1900; (ii) a Si Double-Sided Silicon Strip Detector (DSSD) for implant and decay energy loss and location of the implants and decays; (iii) a NaI(Tl) Total Absorption Spectrometer (TAS) for the measurement of β-delayed γ ray emission and; (iv) a neutron long counter system for the measurement of β-delayed neutron emission.

2.5.1 Beam delivery from CCF and A1900

The primary beam was a 35 pnA ^{82}Se beam at 140 MeV/u , impinging on a Be target, producing a cocktail beam that was purified by the A1900 fragment separator. ^{82}Se was selected based on LISE++ [45] calculations because it produced a combination of the highest rate and purity of ^{61}V in the cocktail secondary beam.

The A1900 fragment separator [46, 47] consists of a series of four magnetic dipoles that discriminate between beam components by their momentum-to-charge ratio and also has an additional 24 magnetic quadrupoles for beam focusing. The Image 2 (I2) position is located between the second and third dipoles; at this position, there was a plastic scintillator with a thickness of 254 μm as well as an Aluminium wedge with 0° thickness of 450 mg/cm^2. The plastic scintillator provided time-of-flight information, acting as the 'stop' signal; to do this, the signals from the scintillator were time-delayed such that they reached the Time-to-Amplitude Converter (TAC) after the 'start' signal from the experimental end station. This was done because the separation of unwanted beam by ion optic components downstream of the I2 scintillator meant that only a small fraction (0.1-0.01%) of beam particles incident on the scintillator were transmitted to the experimental end station. In the case of this experiment, the rate at the I2 scintillator was ∼10,000 pps, whereas the rate at the first detector at the experimental set-up was more than two orders of magnitude lower. The plastic scintillator was read out by two different photomultiplier tubes (PMTs) located on opposite sides of the scintillator, referred to I2N and I2S. The time difference between the firing of these two PMTs gave the position along the dispersive plane for momentum corrections.

Particles travelling through a magenetic dipole with a constant magnetic field obey the

equation of motion,

$$B\rho = \frac{mv}{q}, \tag{2.15}$$

where B is the magnetic field strength, ρ is the radius of curvature, mv and q are the momentum and charge of the particle respectively, and $B\rho$ is collectively defined as the magnetic rigidity. For light nuclei, in this case ^{61}V, it is possible for the nucleus to be fully stripped of its electrons such that q is equal to the nuclear charge Z of the nucleus. Fragments produced by the primary beam impinging on the Be target that are transported to the A1900 have a limited velocity range. The A1900 fragment separator transports only particles with a fixed $B\rho$ (within some percentage acceptance of up to $\pm 2.5\%$), thus allowing for m/Z selection. At the I2 position, the fragments passed through an Aluminium wedge, and lost energy depending on the fragment nuclear charge. At the beam energies of $\sim$100 MeV/u, the energy loss of heavy ions in matter depends on the thickness of the material, the energy of the ion, and the charge of the ion in the following manner:

$$\frac{dE}{dx} \sim \frac{Z^2}{E}. \tag{2.16}$$

At 100 MeV/u, the energy loss through a thin foil is insignificant relative to the total energy, thus the right side of the above equation can be considered to be constant, and the total energy loss through the material can be well approximated by

$$\Delta E \sim \frac{tZ^2}{E}, \tag{2.17}$$

where t is the thickness of the material. Because this energy loss is Z dependent, the change in $B\rho$ is also Z dependent and leads to a broader $B\rho$ distribution following interaction with

the wedge. This allowed for further purification of the beam, as the second set of A1900 dipoles also have a fixed $B\rho$ acceptance. The shape of the wedge in this case was chosen to ensure achromatic focus to maximise transport of the secondary beam to the end of the A1900. For the experiment, the A1900 delivered a secondary beam of ∼36% ^{61}V, with only three major beam contaminants ^{62}Cr, ^{64}Mn and ^{65}Fe.

2.5.2 Particle identification

To distinguish between the beam components, particle identification was done on a event-by-event basis with the δE-TOF method, using the energy loss through the Si PIN detector at the experimental station to discriminate by nuclear charge, and the time-of-flight from the I2 plastic scintillator at the focal plane of the A1900 to the Si pin detector to discriminate by velocity. The particle identification was also further improved through a momentum correction ascertained from the position along the dispersive axis where the beam particle hits the I2 scintillator, allowing for better separation between isotopes of the same element.

2.5.3 Detectors

The experiment utilized many different types of detectors, and their characteristics and purpose will be explained.

2.5.3.1 NERO

The Neutron Emission Ratio Observer (NERO) [48] is a neutron long counter system consisting of 44 BF_3-filled tubes and 16 ^{3}He-filled tubes housed in a high-density polyethylene matrix (ρ=0.93(1) g/cm^3) 60×60×80 cm^3 in size. The matrix has a cylindrical bore of radius 11.4 cm, which was designed to hold the NSCL Beta Counting System [49]. The neutron

counters are co-axial to the beam axis and centred on the detector located in the target position in the BCS chamber. The 60 detectors are arranged in 3 concentric rings, with the innermost ring comprising of the 16 ^{3}He detectors, and the outer two rings comprising of the remaining BF_3 counters.

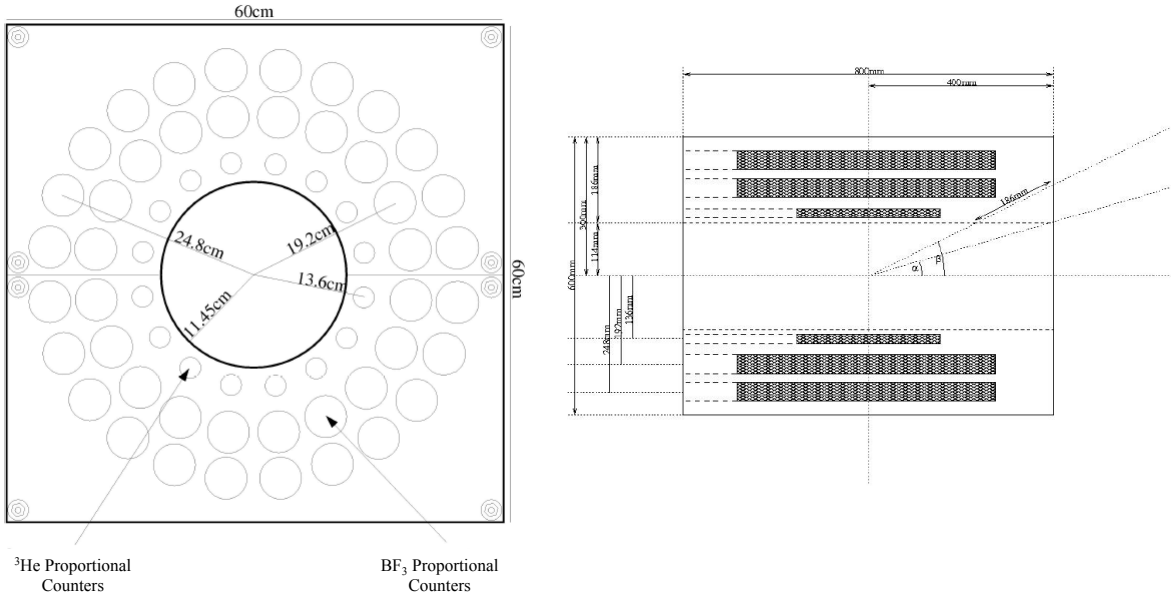

Figure 2.1: Left: Layout of the NERO tubes. Right: Cross-section schematic of NERO. Adapted from [50].

Long counter systems operate on the principle of neutron-induced reactions by neutrons thermalised by a moderating material. The cross-section for neutron-induced reactions at low energies depends inversely on the velocity of the neutron

$$\sigma \propto \frac{1}{\sqrt{E}} \propto \frac{1}{v} \tag{2.18}$$

due to the lack of a Coulomb interaction and the dominance of s-wave capture. For maximising efficiency, it is thus advantageous for the neutron to have as low energy as possible.

Neutrons emitted from the centre of NERO are moderated by interactions with the polyethylene. The energy loss of a neutron collision with a nucleus of mass A is given by

$$\frac{E_f}{E_i} = \frac{A^2 + 2A\cos\theta + 1}{(A+1)^2} \tag{2.19}$$

where E_f and E_i are the final and initial energies of the neutron respectively, and θ is the scattering angle. In the limit where A is large, the quadratic terms dominate and

$$\frac{E_f}{E_i} \sim \frac{A^2}{(A+1)^2} \sim 1. \tag{2.20}$$

Therefore it is ideal to choose a moderating material with as low mass as possible such that fewer scattering events are needed to thermalise the neutron; Polyethylene is an ideal moderator due to the high density of protons. As the neutrons are moderated, they ultimately induce the reactions $^{10}\mathrm{B}(n,\alpha)^{7}\mathrm{Li}$ and $^{3}\mathrm{He}(n,p)^{3}\mathrm{H}$ in the BF_3 and ^{3}He tubes respectively. The produced charged particles then ionise the gas in the tube and the voltage difference applied through the tube triggers and extracts electron cascades (hence the term 'proportional' counters), indicating a neutron detection. Long counters have the advantage of high efficiency for low-energy neutrons, but the disadvantage of losing all initial momentum information of the neutron. The NERO detector was designed to optimize the efficiency for the detection of neutrons lower than 2 MeV. The detector was commissioned in 2005 and calibrated using a series of resonant and non-resonant reactions, as well as a ^{252}Cf source [48]. Monte Carlo N Particle (MCNP) [51] simulations of the efficiency curve (as a function of neutron energy) well-reproduced the trend of the experimentally-determined efficiency curve seen from data, but showed a systematic over-estimation of the efficiency. Thus, the MCNP-

simulated efficiency curve was scaled to the measured efficiency values to obtain the detector efficiency curve at low neutron energies.

2.5.3.2 SuN

The Summing NaI (SuN) detector [52] is a total absorption spectrometer that is primarily used as a γ ray detector. A summing detector was chosen for the experiment to resolve the issue of the Pandemonium effect. Because the β decay transition strengths are extracted from the size of the sum peak at a given energy, it is important for the summing efficiency to be as high as possible. SuN consists of 8 half-annular crystals of Tl-doped NaI, forming a barrel 1ft in length and diameter (Fig. 2.2). Total absorption spectrometers require several properties that the design of SuN takes into account. NaI was chosen because of the ease of producing large monocrystalline volumes, this is simply so that the interaction volume is large, increasing the efficiency. The crystal is doped with Tl, introducing states into the band gap between the conduction and valence bands of pure NaI. These intermediary states are desirable because the wavelengths of photons produced overlap well with the response of photomultiplier tubes.

SuN has several advantages over more precise Germanium detectors for this experiment as the number of transitions is predicted to be extremely high due to the large reaction Q-value and high level density [53], resulting in a significant Pandemonium effect. Firstly, since the level scheme of the daughter nucleus of the ^{61}V β decay, ^{61}Cr, is only known up to $\sim$2.26 MeV compared to the β-decay Q-value of $\sim$12 MeV, individually detected γ rays may not easily be associated with a particular nuclear transition. Secondly, there are likely to be a number of weak transitions to states in ^{61}Cr which themselves can decay through a multitude of different cascades, and Ge detectors simply do not have the intrinsic efficiency to

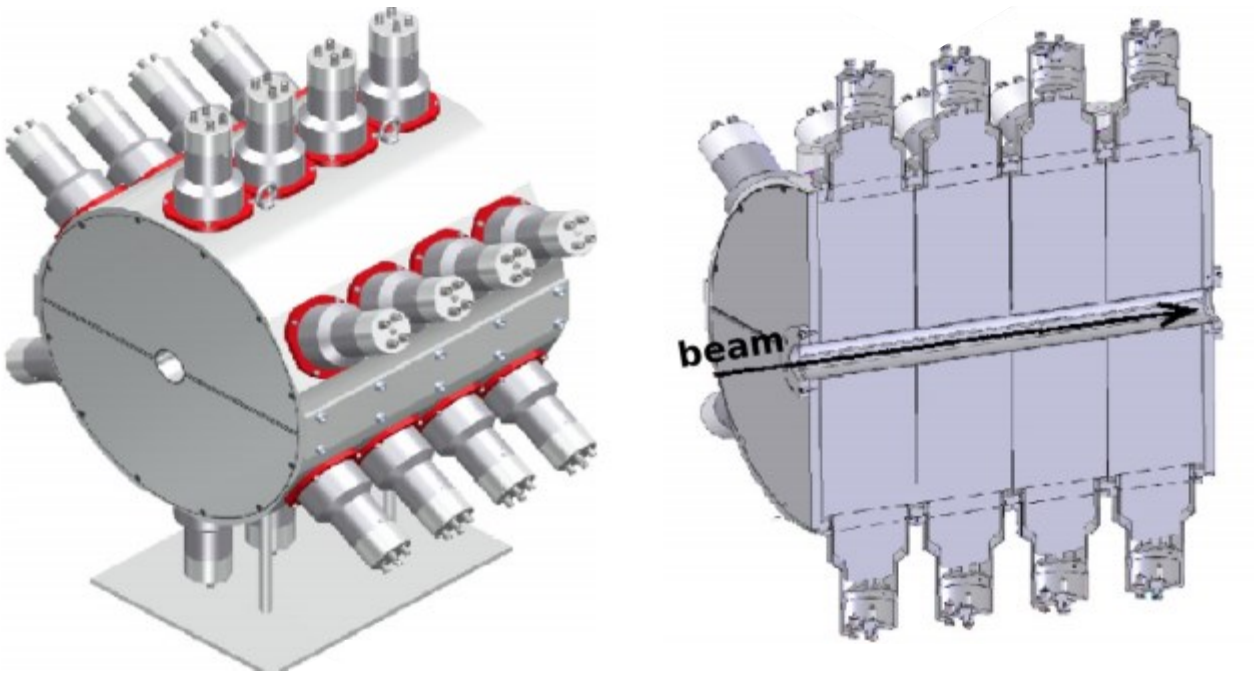

Figure 2.2: Left: Schematic of SuN. Right: Lengthwise cross-section of SuN. Adapted from [52]

measure every one of these transitions. SuN, with its high geometric and intrinsic efficiency, is better suited for this measurement because summing detectors are designed to measure the total energy of an entire γ-ray cascade (or sum peak), rather than individual transitions.

The total absoprtion technique is demonstrated using the decay of ^{60}Co to stable ^{60}Ni. This is an ideal case as the decay scheme is simple due to the low reaction Q-value of 2.8228 MeV and the low density of states at low energy in ^{60}Ni. There are only three excited states which can be populated by the β-decay; the first 2^+ excited state at 1332.5 keV, the second 2^+ excited state at 2158.6 keV, and the first 4^+ excited state at 2505.7 keV. Of these three states, the β-feeding intensity to the 4^+ state dominates (99.88%) since the ground state of ^{60}Co has $J^\pi = 5^+$. The remainder of the decays will populate the 1332.5 keV state, while there is virtually no population of the 2158.6 keV state. In this example, we will focus on the γ decays following a β decay to the 2505.7 keV state.

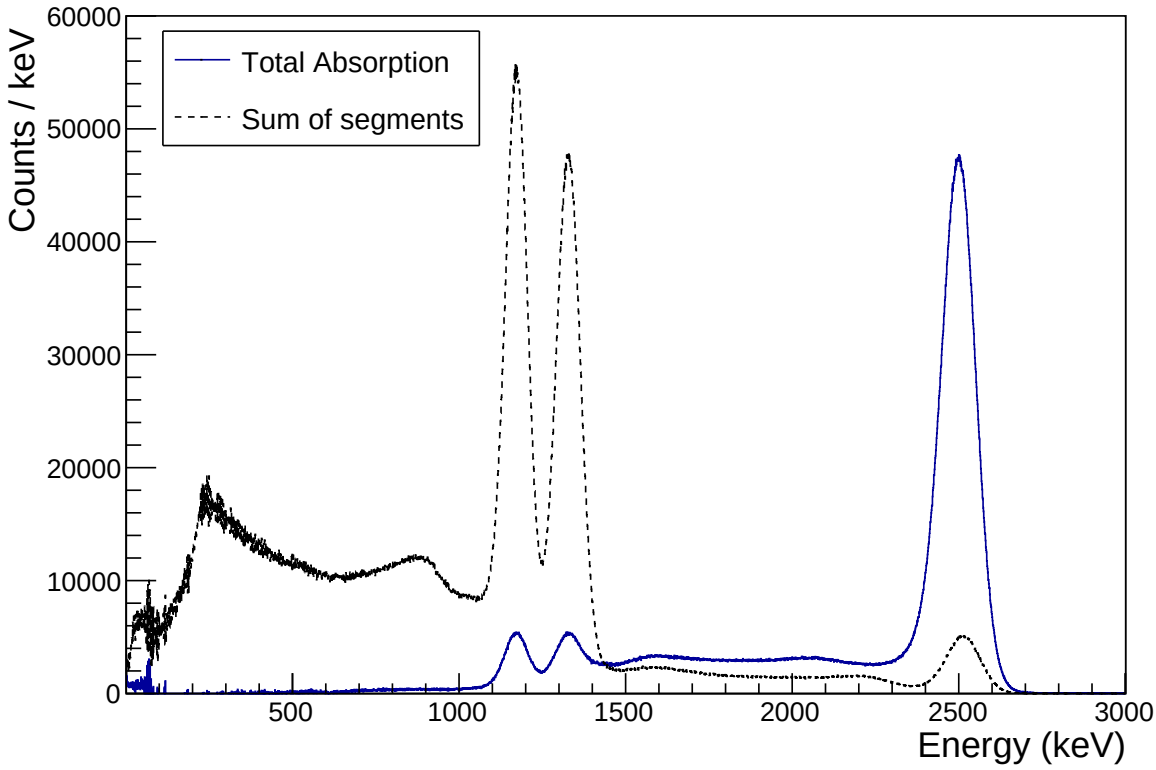

Figure 2.3: The total absorption (solid blue) and sum of segments (dashed black) spectra for a ^{60}Co source.

The 2505.7 keV state can decay directly to the ground state or to the first or second excited 2^+ states. The predominant branch is the cascade decay through the first excited state, with two γ rays of 1173.2 keV and 1332.5 keV. The cumulative spectrum of the individual scintillator segments in SuN, hereafter referred to as the sum of segments spectrum, is shown in Fig. 2.3.

The two individual peaks at 1332.5 keV and 1173.2 keV dominate the spectrum. The small peak at 2505.7 keV demonstrates the much weaker branching of the direct to ground state transition, or the case where both γ rays in the spectrum are detected in the same crystal. The total absorption spectrum is constructed by adding together the total energy detected in each segment for each γ ray event. In the total absorption spectrum for the

same ^{60}Co decay, the peak at 2505.7 keV dominates, with smaller peaks at 1332.5 keV and 1173.2 keV due to incomplete summing when one of the γ rays is missed.

2.5.3.3 Double-Sided Strip Detectors (DSSDs)

Nuclei in the secondary beam delivered to the experimental area were implanted in the DSSD and subsequently decay, emitting a β decay electron which can also be detected by the DSSD. The DSSD used for the NERO portion of the experiment (hereafter referred to as the BCS DSSD) was a Micron Semiconductor BB1 (979 μm), with each side of the DSSD segmented into 40 strips with $\sim$1 mm pitch, for a total of 80 strips and an active area of 39.90 $\times$ 39.90 mm^2. The front and back sides of the DSSD are segmented orthogonally, creating 1600 1 mm^2 pixels. Each channel is read out by a Multi-Channel Systems CPA-16 dual-gain pre-amplifier, for a total of 160 channels, allowing the detection of both the implanted ion (low gain, GeV range) and the β-decay electron (high gain, MeV range). The DSSD used for the SuN portion of the experiment (hereafter referred to as the miniDSSD) was a Micron Semiconductor BB8 type (1030 μm), with each side of the DSSD segmented into 16 strips with 1.25 mm pitch, forming a total of 32 strips and an active area of 20.0 $\times$ 20.0 mm^2; each strip is read out by a Multi-Channel Systems CPA-16 dual-gain preamplifier. Similar to BCS DSSD, the front and back strips are segmented orthogonally, forming a total of 256 pixels.

2.6 Data Acquisition

2.6.1 Digital Data Acquisition System

The signals from the detector systems in the experiment were processed with the NSCL Digital Data Acquisition System (DDAS) [54, 55]. NSCL DDAS utilises the XIA digital gamma finder class of electronics, currently all of the Pixie-16 (16 channel) type. Each channel is FPGA-programmable, and can independently read out a pulse arrival time and pulse-processed energy. In total, 24 100 Mega-sample per second (MSPS) Pixie-16 modules were used in a three-crate system. Each module also has the ability to transmit and receive another module's clock signal, allowing for a system-wide timing synchronisation to within one clocktick (10 ns). Each DDAS event is stored as four 32-bit words. An annotated example event is given in Fig. 2.4. The first 32 bits store the crate and channel information and the event length. The next 32 bits store the least significant bits of the timestamp in units of clock ticks. The third 32 bits has two 16 bit segments, with the first recording the most significant bits of the timestamp in units of clockticks, for a total of a 48-bit timestamp ($\sim$782 hours), and the second recording the constant fraction discriminator (CFD) time for sub-timestamp clock precision. The final 32 bits also has two 16 bit segments, with the first storing the pulse-processed energy and the second storing the trace length (if recorded).

DDAS has an advantage over analog electronics systems in terms of throughput. The vast majority of analog acquisition systems, when triggered, will store the peak point of the signal in a capacitor, which is then converted to a digital value for the data acquisition system. When this conversion process occurs, the analog system will be in the interrupt state and cannot accept more signals, a period of time known as the 'dead time' of a system. Digital electronics do not require such a conversion, and its dead time is mostly determined

```
Event 56 bytes long
0038 0000 9bb0 01fc 0000 0000 0002 0000
0020 0000 0000 0000 0020 0000 001e 0000
000c 0000 00fa 0f0e 42ac 0008 9376 003f
0000 0000 0017 0000
```

```
0038 0000                 event length = 56 bytes
          9bb0 01fc       timestamp = 33332144 ns
0000 0000
          0002 0000       data source = source 2
0020 0000                 fragment length = 32 words
          0000 0000
0020 0000                 fragment length = 32
          001e 0000       data type = 30 (physics event)
000c 0000 00fa 0f0e       DDAS firmware identifier
42ac 0008                 4 word evt, crate 2, mod 10, ch 12
          9376 003f       lowest bits of timestamp
0000 0000                 total timestamp = 4166518 clockticks
          0017 0000       energy = 23 ADC u.; trace length = 0
```

Figure 2.4: Example of an event in the DDAS data stream. The top panel shows the event as it is recorded in the data stream. The bottom panel shows the same event with each separate component commented out.

by the length of the filter used to calculate if a trigger is accepted or not. This is useful for a detector such as SuN, which in self-trigger mode will have thousands of counts per second just from room background. Another advantage of DDAS is the ease with which it can be set up, especially if the filter parameters are already known from previous calibrations or experiments (assuming the pre-amplifiers are the same).

The input traces are analysed using a short filter, called the trigger or fast filter, that determines if a rising edge of a signal is detected. DDAS uses a type of filter called a trapezoial filter. A trapezoidal filter is characterised by two windows with length L separated by a flat top time G. The application of the filter subtracts the signal heights in the first section of length L from the signal heights in the second section of length L. The advantage of a trapezoidal filter over a triangular filter (where $G = 0$) is that it avoids summation over the region where the signal height is changing rapidly. Consider a pulse with some height H- the determination of H by DDAS uses a simple subtraction of the points before the pulse trigger and after the pulse trigger to determine H. For a trapezoidal filter with rise time L and gap time G, the signal height H is found by the following equation:

$$LH_k = \sum_{k-L+1}^{k} H_i - \sum_{i=2L-G+1}^{k-L-G} H_i \tag{2.21}$$

where k is a signal point. This procedure is repeated for every new signal point k until the filter threshold is passed. If the trigger threshold set in DDAS is passed by the output of the trigger filter, it is timestamped and the trace passes through a longer trapezoidal filter, called the energy or slow filter. The output of the energy filter at time PEAKSAMP (determined only by parameters of the energy filter) after the trigger point is then stored as the energy value of the event. An example of filter output of a signal is given in Fig. 2.5.

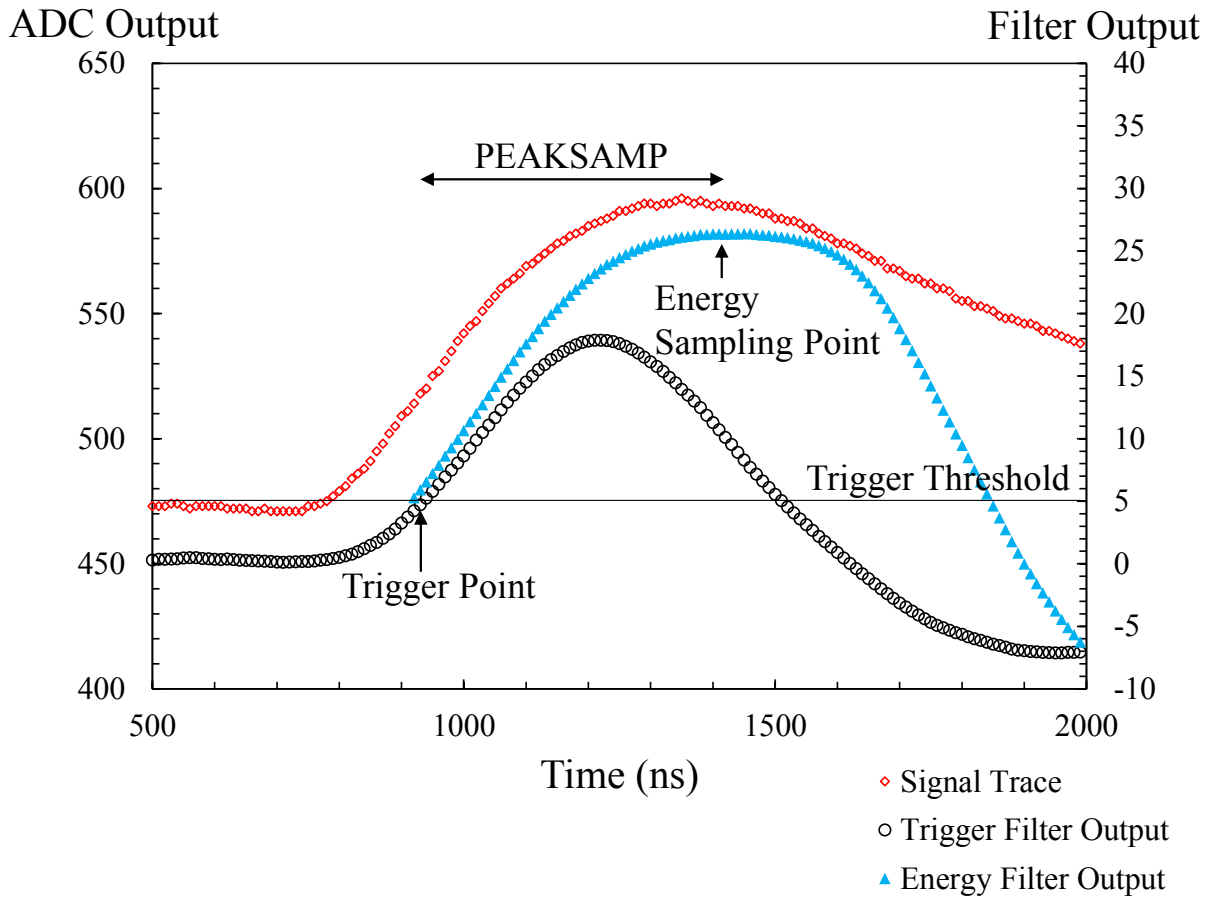

Figure 2.5: Example of a trace (red diamonds), the trigger filter output (black circles), and the energy filter output (blue triangles) from a representative DSSD high gain signal. The energy filter output has been scaled down to fit on the same scale as the trigger filter output. The trigger filter parameters are $L = 80$ ns and $G = 500$ ns. The energy filter parameters are $L = 100$ ns and $G = 700$ ns.

When determining which filter parameters are best for a signal, the following guidelines were useful: (a) The 'flat top' time of the trapezoidal filter should be approximately the rise time of the signal; (b) the rise time of the trigger filter is primarily determined by the signal-to-noise ratio, and the longer the trigger filter rise time, the more baseline of the signal is averaged over such that a lower trigger threshold can be set without triggering on noise. The trade-off by choosing a long filter rise time is that the effective dead-time of the system increases with the length of the trigger filter; (c) the rise time of the energy filter will determine the energy resolution of the slow filter.

Finally, another important DDAS parameter is τ, the decay time of the signal. Due to the high trigger rates in the experiment, signal pile-up occurs where the signal does not return to the baseline before the second pulse arrives. Therefore, it is necessary to know the extent to which the first signal has decayed or decreased for an accurate baseline subtraction. As a result, the position of the energy peak in ADC units is fairly sensitive to τ. In contrast, the resolution is less sentitive to τ. For the experiment, the filter parameters were optimised for each channel individually and τ was obtained by fitting signal traces.

2.6.2 NSCLDAQ

The data acquisition used during the experiment was the NSCL Data Acquisition suite of softwares (NSCLDAQ) which is well-suited for processing and merging data flows from different sources. This capability was especially relevant for the experiment as there were three separate DDAS crates read out by three separate computers. NSCLDAQ provides flexibility by allowing each individual crate to run its acquisition (termed 'readout') independently (useful for troubleshooting), or to be controlled by a master system that enforces time-ordering of events from different sources. In a multi-crate system, each crate has its

own onboard computer (spdaq) device which is read out independently of each other. The on-board buffer acquires data and is polled continuously by readout, and upon hitting a user-defined threshold, the data are transferred to a ringbuffer that is specific to each spdaq device or data source. Each data source is subsequently read out into a ring buffer or circular buffer, termed within the NSCLDAQ system as a 'raw ring'. The advantage of ring buffers for continuous data acquisition is that it easily preserves a first-in first-out (FIFO) queue without pointer reassignment, such that event triggers that occur first temporally are also read from the ring buffer first in the data stream. Each raw ring is then fed to the NSCLDAQ on-line event builder, a system designed to merge data from different sources in a time-ordered fashion. A data packet from a raw ring is wrapped in a header which provides information on the data source and the global timestamp (compared to system clockticks, which is what raw data usually stores) such that systems with different clock frequencies can be run. The second part of the NSCLDAQ event builder is the *glom* software, which collects all triggers occuring within a user-defined correlation time into an event.

2.6.3 Defining a physics event

The use of digital data acquisition allows for the timestamping of each accepted trigger. Instead of relying on external triggers, triggers are gathered into groups defined by a time period, similar to the *glom* software in the NSCLDAQ event builder. A group of triggers is hereafter referred to as a physics event, meaning that the triggers originate from the same physical event such as a beam particle being stopped or a β decay. In this manner, triggers from SuN or NERO that follow the detection of a DSSD signal are grouped together with the DSSD trigger. In the case of the NERO portion of the experiment, this coincidence window is defined to be 200 μs to accomodate the moderation time of neutrons in NERO (discussed

in section 3.1.1.1). In the case of the SuN portion of the experiment, the coincidence window was defined to be 300 ns to minimise the contribution of background γ rays.

2.7 Experimental End Station

The experiment was run in two segments, first with the beam focused on the DSSD centred in NERO (9.8 hours) and then on the miniDSSD centred in SuN (90 hours). The most upstream part of the end station consisted of a cross containing (from upstream to downstream) two Si PIN detectors and passive beam degraders. SuN was located downstream of the cross and NERO was downstream of SuN. Though the two detectors were not used simultaneously, this configuration was chosen to optimise the use of beam time. 8 hours were allocated following the NERO run to remove the NERO target chamber and insert the SuN target (different to the NERO target) in the centre of SuN. To achieve such a rapid switchover time, both SuN and NERO were set up initially and an empty beampipe connected the upstream cross to the NERO target chamber. Once the NERO measurement was completed, the SuN miniDSSD was inserted into the beam pipe in the centre of SuN and the SuN measurement was subsequently conducted. Because the two segments only share the two PIN detectors in common and essentially function as two independent end stations, the set-up for the NERO and SuN runs will be described separately.

2.7.1 NERO set-up

A schematic of the NERO set-up is shown in Fig. 2.6, and a table of the detectors used along with their characteristics is given in Tab. 2.2.

The passive degraders were placed downstream of PIN2 in the PIN stack so that the

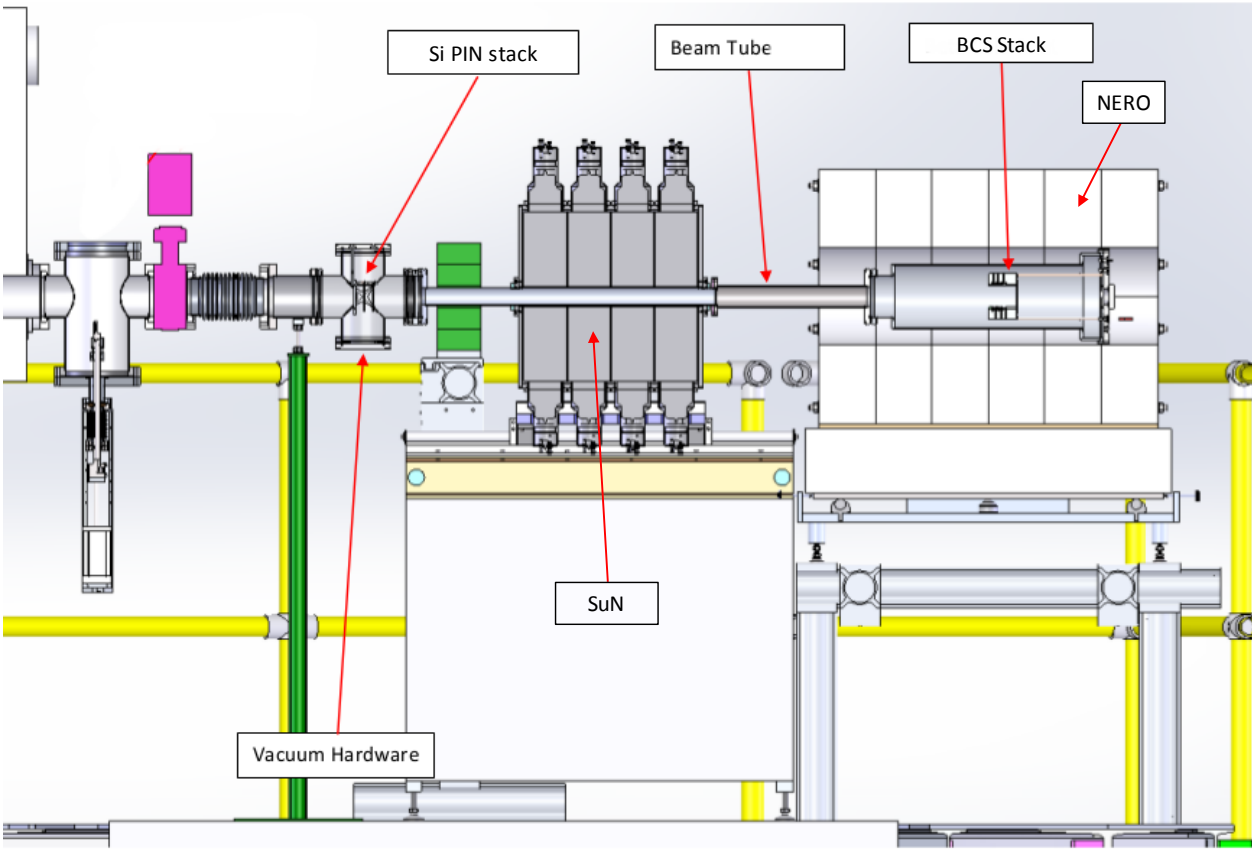

Figure 2.6: A cartoon showing the components of the set-up for the NERO portion of the experiment.

PINs would not have to be moved when the passive degraders were changed for the SuN run. PIN3 and PIN4 were read out by low-gain pre-amplifiers for additional particle identification information (eventually not used for this function) and for determining transmission of the secondary beam through to the DSSD. PIN5 was read out by a high-gain pre-amplifier as a secondary light particle veto, but this information was not used in the analysis. A Si Double-Sided Strip Detector (DSSD) was at the target position at the centre of NERO. A Si Single-Sided Strip Detector (SSSD) was located directly downstream to veto particles which

Si PIN Stack

Detector	Thickness (μm)	Voltage (V)	Gain
PIN1	525	40	Low
PIN2	1041	75	Low
Al Degrader	250	-	-

BCS Stack

Detector	Thickness (μm)	Voltage (V)	Gain
PIN3	488	50	Low
PIN4	503	-30	Low
PIN5	991	-150	High
DSSD	979	280	Low and High
SSSD	982	-210	High
Scintillator	$\sim$ 25400	-850	High

NERO

Detector	Type	Voltage (V)
NERO A 1-4	^{3}He	1130
NERO B 1-4	^{3}He	1130
NERO C 1-4	^{3}He	1080
NERO D 1-4	^{3}He	1350
NERO A 5-15	BF_3	2620
NERO B 5-15	BF_3	2620
NERO C 5-15	BF_3	2620
NERO D 5-15	BF_3	2620

Table 2.2: List of detectors and properties used in the NERO set-up.

did not lose all their energy in the DSSD (termed 'punchthroughs'), followed by a thick plastic scintillator which was used as the primary light particle veto. Light particles such as He ions that can be part of the fragment beam deposit approximately the same energy in the silicon detectors as β decay electrons and can mimic decay signals. The thick plastic scintillator enables the differentiation of β decay electrons from light particles, as the light particles will deposit far more energy in the scintillator than the maximal β decay electron energy of 11.95 MeV, which was chosen as the upper threshold above which all β-like signals in the DSSD are vetoed.

The data acquisition electronics are shown in Figs. 2.7 and 2.8. A coincidence between a signal from a front strip and a back strip of the DSSD was required for a valid signal to be read out. The DDAS signals were passed to DDAS breakout modules, which were used to extract a 16-channel OR over all the channels in a module. The TTL signals that contain the AND signals from the front and back strips were then passed back into the DDAS breakout modules as an external trigger for DDAS. For all other detectors, the signals were processed in self-trigger mode, and did not require any external validation. This was possible because the lack of dead time of DDAS enabled the recording of high trigger rates.

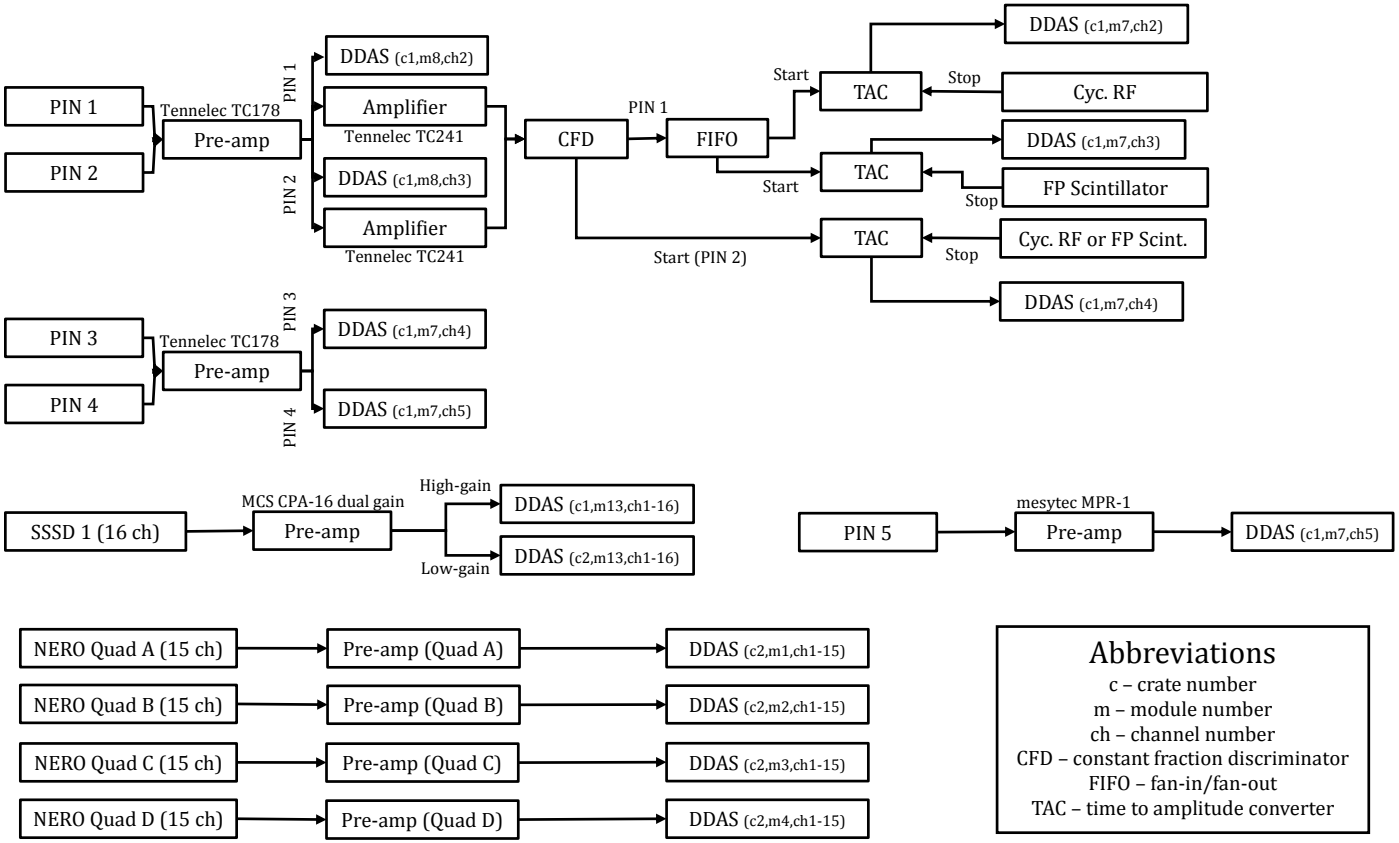

Figure 2.7: BCS/NERO electronics logic.

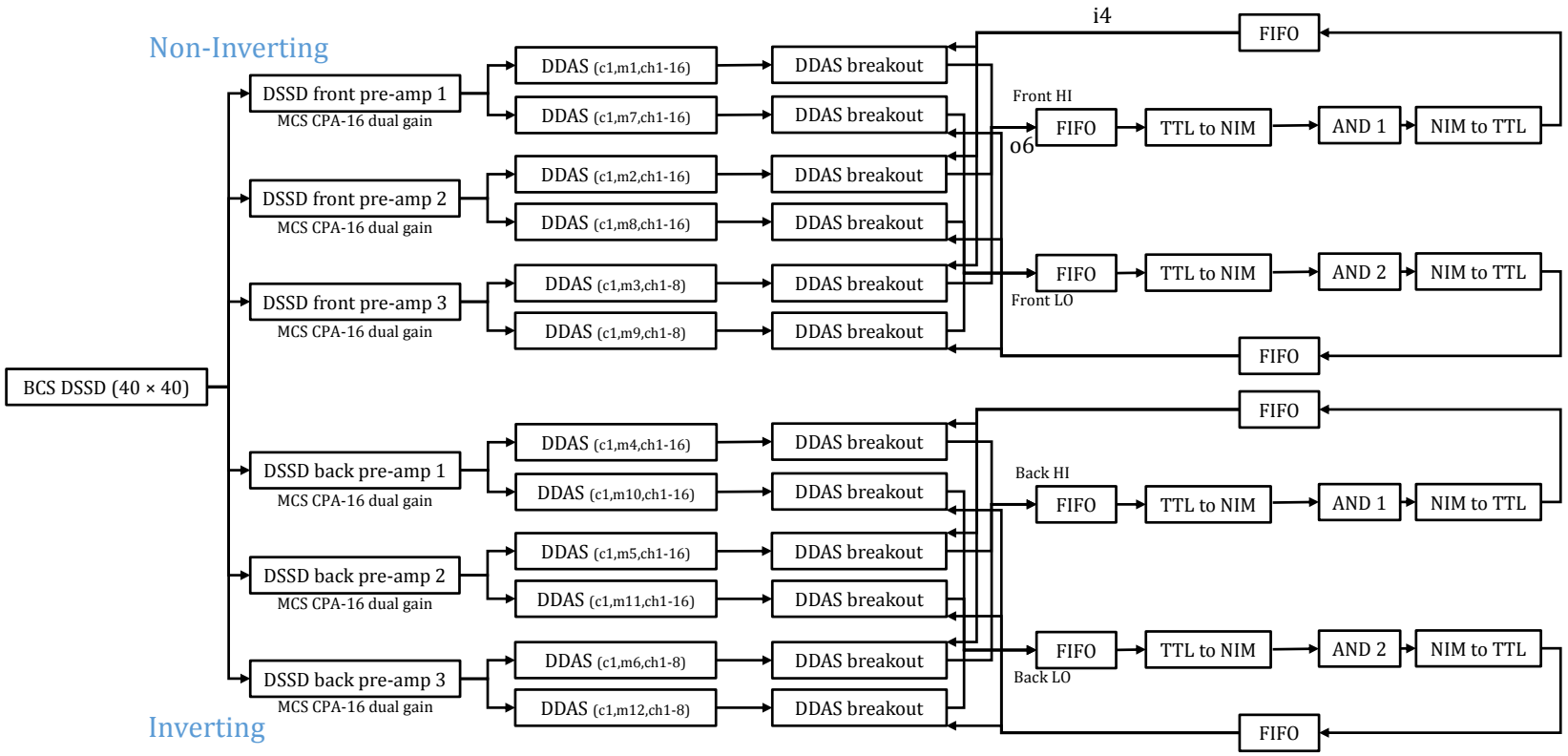

Figure 2.8: BCS DSSD electronics logic.

2.7.2 SuN set-up

For the SuN set-up, the beam line vacuum was vented and the beam tube and the BCS chamber were removed so that the SuN miniDSSD could be installed. Behind the miniDSSD was a Si barrier detector which functioned as a veto for the light particles and punchthroughs. At the same time, the passive degraders in the PIN flange in the cross located upstream were replaced for a thicker set of 2300 μm thickness, shown by LISE to provide the optimal implantation depth of ^{61}V. The list of detectors and degraders in the SuN set-up is listed in Tab. 2.3. A schematic of the SuN layout is shown below in Fig. 2.9.

Si PIN Stack		
Detector	Thickness (μm)	Voltage (V)
PIN1	525	40
PIN2	1041	75
Al Degrader	2300	-

SuN Stack		
Detector	Thickness (μm)	Voltage (V)
DSSD	979	280
Veto	982	-210

Table 2.3: List of detectors and properties used in the SuN set-up.

The data acquisition electronics are shown in Fig. 2.10. For a valid SuN signal to be recorded, the three PMTs in each segment had to fire within a 0.5 μm coincidence window. The summing module acts as a 24 channel OR for the CFD to get the time of any SuN triggers. Similar to that of the BCS DSSD, there was also a coincidence condition for the miniDSSD where a signal had to be recorded from both a front strip and a back strip to be recorded. There were no external triggering conditions for any of the other detectors.

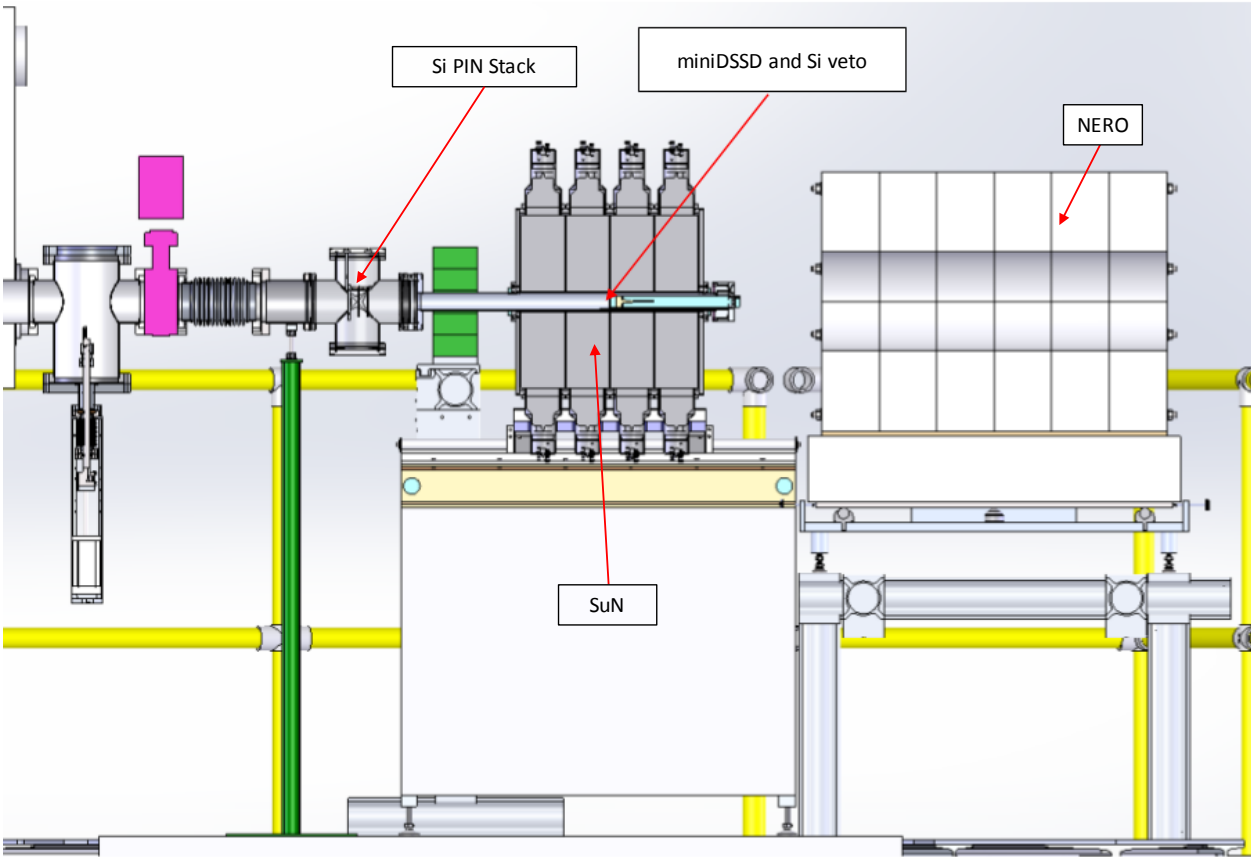

Figure 2.9: A cartoon showing the components of the set-up for the SuN portion of the experiment. Here, the BCS chamber has been removed from the set-up, indicated by the hollow bore of NERO.

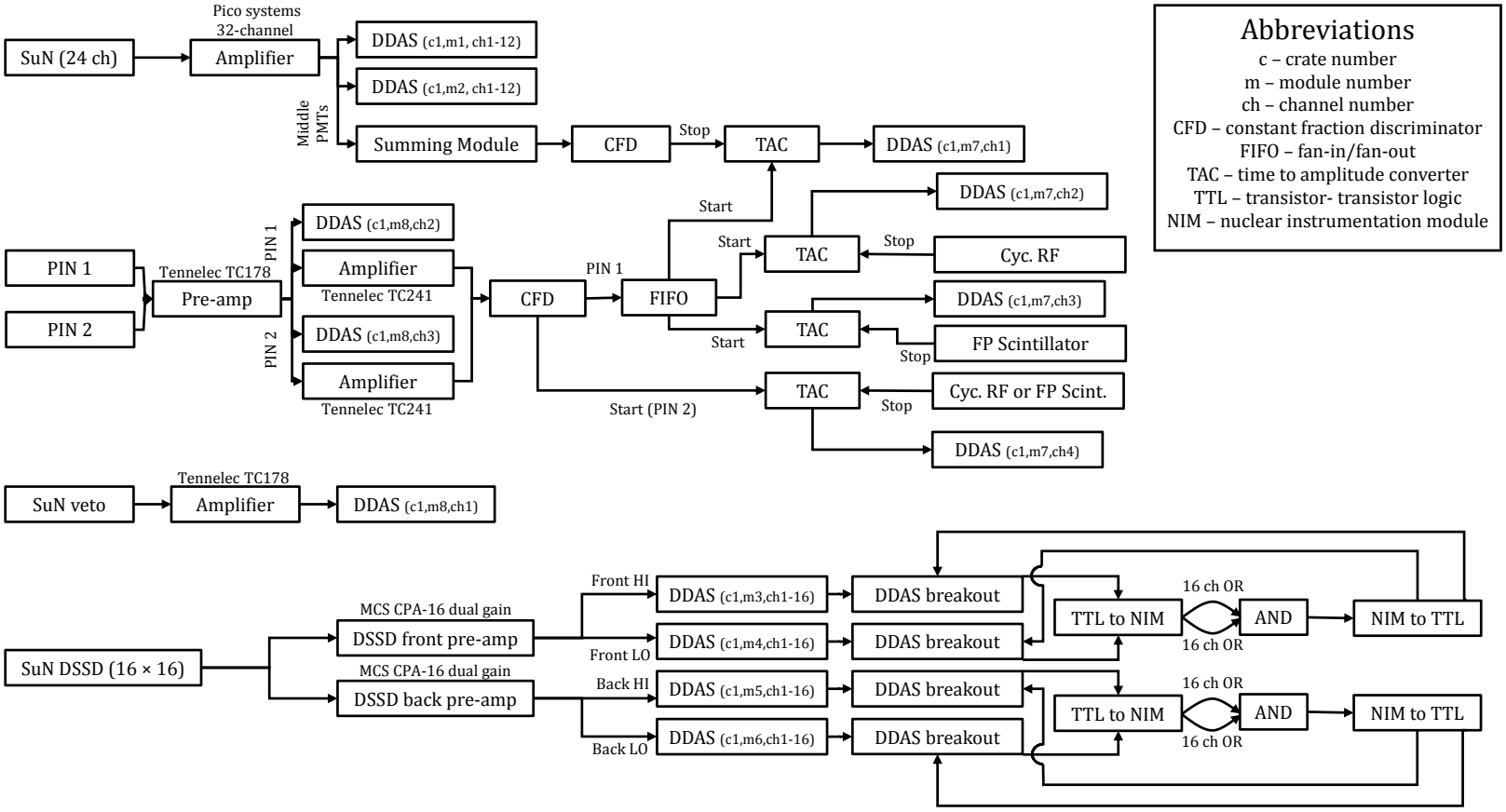

Figure 2.10: SuN electronics logic.

Chapter 3

Data Analysis

3.1 Calibrations

3.1.1 NERO Efficiency

A ^{252}Cf source efficiency measurement was performed using the same ^{252}Cf source (NSCL source ID Z7153) used in NERO efficiency measurements in [56] and [57]. ^{252}Cf produces neutrons through spontaneous fission, with a spontaneous fission branching of 3.39% and 0.116 neutrons/decay [58]. The source had a nominal activity of 50 μCi on November 19$^{\text{th}}$ 1990, but this value only takes into account the presence of ^{252}Cf. In addition to ^{252}Cf, there are two other main contributors to neutron production in the source, ^{250}Cf, which also produces neutrons following spontaneous fission (0.0027 n/decay) [59], and ^{248}Cm (the α decay daughter of ^{252}Cf), which produces neutrons at a rate of 0.2611 n/decay [59]. Since the nominal value of the source has a large error bar of 10 %, a more precise value of the source neutron activity has to be determined for a precise efficiency calibration of NERO.

The total source α activity, together with knowledge of the original source isotopic composition, can be used to determine the neutron activity on any date thereafter. The most recent α calibration of Z7153 was performed in October 2014. Tab. 3.1 shows the source properties on December 1$^{\text{st}}$ 1989 and on this date.

The α activity of the source was measured using a Si barrier detector with an active

December 1st 1989		October 16th 2014		
Nuclide	Amount (atom %)	Nuclide	Amount (atom %)	Neutron Activity (s^{-1})
^{249}Cf	7.32	^{249}Cf	6.972	0
^{250}Cf	13.11	^{250}Cf	3.506	49.8
^{251}Cf	4.55	^{251}Cf	4.463	0
^{252}Cf	75.02	^{252}Cf	0.110	331.7
^{245}Cm	0	^{245}Cm	0.351	0
^{246}Cm	0	^{246}Cm	9.583	0.1
^{247}Cm	0	^{247}Cm	0.087	0
^{248}Cm	0	^{248}Cm	74.907	3.9

Table 3.1: Isotopic composition of the source on the source preparation date (left, provided by source manufacturer) and on the α calibration date (right, calculated).

area of radius 0.5 cm at a distance of 0.62 cm. After correction for the geometric efficiency of the Si detector [60], the α activity of the source was 22964/s. Taking into account the contributions of other α-emitting nuclides in the source, the total neutron activity on the date of α calibration was calculated to be 385.4 n/s, with 49.8 n/s from ^{250}Cf, 331.7 n/s from ^{252}Cf, and 3.9 n/s from ^{248}Cm. This calibration is increasingly important as the source ages because the proportion of neutron activity from ^{250}Cf and ^{248}Cm will increase (compare Tab. 3.1 and Tab. 3.3) and ignoring these sources of neutrons will lead to an inaccurate efficiency measurement.

In the presence of electronics-induced noise, the efficiency of NERO depends on the hardware thresholds used. Example spectra from a ^{3}He tube and a BF_3 tube are shown in Fig. 3.1. In some cases there was a clear separation between the noise peak and the neutron signals, but this was not true for all of the tubes. For the experiment, the hardware threshold was set so that the noise peak was visible. These noise signals were then eliminated by the use of software thresholds in analysis on a run-by-run basis. The software thresholds were set at the minimum point between the low-frequency noise peak and the neutron signals if

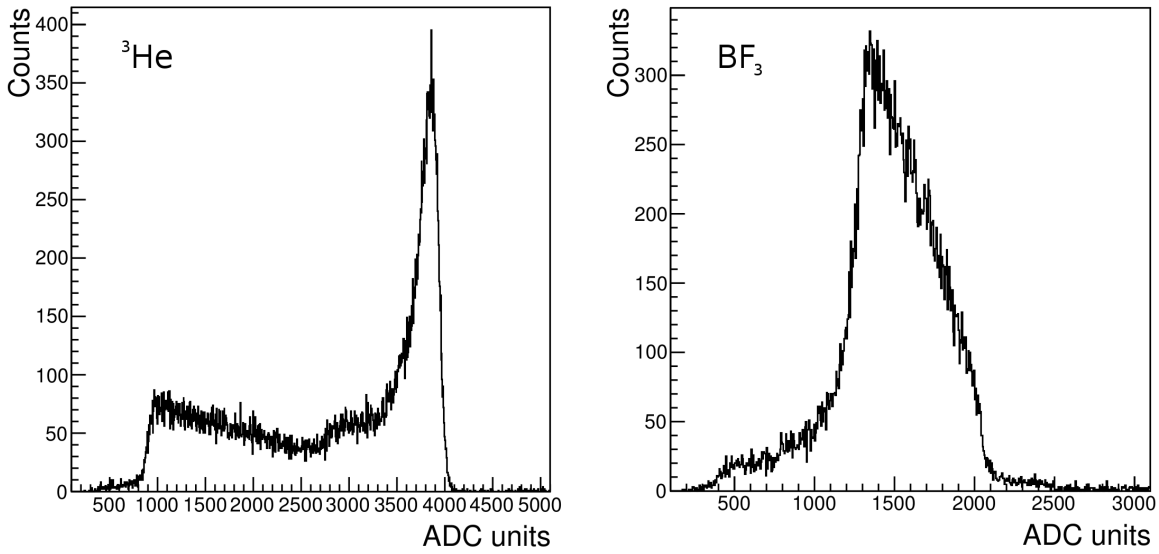

Figure 3.1: Left: Spectrum from a representative ^{3}He tube. Right: Spectrum from a representative BF_3 tube.

Quadrant	Rate (n/s)
A	1.1
B	0.4
C	0.4
D	0.3
Total	2.2

Table 3.2: NERO detection rate of neutrons for a representative background run during the experiment.

there was not good separation, and at the beginning of the neutron signals if there was good separation.

The rate of background neutrons was also investigated. Tab. 3.2 gives the neutron count rate per quad, applying the same software thresholds, for a representative background run during the experiment. This background rate was used to determine the level of false β-n correlations, where a true β decay is correlated to a background neutron, when the β decay curve is fit to extract the number of true β-n events.

The background-subtracted NERO efficiencies by quadrant before and after the experi-

ment are listed in Tab. 3.3. The total NERO efficiencies for a ^{252}Cf source were measured at 31(5) % (before) and 32(2) % (after). The efficiencies are very similar, with the biggest difference from the change in quadrant C BF_3 efficiency due to a detector which was not working in the calibration before the experiment that was fixed prior to the experiment. The larger error bar from the pre-experiment efficiency measurement comes from the assumption that the broken detector could contribute up to the average of the other detectors in the same ring. These measurements are compatible with the value of 31.7(2)% reported in [48] which is considered the benchmark efficiency for ^{252}Cf. Therefore, the same scaled efficiency factor of 37(5) % as in [57] was used in the calculation of the P_n value.

Before			After		
Nuclide	Amount (atom %)	Neutron Activity (s^{-1})	Nuclide	Amount (atom %)	Neutron Activity (s^{-1})
^{249}Cf	6.96	0	^{249}Cf	6.96	0
^{250}Cf	3.36	47.7	^{250}Cf	3.35	47.6
^{251}Cf	4.46	0	^{251}Cf	4.46	0
^{252}Cf	0.09	267.6	^{252}Cf	0.088	265.1
^{245}Cm	0.36	0	^{245}Cm	0.36	0
^{246}Cm	9.74	0.1	^{246}Cm	9.74	0.1
^{247}Cm	0.09	0	^{247}Cm	0.09	0
^{248}Cm	74.93	3.9	^{248}Cm	74.93	3.9
Quadrant	^{3}He (%)	BF_3 (%)	Quadrant	^{3}He (%)	BF_3 (%)
A	3.06	4.57	A	3.17	4.88
B	2.99	5.06	B	3.05	5.20
C	3.07	4.59	C	3.14	5.26
D	2.80	4.72	D	2.74	4.89
Total	11.92	18.94	Total	12.10	20.23

Table 3.3: Source characteristics and NERO efficiencies by quadrant and detector type before (left) and after (right) the experiment.

3.1.1.1 Moderation time of neutrons in NERO

Because the β-delayed neutrons are moderated by the NERO polyethylene matrix (according to Eq. 2.20) before detection in the proportional counter tubes, the time delay of neutron detection following the detection of the β-decay electron is significant, unlike for β-delayed γ rays. Therefore, the moderation time of neutrons in NERO must be considered for the successful correlation of neutron detections to β decay events. Fig. 3.2 shows the time difference between a β decay signal and the neutron detection by a tube in NERO demonstrating that 98.4% of neutrons are detected within a 200μs window of the β decay event. Therefore, during the analysis, all neutrons arriving within a 200 μs window following the detection of a decay signal (defined in section 3.3) were considered to be β-n events.

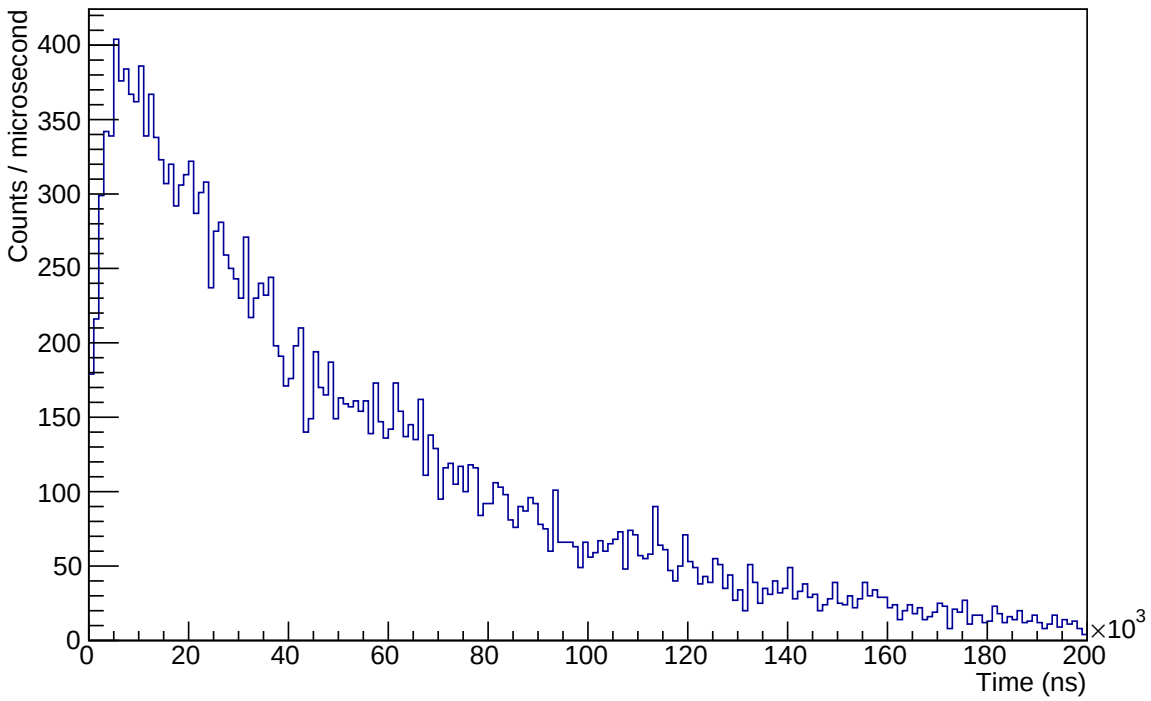

Figure 3.2: Moderation time of neutrons in NERO. The time for half the neutrons to be detected is ∼34 μs.

3.1.2 SuN Energy Calibrations

Each SuN segment is read out by three PMTs which must be gain-matched so that each PMT reads out the same signal voltage when receiving the full light from the detection of a specific a γ ray. This is so that the energies detected in each PMT can be summed together correctly. Gain-matching was done using the 1460 keV line from ^{40}K in the room background which will not produce strong geometric effects in the PMT spectra, which using a source at the centre of the SuN detector would [61]. First, the PMTs were gain-matched by adjusting the PMT voltages until the peaks in the spectra from the three PMTs in a segment overlapped (Fig. 3.3).

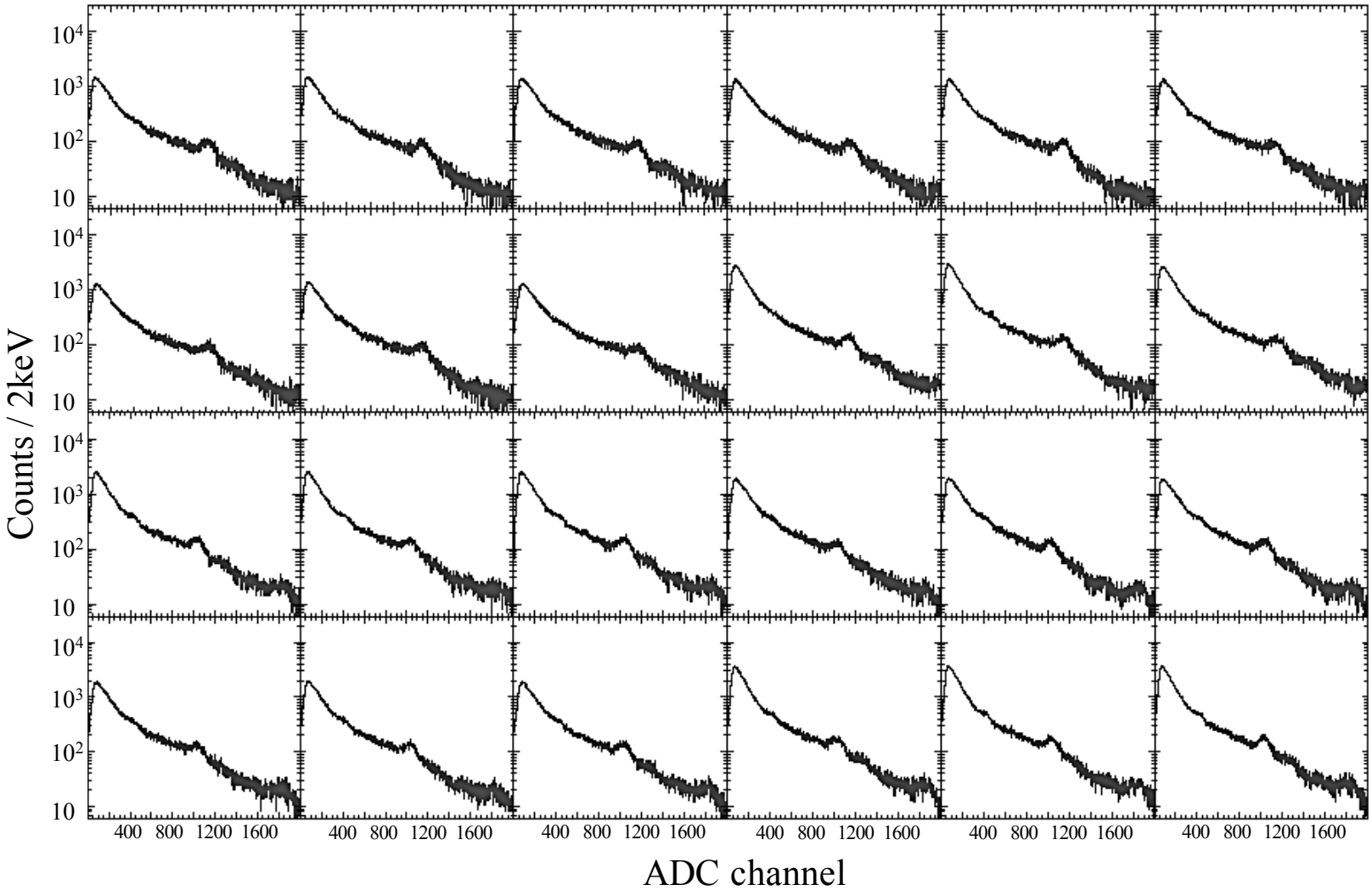

Figure 3.3: Gain-matched room background spectrum for all 24 PMTs of SuN. The peak at ∼1000 ADC units is the 1461 keV line from the decay of ^{40}K in the room background.

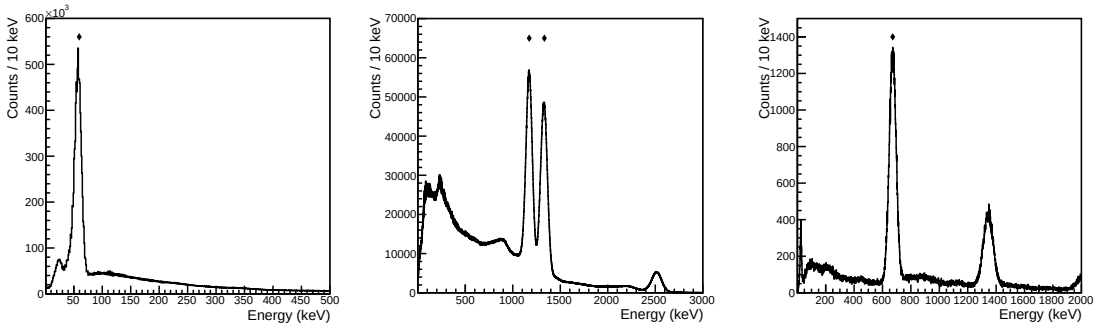

Figure 3.4: The source γ rays used for the calibration of SuN from ^{241}Am (left), ^{60}Co (centre), and ^{137}Cs (right), marked by diamonds. The second peak in the ^{137}Cs spectrum is produced by two γ rays at 662 keV from two separate decays being detected by the same segment, and is a result of the high activity of the ^{137}Cs source used.

The SuN segments were also calibrated so that the ADC units of the energy recorded by the energy filter of DDAS matched the energy of the γ ray in keV. Four lines from three sources were used for this calibration, the 59.5 keV line from ^{241}Am, the 661.7 keV line from ^{137}Cs, and the 1173 keV and 1332 keV lines from ^{60}Co (Fig, 3.4).

The calibration was applied using a linear least squares fit to the position of the four peaks, determined using a Gaussian fit, for each segment. Calibrations were performed both before (Fig. 3.5) and after (Fig. 3.6) the experiment to ensure that the effects of any voltage drift of the PMTs throughout the experiment were taken into account during the analysis.

3.1.3 Silicon Detector Calibrations

3.1.3.1 Energy calibration and resolution of PIN detectors

For the Si PIN detectors to be useful for particle identification, the energy resolution has to be sufficient to distinguish between the different components of the incoming beam. According to LISE++ [45] calculations, a $\Delta E/E$ resolution of less than 3% was necessary to separate all beam components. The energy calibrations and resolutions of the primary par-

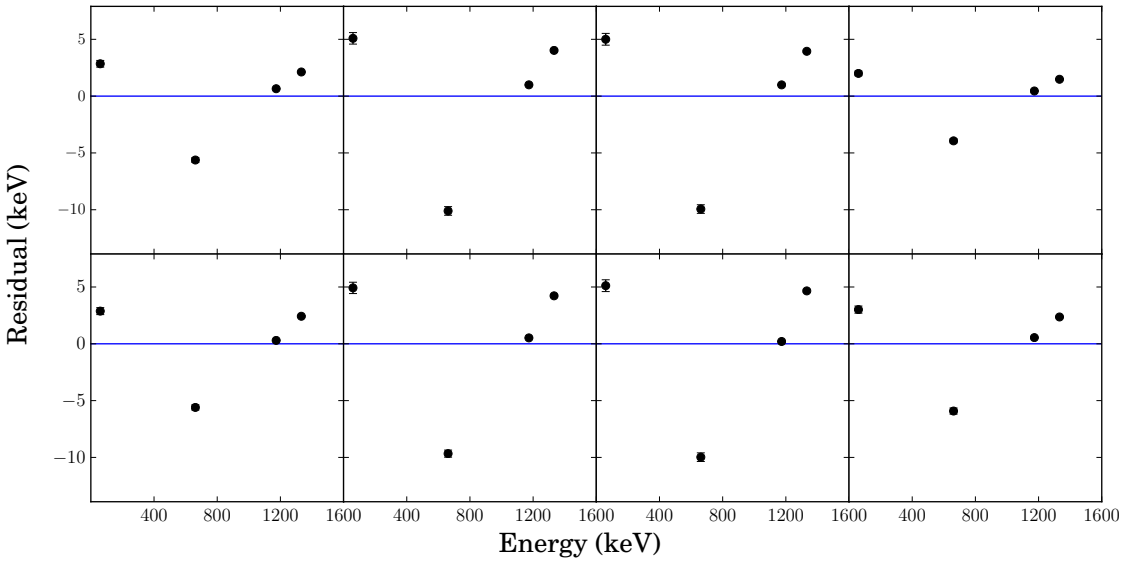

Figure 3.5: Calibration residuals for all 8 segments of SuN for the energy calibration from before the experiment.

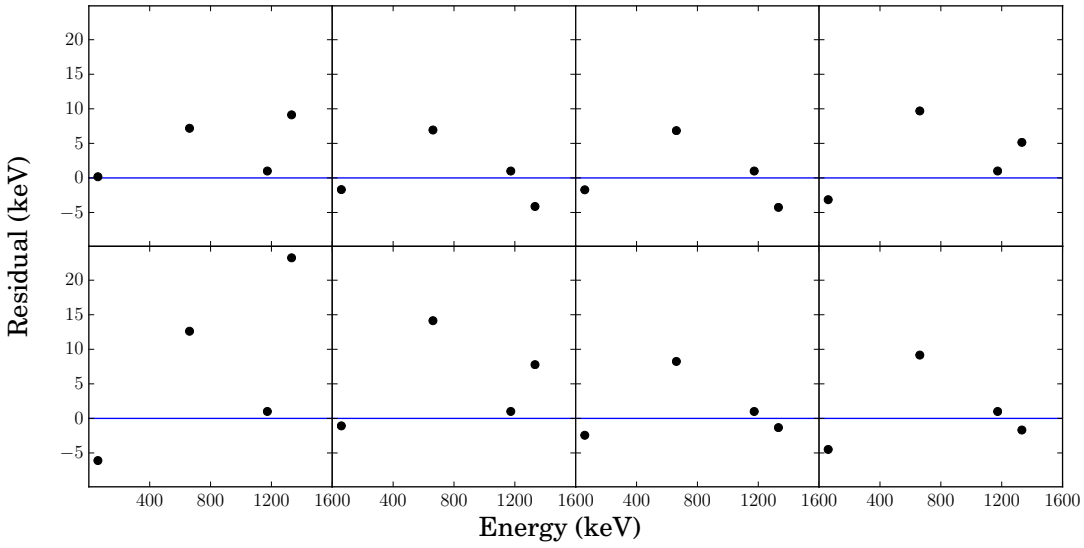

Figure 3.6: Calibration residuals for all 8 segments of SuN for the energy calibration from after the experiment.

ticle identification PINs (1 and 2) were determined with an ^{241}Am source, which has two visible α lines at 5442.80(13) keV an 5485.56(12) keV which require a 0.8% resolution to separate. The DDAS energy filter rise and flat top parameters were adjusted to achieve the best resolution possible for the stronger 5485.56 keV α line and are listed in Tab. 3.4. Although the resolution required to separate the two α lines was not achieved, the resolution was good enough for the purpose of particle identification (also listed in Tab 3.4). The calibrations and resolutions of PINs 3,4, and 5 were determined using a ^{228}Th source, which has 6 well-known α lines of energy 5.4-8.8 MeV from α decay of ^{228}Th and nuclei in the daughter chain (Fig. 3.7). The signals from PINs 1, 2, 3, and 4 were passed through a Tennelec 4-channel (TC-178) pre-amiplifier unit, which has three gain settings of 100 MeV, 1 GeV, and 10 GeV. Based on LISE++ calculations of the amount of energy expected to be desposited in each PIN detector (300-900 MeV), the pre-amplifier settings for all four low-gain PINs for the experiment were set to 1 GeV. On this gain setting, a $\sim$5 MeV α would not produce detectable signals. Thus, for these PINs, the resolution optimisation and energy calibrations were performed with the 100 MeV gain setting and assumed to hold for the 1 GeV gain setting. The poor energy resolution of PINs 3 and 4 are caused by noise in the pre-amplifier channels used. This did not end up affecting the analysis, since PIN3 and PIN4 were used to confirm transmission through the BCS chamber to the BCS DSSD rather than precise particle identification.

3.1.3.2 Calibration of DSSDs

Energy calibrations of the high-gain channels of both the BCS DSSD (and SSSD) and the miniDSSD were determined using a ^{228}Th source. Signals from the different DSSD strips were gain matched to facilitate the position distribution. A linear least squares fit was

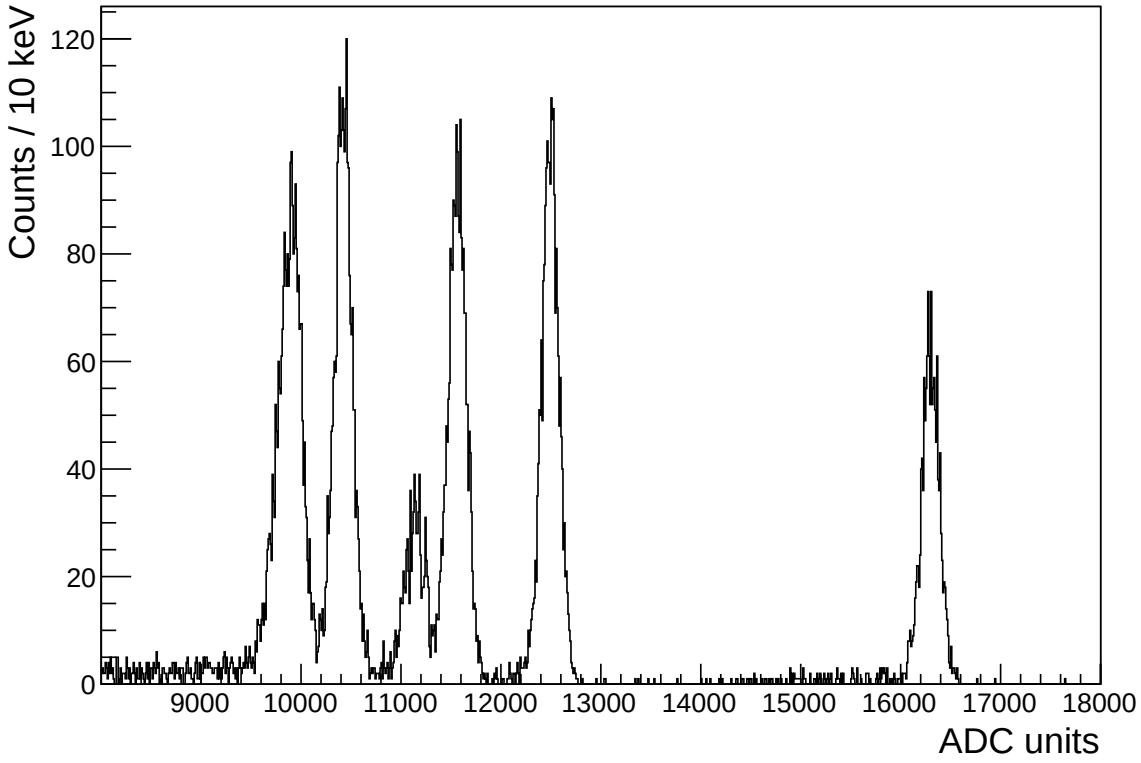

Figure 3.7: ^{228}Th spectrum. The six α peaks from the decay chain are at 5.42, 5.69, 6.05, 6.29, 6.78, and 8.78 MeV.

Detector	Rise time (μs)	Flat top time (μs)	FWHM resolution (%)
PIN1	9.52	0.640	1.2
PIN2	9.52	0.640	2.24
PIN3	9.52	0.640	10.1
PIN4	9.52	0.640	4.25
PIN5	4.96	0.240	1.8

Table 3.4: DDAS slow filter parameters and highest achieved energy resolution of the PIN detectors.

performed for the energy vs channel data for the 6 α lines from the ^{228}Th source (Fig. 3.7). The residuals of the calibration for the ^{228}Th source measurements for the BCS DSSD and SuN miniDSSD are shown in Figs. 3.8 (front) and 3.9 (back), and 3.10 respectively. The offsets for the calibration were at a reasonable level of $\sim$100-200 keV at ADC channel 0.

The low energy thresholds were set by using a ^{90}Sr source, which has a well-known β-decay electron spectrum. The thresholds were set high enough such that it minimised the inclusion of noise as false β decay signals, but as low as possible to include as many true β decay signals as possible (Fig. 3.11). The low-gain channels of the DSSDs could not be tested using sources before the experiment since source αs are not energetic enough, so these were gain-matched online with the energy deposition by beam particles.

3.1.4 Light Particle Veto Calibrations

For the NERO portion of the experiment, the thick plastic scintillator downsteam of the SSSD was used as the light particle veto. The light particles which come with the beam are much more energetic than the β decay electrons, but mimic β decay signals in the comparatively thin DSSD and SSSD. However, the LISE prediction for the energy deposited in the scintillator by the light particles is much higher (>50 MeV) than the β decay Q-value of ^{61}V ($\sim$12 MeV), and gating out the high energy portion of the scintillator spectrum helps

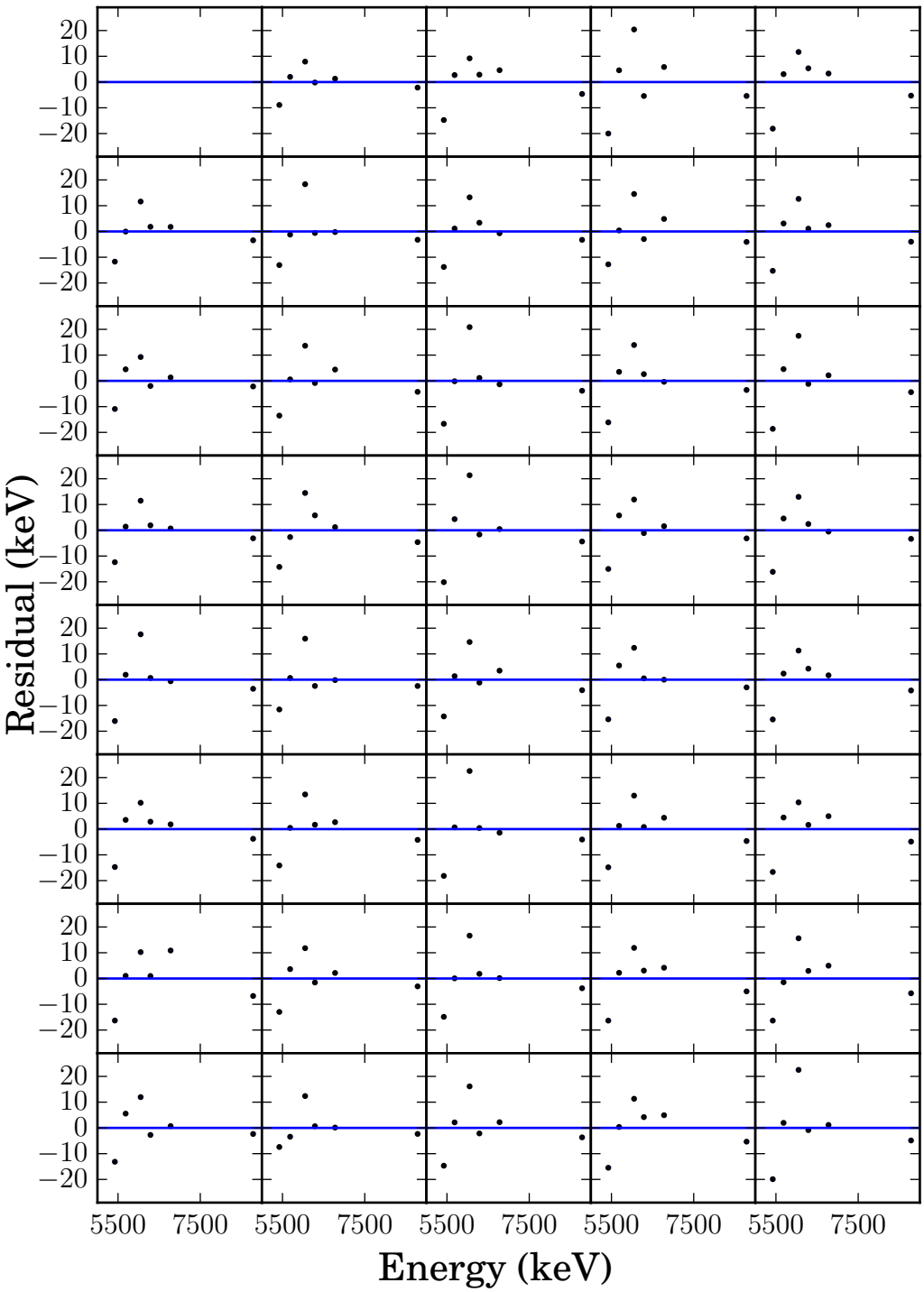

Figure 3.8: BCS DSSD front side calibration residuals with a ^{228}Th source. Strip 1 shows no residuals as it was not operational due to a broken contact.

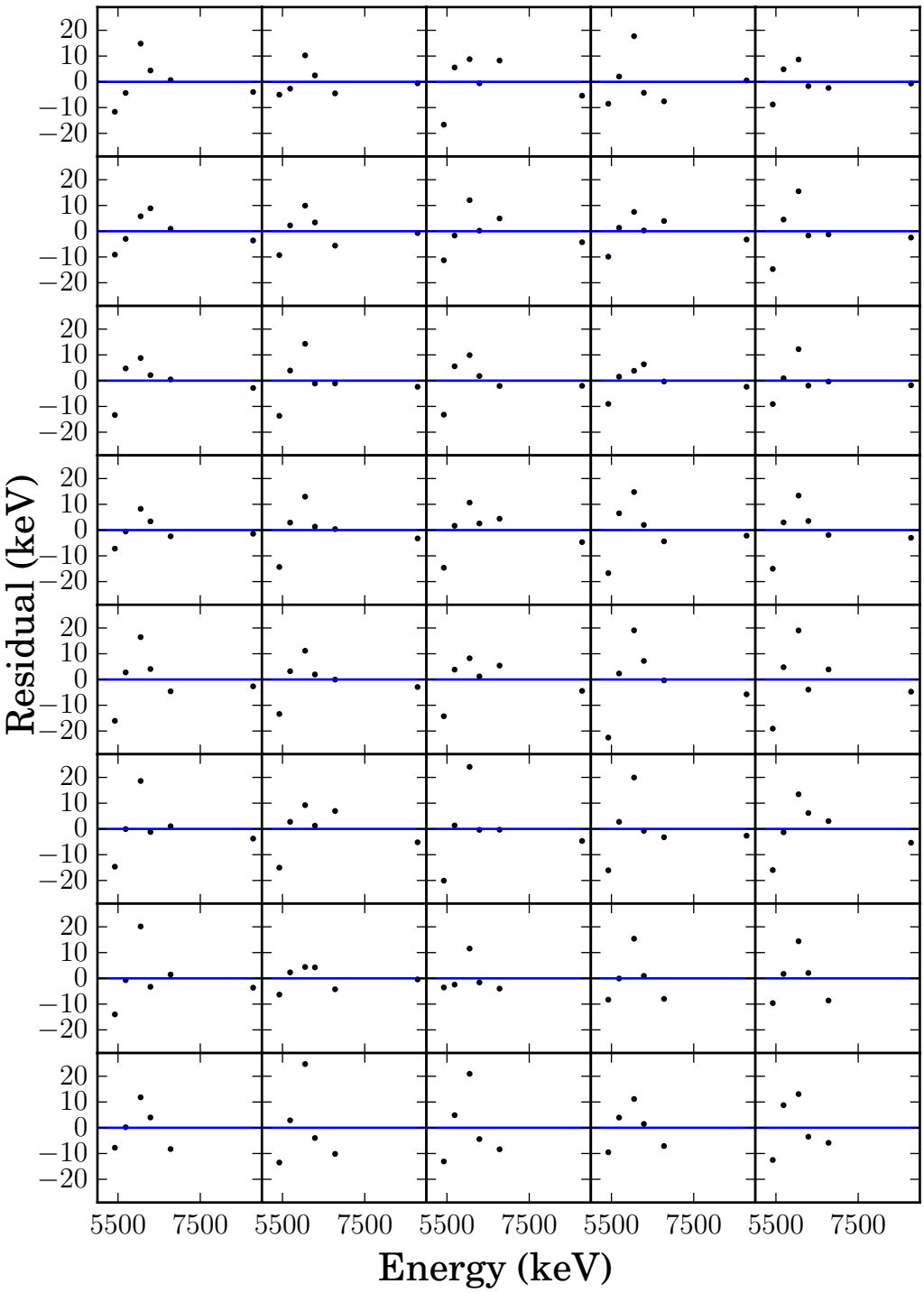

Figure 3.9: BCS DSSD front side calibration residuals with a ^{228}Th source. The shared pre-amlifier for strips 33-40 had a gain high enough that the 8.8 MeV α from ^{228}Th was outside the ADC range.

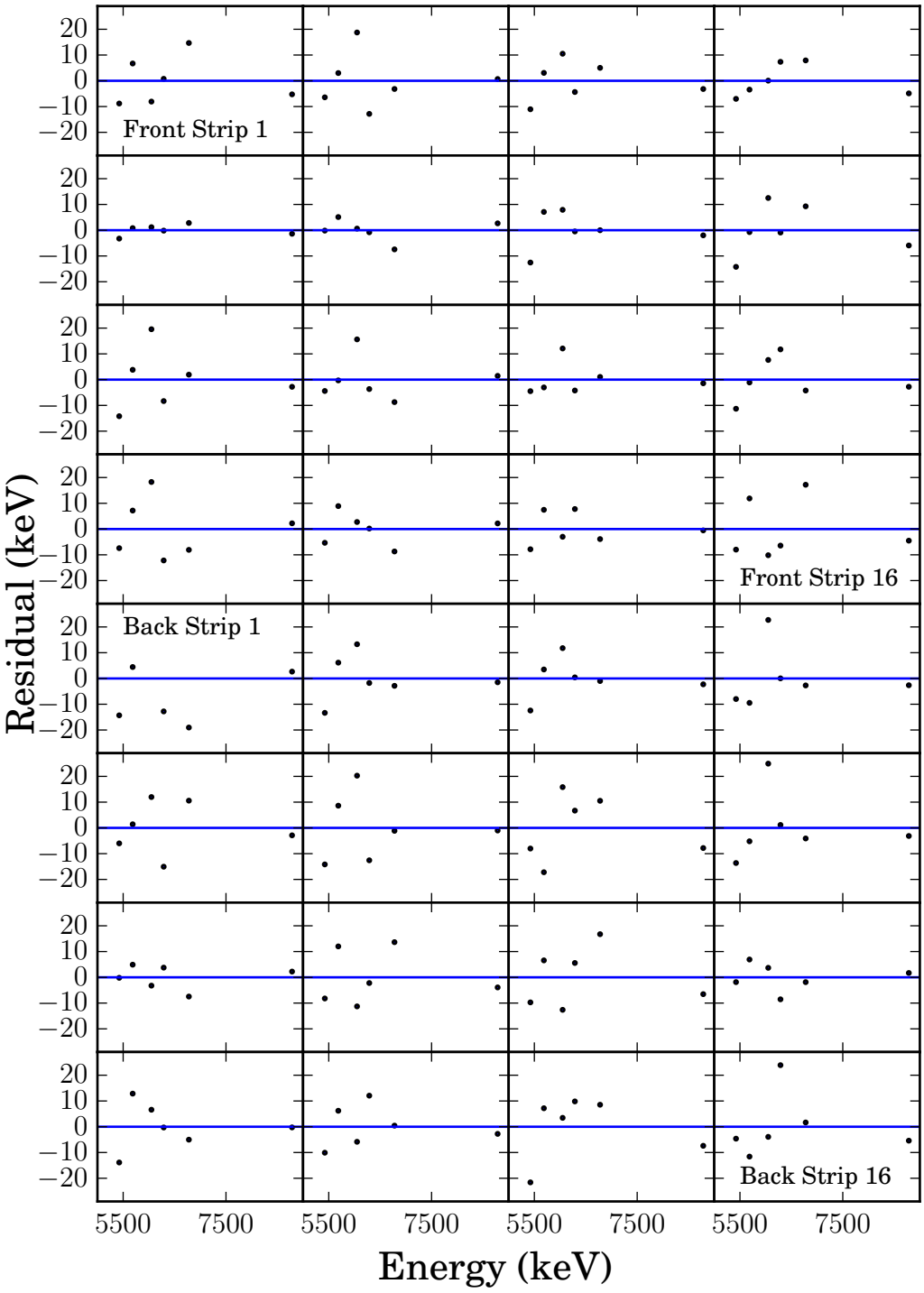

Figure 3.10: SuN miniDSSD front side (top four rows) and back size (bottom four rows) calibration residuals with a ^{228}Th source. Strips are ordered left to right, then top to bottom.

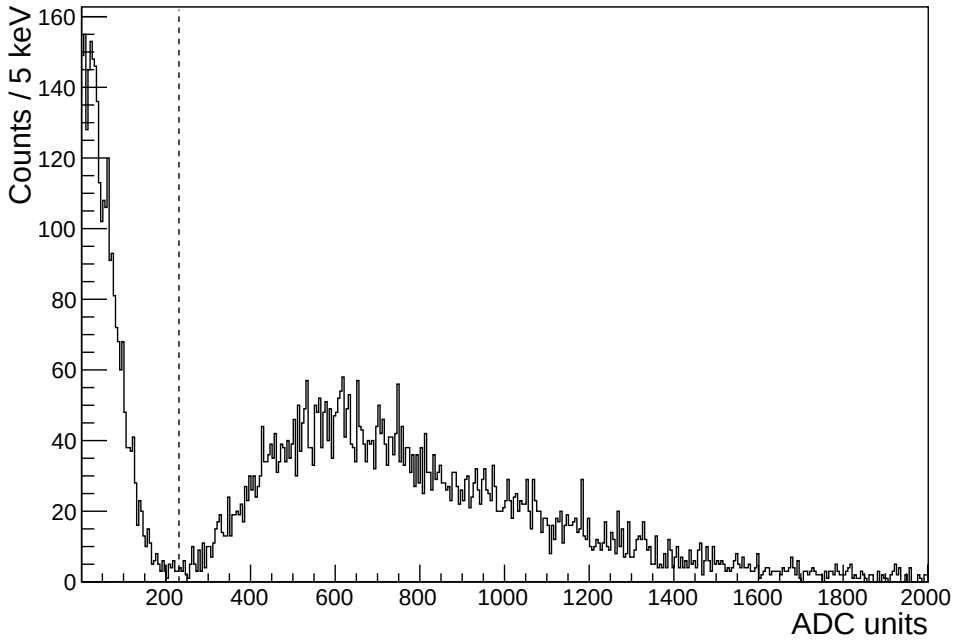

Figure 3.11: ^{90}Sr spectrum in a representative DSSD strip. The threshold used is indicated by the dashed line. The peak to the left is due to electronic noise, and the broad peak to the right is the β spectrum measured from the ^{90}Sr source.

to eliminate the light particles event from the β decay spectrum seen in the DSSD (Fig. 3.12).

3.2 Particle Identification

As previously discussed in section 2.5.2, the particle identification for this experiment was performed using the δE-TOF method. The energy loss ΔE used was the energy loss in PIN1, and the time-of-flight used was the time between a (delayed) signal from the I2 scintillator and a signal in PIN1. The uncorrected PID is shown in Fig. 3.13. The I2 slits were open to allow a momentum acceptance, dp/p, of 2%, and momentum corrections were performed using the position along the I2 scintillator to account for the distribution in the time of flight. This correction was done by assuming that the position in the I2 scintillator was a

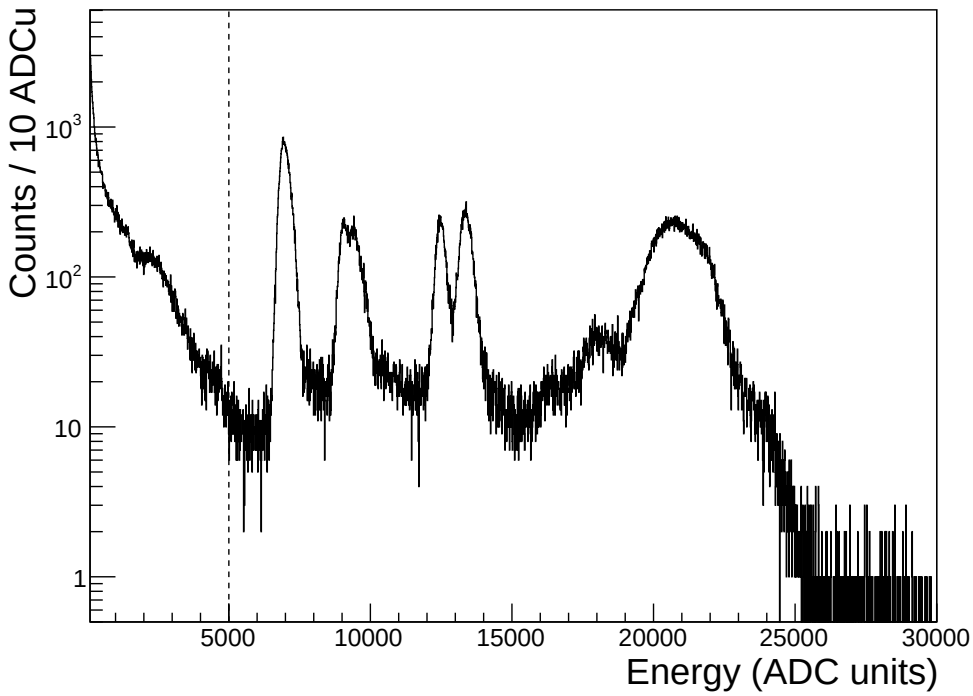

Figure 3.12: Scintillator spectrum for a representative NERO run. The dashed line indicates the 12 MeV upper threshold used to eliminate light particle signals from the DSSD high-gain channels.

linear function of the TOF, and calculating a corrected time of flight which is independent of the position in the I2 scintillator (effectively performing a rotation of the trendline).

In the case of this experiment, the tune was such that the beam contained only a few fragments, and only a single isotope of each element. The cause of the double peak structure in the I2 position spectrum for ^{61}V and ^{64}Mn is uncertain. However, following momentum correction, the double-peaked structure is resolved into a single peak, and the γ ray spectra gated on each peak shows that they are the same isotope. The γ ray spectrum in coincidence with implantation events does not show any isomeric transitions for either ^{64}Mn or ^{61}V. Analysis gates for each isotope were defined by selecting regions in the corrected PID (Fig. 3.13) so that the β decays and β-delayed radiation could be analysed for each isotope separately.

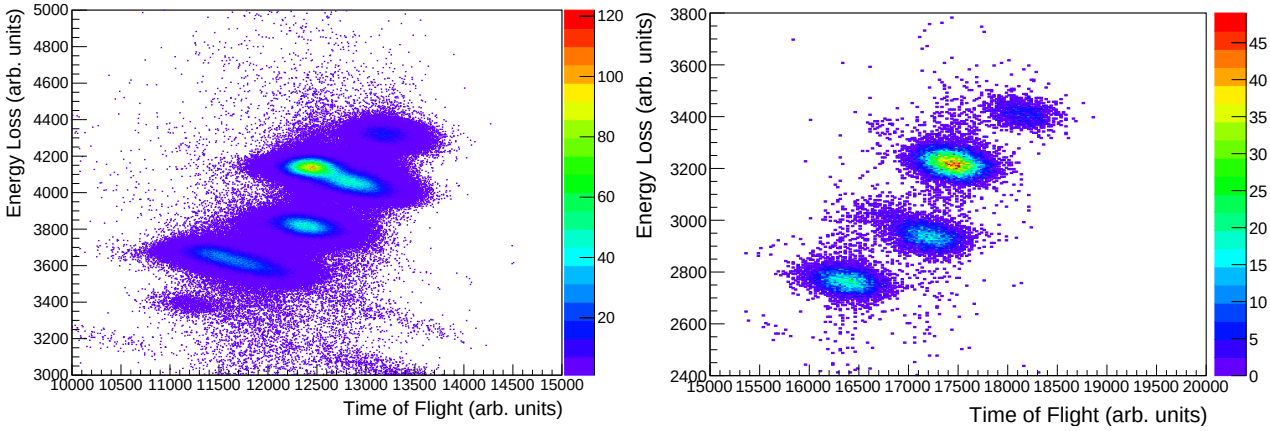

Figure 3.13: Uncorrected (left) and corrected (right) particle identification plots.

3.3 Correlating implants and decays

After being implanted in the DSSD, the beam particle eventually decays and emits an electron. Both the decaying ion, referred to as the implant, and the β decay electron, referred to as the decay, will deposit energy in the DSSD. To be classified as an implant, the following conditions were required: (1) a signal in PINs 1-4; (2) a signal in the low-gain channels of both the front and back side of the DSSD; (3) no signal in the SSSD; and (4) no signal in the plastic scintillator. Events where conditions (1) and (2) are met but (3) is not are considered punchthrough events. These events are excluded because the decay electron from implantation in the SSSD is not localizable by a single SSSD, making correlation challenging.

To be classified as a decay, the following conditions were required: (1) no signal in PINs 1-4; (2) no signal in the low-gain channels of the DSSD; (3) a non-overflow signal in the high-gain channels of the DSSD that also passes the hardware noise thresholds; and (4) a signal in the plastic scintillator under the 12 MeV threshold. Events where conditions (1)-(3) are fulfilled but condition (4) is not are considered light particle events, which otherwise behave the same as β decay events, but have to be vetoed as they can occur at a much higher rate depending on the secondary beam delivered to the experimental end station.

Each time a decay was detected, it was correlated to all implants within the given correlation time window (a time chosen to be ten times the half-life of the decaying parent, 500 ms in the case of ^{61}V) and within the correlation area (defined below) of the decay pixel. This was done to generate a flat random background. If the decay had been correlated only to the most recent implant within its correlation field, this would bias the background toward lower time differences between the implant and decay, and lead to a slowly decaying background.

Correlations between implants and decays are complicated by the fact that other species implanted in the detector can also emit decay electrons, whether they be other components of the implanted beam or daughter nuclei from previously implanted species that undergo further decays. The first problem was dealt with by using gates in the particle identification so that only implants of a certain species are considered. Additionally, fewer false correlations were achieved by choosing an implantation rate where the time between implants is much longer than the half-life of the implanted isotope of interest.

Another strategy used was to utilise the fine pixelisation of the DSSD to spatially localise both the implant and decay, and to correlate implants and decays which are in proximity to each other (since it is likely that the decay electron will be detected near the implant which emits it). Once an implant is localised, the correlation field can be defined to be either the implant pixel itself, or can be widened to include the neighbouring pixels (including diagonally adjacent pixels) to create a 3×3 field of 9 pixels or a 5×5 field of 25 pixels. The presence of a high-gain signal (not vetoed by the light particle vetoes) in any of the pixels in the correlation field is then considered a correlated β decay electron.

The maximum rate of implants of major beam species in correlation fields of different sizes for a representative run during experiment is given in Tab. 3.5. For a 3×3 pixel^2 correlation field, the average time between implants for ^{61}V is ∼15000 ms, or about 300

Species	Correlation field size	Rate of implantation (ms^{-1})	Implantation efficiency
^{61}V	1×1	1.2×10^{-5}	80%
^{61}V	3×3	6.6×10^{-5}	
^{62}Cr	1×1	1.5×10^{-5}	86%
^{62}Cr	3×3	8.7×10^{-5}	
^{64}Mn	1×1	3.6×10^{-5}	76%
^{64}Mn	3×3	1.5×10^{-4}	

Table 3.5: Rate of implants for the major beam species at the centre of the position distribution in the plane of the detector in different correlation field sizes. The implantation efficiency (fraction of implants to beam particles) for each species is also given.

times longer than the half-life of ^{61}V. This is a sufficiently large time between implants to minimise ambiguities in correlating decay events to implantation events.

The decay electrons and implants typically cause more than one strip on each side to trigger, and were localised based on the distribution of energy in the front and back strips. The implants deposited energies on the order of 2 GeV in the DSSDs and the ranges of the pre-amplifiers were not large enough such that the implant signals frequently overflowed. This prevented localisation of the implant by simply selecting the strips with the highest energy deposition. Instead, two different procedures were used: (1) the central of the set of consecutive overflowed strips was selected if the number of overflowed strips is odd and randomly selected from the central two of the set of strips if the number of overflowed strips is even, referred to as C_{of}; and (2) the energy-weighted average strip number was selected (overflowed strips were assigned the value 32767, the maximum of the 16 bit range), referred to as C_{wa}.

$$C_{wa} = \frac{\sum_{i=0}^{i=39} iE_i}{\sum_{i=0}^{i=39} E_i} \tag{3.1}$$

For all correlated events, C_{of} and C_{wa} were the same or adjacent to each other. Similarly

for the decays, localisation was used by taking the strip with the highest energy deposition in the front and the back. There was no need to perform the same procedure as was done for the implants because the high-gain signals did not overflow the range of the pre-amplifier. The spatial distributions (in the plane of the detector) of correlated β decays for the BCS DSSD and the miniDSSD are shown in top row and bottom row of Fig. 3.14 respectively. The procedures used to determine the positions of the implants and decays can be checked by determining the correlation efficiency (section 3.3.1) and were found to be appropriate.

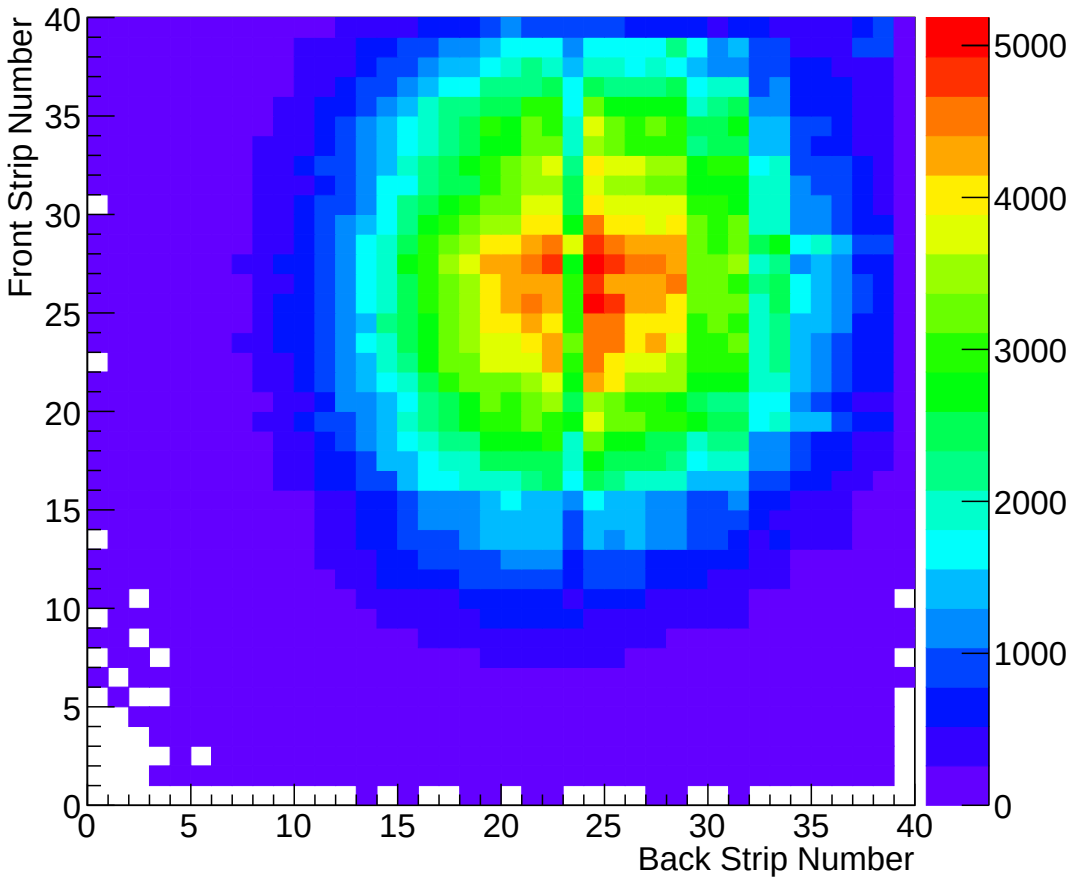

Figure 3.14: The spatial distribution of correlated ^{61}V decays in the BCS DSSD. The low-event strip in the middle is due to a noisy channel with a high threshold.

The total number of implants and correlated decays are given in Tab. 3.6.

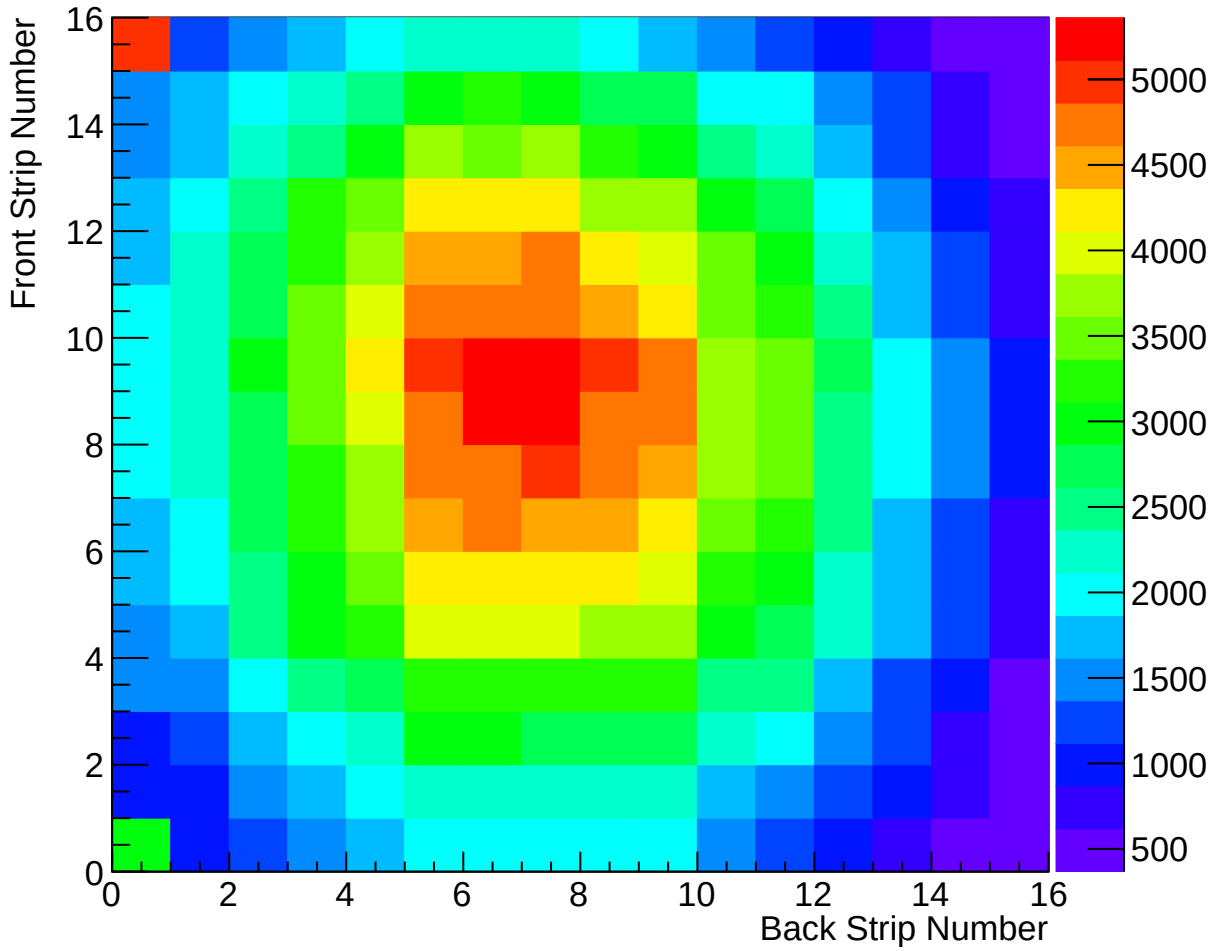

Figure 3.15: The spatial distribution of correlated ^{61}V decays in the miniDSSD.

3.3.1 β Correlation efficiency

The β correlation efficiency refers to the fraction of detected β decays correlated to an implantation event, and includes both the detection and correlation efficiencies. Experimentally, the Bateman equations have to be corrected by the β correlation efficiency for each isotope, such that

$$N(t) = \epsilon N_0 e^{-\lambda t} \tag{3.2}$$

$$N'(t) = \epsilon' N'_0 e^{-\lambda' t} - \epsilon N_0 \frac{\lambda}{\lambda' - \lambda}\left[e^{-\lambda' t} - e^{-\lambda t}\right] \tag{3.3}$$

BCS DSSD

Isotope	Implants	Correlated Decays	Efficiency
^{61}V	164736	61847	37.5 (2.0) %
^{62}Cr	154559	59300	38.4 (2.3) %
^{64}Mn	377259	138412	36.7 (1.6) %

SuN miniDSSD

Isotope	Implants	Correlated Decays	Efficiency
^{61}V	1185155	223910	18.9 (1.1) %
^{62}Cr	927977	186584	20.1 (1.2) %
^{64}Mn	3480589	752020	21.6 (1.0) %

Table 3.6: Calculated efficiencies for the correlation of implanted isotopes for the BCS DSSD (top) and the SuN miniDSSD (bottom).

where N, ϵ and N', ϵ' are the number of correlated decays and β correlation efficiencies of the parent and daughter respectively. The β correlation efficiency for all the components of the secondary beam have been determined by taking the ratio of correlated decays ($N(t)$) obtained from the decay curve fit to the number of implanted ions ($N_0(t)$). The β correlation efficiencies of the components of the implanted beam are listed in Tab. 3.6.

A potential cause for differences in efficiencies could be the position distribution of the implants in the plane of the detector. The closer the centroid of the beam spot is to the edge of the detector, the more likely that the decay electrons will not be detected by the DSSD. Fig. 3.16 shows the planar position distribution in the front and back sides of the two DSSDs for the beam components. For the BCS DSSD, there is no significant difference in the beam position between ^{64}Mn and ^{61}V, but the ^{62}Cr beam position is more centred and does not show the same run-off the sides of the detector as ^{64}Mn and ^{61}V, which could account for the slightly elevated correlation efficiency of ^{62}Cr. For the SuN miniDSSD, all three beam positions are encompassed mostly within the miniDSSD, and beam position is thus unlikely to have had an impact on correlation efficiency. Given the similarity of β

	BCS DSSD		SuN miniDSSD	
Size	Efficiency	Signal-to-Background	Efficiency	Signal-to-Background
1×1	14.2 (0.8) %	26.4	18.9 (1.0) %	9.49
3×3	37.5 (2.0) %	8.17	25.9 (1.4) %	3.25
5×5	42.8 (2.3) %	3.51	-	

Table 3.7: Summary of correlation efficiency as a function of correlation field size for both DSSDs. The result for a 5×5 field for the miniDSSD was not included as a reduced χ^2 of below 2 was not achieved by the best fit.

correlation efficiencies for the different beam components studied here and previously [56,62], we fellow the approach in previous work and assumed that the β efficiencies are the same for parent and daughter decays. In this case, the efficiency term in the experimental Bateman equations is simply a scaling factor.

The correlation efficiency will also depend on the size of the correlation field- the efficiency can be increased if the correlation field is widened to a 3×3 pixel^2 field instead of a single pixel field because the decay electron may deposit its energy predominantly in a neighbouring strip, or because the implant was localised incorrectly. This gain in efficiency tapers off as the correlation field is subsequently widened. The trade-off when using a larger correlation field is that the signal-to-noise ratio (defined here as the N_0 term over the background level) will decrease as the background increases at a faster rate than the number of true decay events. Tab. 3.7 lists the correlation efficiencies and signal-to-background ratios for the BCS DSSD for 1×1, 3×3, and 5×5 pixel^2 correlation fields, and 1×1 and 3×3 pixel^2 fields for the SuN miniDSSD. All results in this work were obtained using a 3×3 and 1×1 pixel^2 field for the BCS DSSD and the SuN miniDSSD respectively. For the BCS DSSD, a 3×3 correlation field was chosen because the significant increase in efficiency outweighted the derease in signal-to-noise.

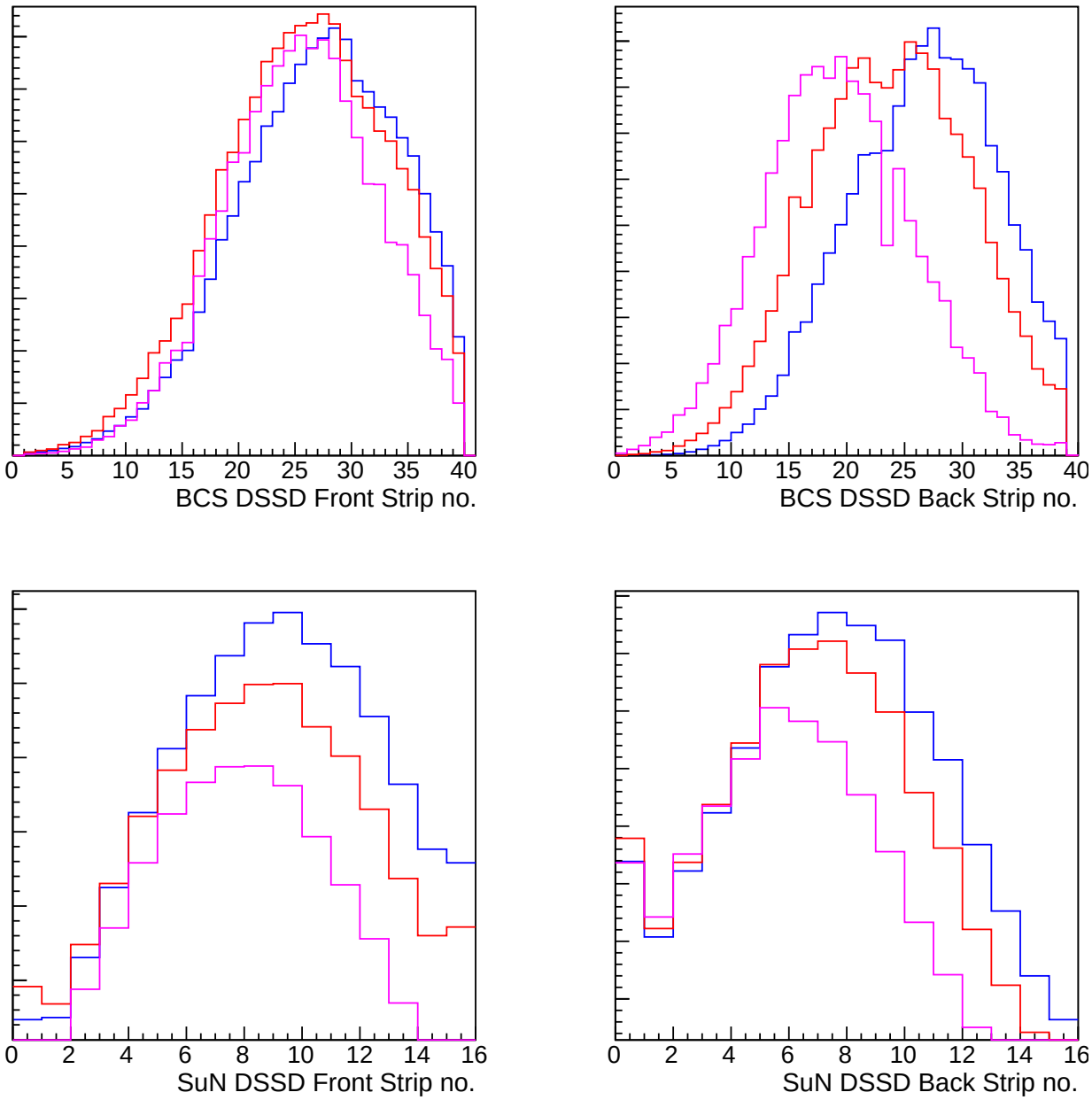

Figure 3.16: Top: Implant distribution for ^{61}V (red), ^{62}Cr (magenta), and ^{64}Mn (blue) for the front (left) and back (right) sides of the BCS DSSD. Bottom: Implant distribution for ^{61}V (red), ^{62}Cr (magenta), and ^{64}Mn (blue) for the front (left) and back (right) sides of the SuN miniDSSD.

3.3.2 Reverse-time correlations

Running the correlation algorithm on the time-reversed event sequence (hereafter referred to as reverse-time correlations) extracts the rate of false correlations, or background. There are many potential sources of background- for example, long-lived nuclei in the decay chain of the implanted nuclei will decay at a much later time, emitting β decay electrons that are then erroneously correlated with newly implanted events; light particles that are part of the incoming beam that were not vetoed by the plastic scintillator. All of these events have different and uncorrelated rates, and therefore should generate a flat background of correlated events. The reverse time correlation should correctly reproduce the same background rate as the forward time correlation.

3.4 Simulating β-delayed radiation in SuN

3.4.1 GEANT4 construction of SuN

A GEANT4 [63] simulation of the SuN set-up, consisting of the SuN detector [61], the beampipe and the miniDSSD [64] was used to analyse the β-delayed γ ray spectra. Because of the low resolution of the SuN detector, it is often impossible to analyse individual γ ray peaks. Furthermore, the purpose of using SuN was to extract the β decay transition strengths by considering the total cascade energy rather than single γ rays. The summing efficiency of SuN is not 100% (for example, the summing efficiency for the 662 keV ^{137}Cs line is 82% [52]), and the summing efficiency will vary from cascade to cascade. Since each excited state can decay through multiple cascades, it is not straightforward and in some cases impossible to determine the population of a given excited state by counting the number of events in a

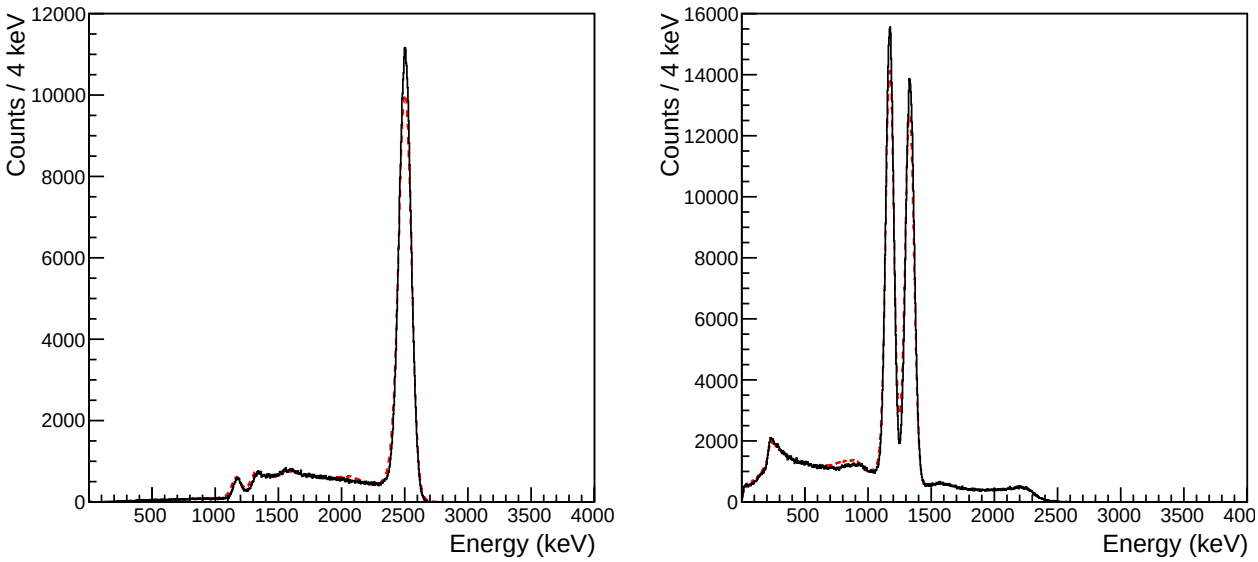

Figure 3.17: Total absorption spectrum (left) and sum of segments spectrum (right) comparing background-subtracted ^{60}Co source data (dashed red), and GEANT4 simulation with a ^{60}Co source (solid black).

given total absorption peak and unfolding the efficiency. Instead, it is more feasible to use the GEANT4 simulation to automatically take the detector response into account.

To ensure that the GEANT4 simulation of the detector is trustworthy, it was benchmarked against a source measurement. Utilising the properties of a well-characterised ^{60}Co source as input to the simulation, the accuracy of the simulation was verified. Fig. 3.17 demonstrates that the GEANT4 simulation does reproduce the measured γ ray sum of segments spectrum, as well as the total absorption spectrum. In Fig. 3.17, the counts in the total absorption spectrum for the simulation was normalised to the counts in the spectrum from the data, since this represents the total number of detected events. Integration of the total absorption peaks for both cases gave a summing efficiency of 61.2(1)% and 62.6(1)% for the data and simulation respectively, in good agreement with the 62.4(1.2)% result from [61]. More details regarding the previous benchmarking of the SuN GEANT4 simulation are discussed in [61].

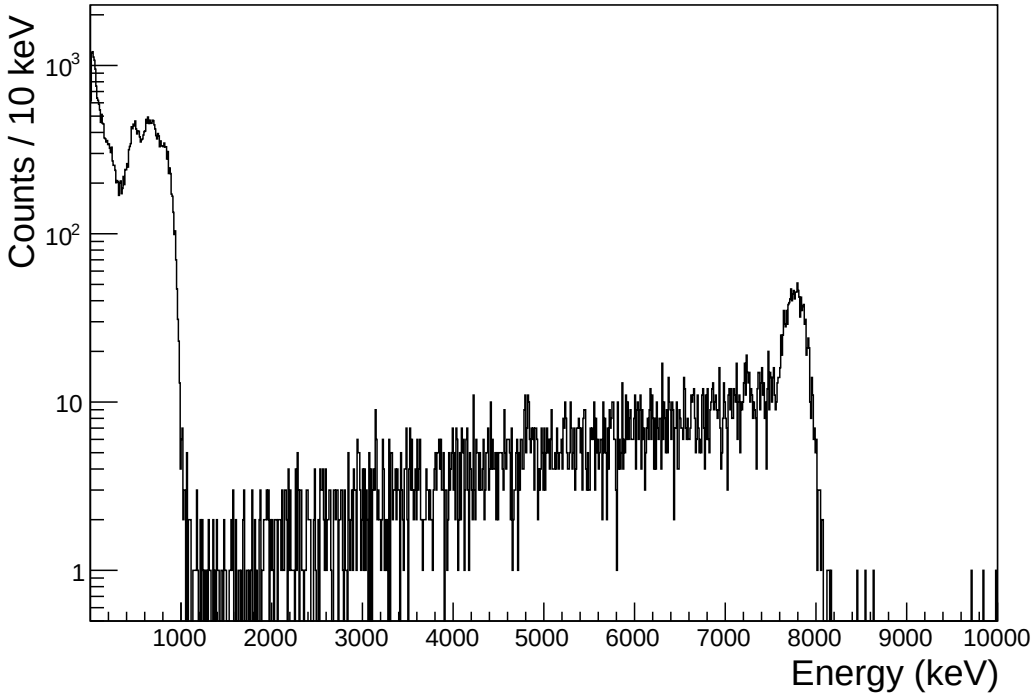

Figure 3.18: Total absorption spectrum for mono-energetic 1 MeV neutrons, showing the sum peak for the inelastic scattering populating the first excited state of ^{127}I where the neutron is not captured and the 7.8 MeV peak from neutron capture on ^{127}I.

3.4.2 Neutron and electron signals in SuN

3.4.2.1 Neutrons

In addition to β-delayed γ rays, SuN also detects neutrons and the high-energy electrons from the β decay. The neutron signal in SuN arises through inelastic scattering reactions, $^{127}\mathrm{I}(n,n'\gamma)^{127}\mathrm{I}$ and $^{23}\mathrm{Na}(n,n'\gamma)^{23}\mathrm{Na}$, or neutron capture on ^{127}I ($Q = 6.826$ MeV) [65]. The neutron signatures in SuN are demonstrated with a GEANT4 simulation of SuN using mono-energetic neutrons at 1 MeV emitted isotropically from the centre of the detector (Fig. 3.18). The presence of 58 keV γ rays from inelastic scattering of neutrons on ^{127}I is seen, as is the sum peak around the neutron capture threshold of ^{127}I at 7.8 MeV (with the capture Q-value summed with the energy deposited by inelastic scattering) [66].

Though SuN in principle detects neutrons, the efficiency is not high, and the neutron capture peak is overwhelmed by decay cascades from states in ^{61}Cr at that energy. As part of this thesis, some work was done comparing GEANT4 simulations of (p, n) events to SuN data measuring ^{92}Zr(p, n) and ^{64}Ni(p, n) from experiments carried out at Notre Dame. However, on the whole, the response of SuN to neutrons has not been well-benchmarked, unlike its response to γ rays. As such, the neutron data from NERO are needed to determine the β-delayed neutron branch of the decay of ^{61}V.

3.4.2.2 Electrons

To simulate the SuN detector response to β electrons, it is important to include the beampipe and the miniDSSD because the additional material shifts the electron spectrum seen in SuN to lower energies. Low-energy electrons up to ∼400 keV will be stopped in the miniDSSD. Electrons up to ∼1 MeV are stopped in the SuN beam-pipe. Higher-energy electrons will enter SuN and be detected, and can be summed together with the β-delayed γ rays, complicating the extraction of γ rays cascade strengths. Thus, in addition to generating γ rays, the SuN GEANT4 simulation included neutron and electron emission. The neutrino is ignored as the likelihood of interaction is effectively nil.

The simulated electron spectrum in SuN following an interaction with the DSSD and the SuN beam-pipe is shown in Fig. 3.19. As the average electron energy increases (with increasing β decay Q value), less energy is deposited in the DSSD and the beampipe. Consequently, the fraction of total electron energy deposited in the SuN detector will increase.

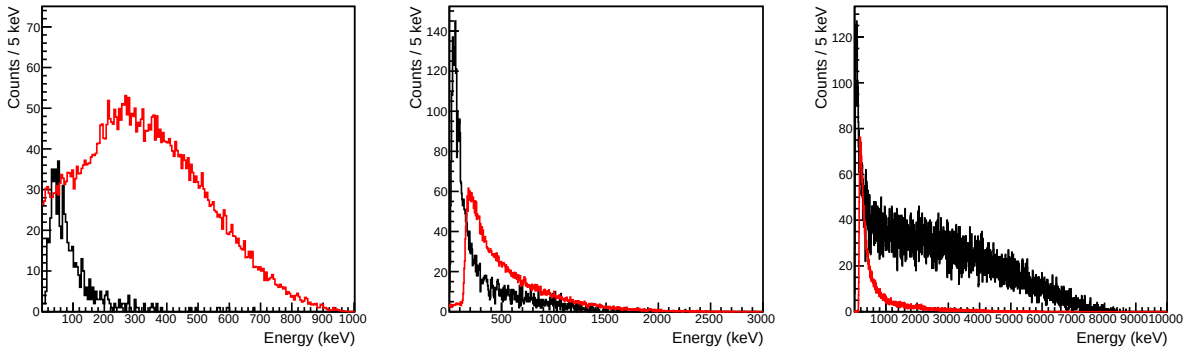

Figure 3.19: Simulated total absorption spectrum (black) and energy deposited in the DSSD (red) for allowed β decay of a species with a Q value of 1 MeV (left), 3 MeV (centre), and 10 MeV (right).

3.4.3 GEANT4 simulation of β decay events in SuN

Each β decay event in GEANT4 begins with a decay that occurs in the miniDSSD at the target position of SuN. The γ ray cascade associated with this decay event is read in from an input file and the total energy of the cascade is subtracted from the β-decay Q-value. The remainder of the energy is shared between the electron and the neutrino. The electron energy is randomly generated, sampling the β-decay distribution for allowed transitions, and the electron is emitted from the centre of SuN, following an isotropic angular distribution. For templates for βn decays, the neutron is emitted isotropically, and its energy, E_n, is given by Eqn. 3.4,

$$E_n = E_f - E_i - S_n, \tag{3.4}$$

where E_f is the energy of the state in ^{60}Cr populated by the neutron emission, E_i is the energy of the state in ^{61}Cr which is first populated by the β decay of ^{61}V, and S_n is the neutron separation energy of ^{61}Cr.

3.5 Extracting β-feeding intensities from SuN γ ray spectra

The total β decay radiation spectrum from SuN was considered to be the sum of the β decay radiation spectra for the decays to single states. Instead of attempting to simulate the full β decay spectrum in SuN, templates of the β decay specta for β decays to individual states in ^{61}Cr and βn decays to states in ^{60}Cr are generated, and the total spectrum is then a linear combination of the templates. The β decay transition strengths, including the βn feeding, are the normalised co-efficients from the fit to the data. In the following sections, a 'template' refers to the simulated γ ray spectrum of β decays to a given state, and a 'sub-template' refers to the simulated γ ray spectrum of a specific γ decay cascade following β decays to a given state (Fig. 3.22).

3.5.1 Generating templates of the decay of known states

Several levels in ^{61}Cr populated by the β decay of ^{61}V have been identified in a previous study using the high purity Germanium array SeGA [36] (Fig. 3.20). Together with states in ^{60}Cr populated following β-delayed neutron emission, and states in ^{61}Mn populated by the decay of ^{61}Cr, these are marked out in Fig. 3.21. No new states in ^{61}Cr were definitively identified in this study, as the limited resolution of SuN makes it challenging to identify individual states. Additionally, because of the contribution of the β decay electrons to the total absorption spectrum, the background was too high to effectively identify peaks.

Cascade branchings from known levels were found by recursively fitting the contribution of cascades from lower-lying states. This is described using the 224 keV level as an example. First, three GEANT4 sub-templates were generated, representing the decays through the

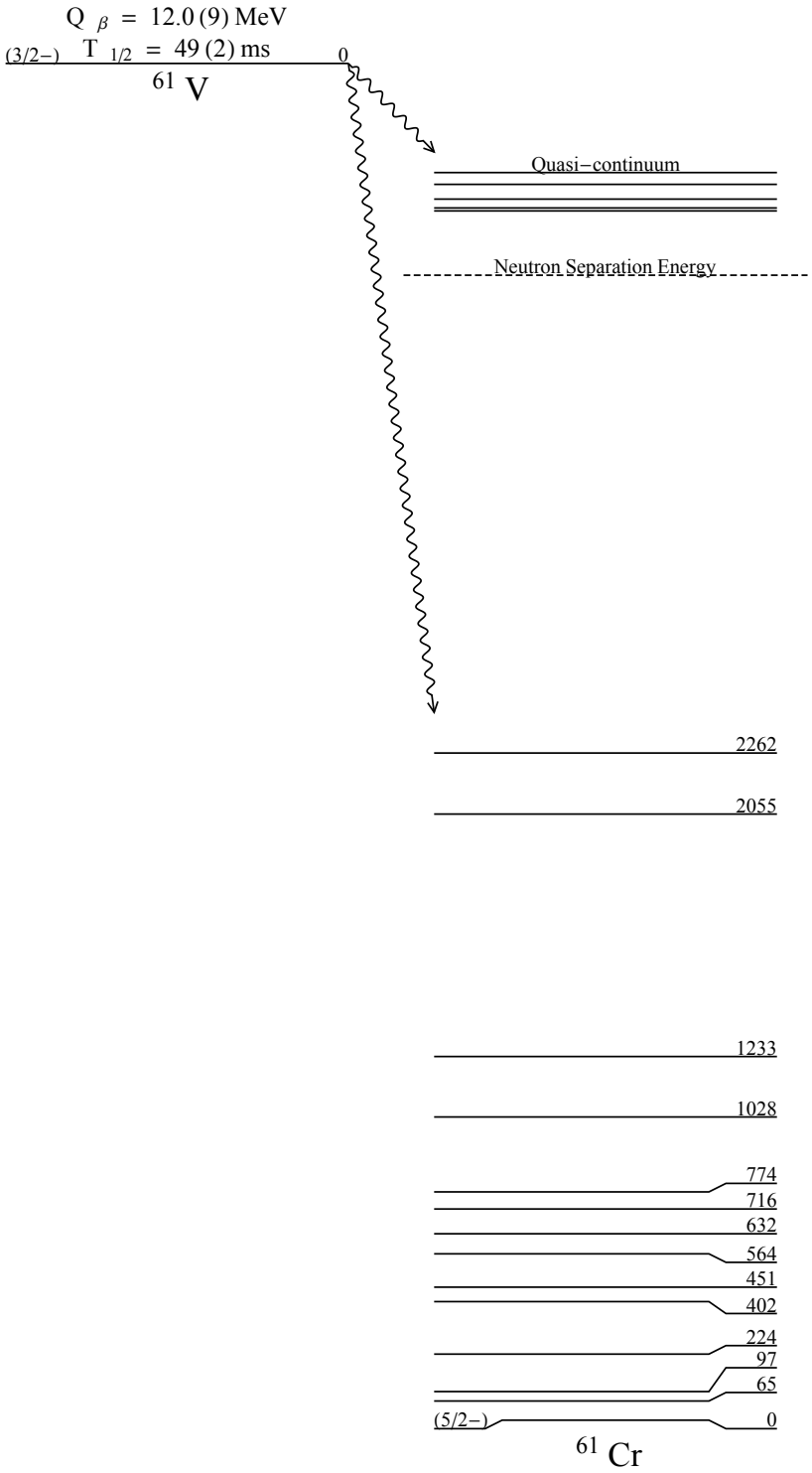

Figure 3.20: Level scheme showing the known excitation levels in ^{61}Cr populated by β decay.

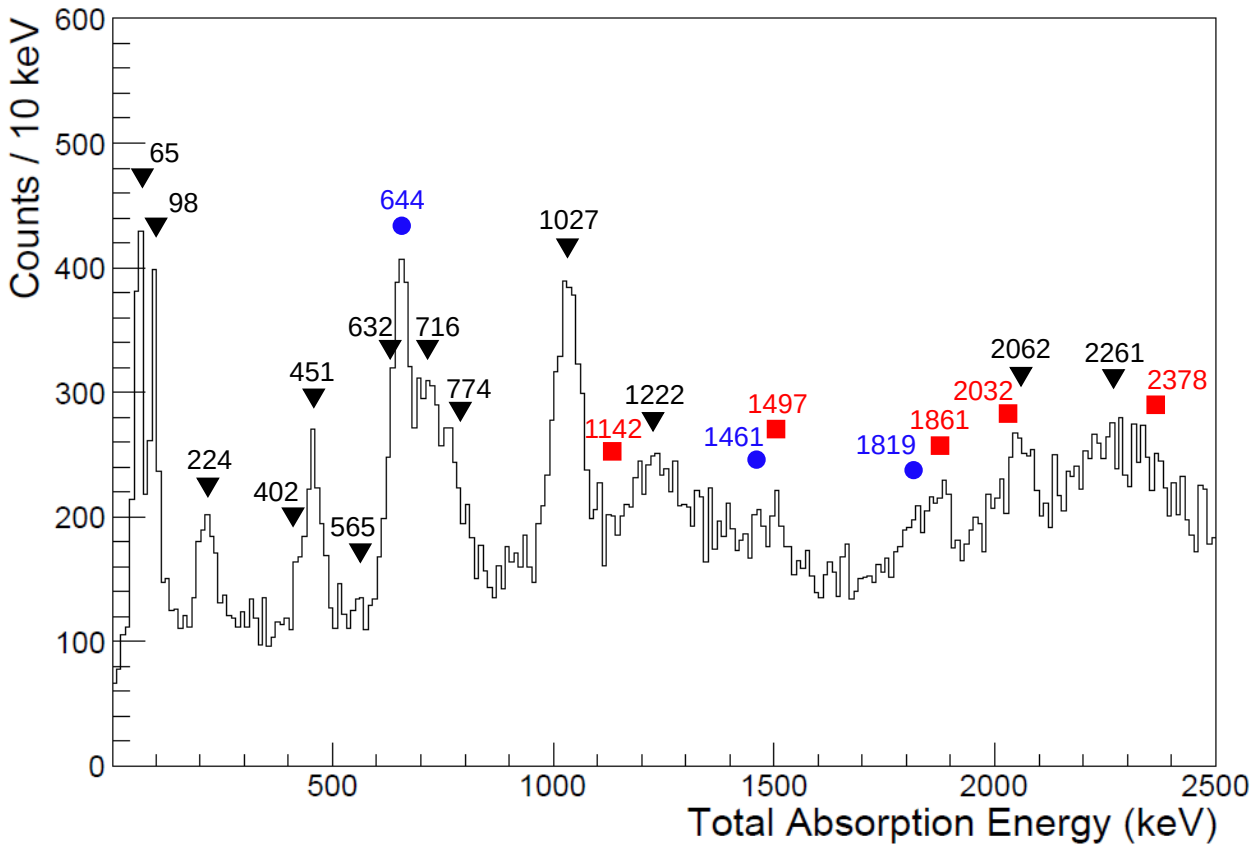

Figure 3.21: Total Absorption spectrum of γ rays correlated with β decay events from implants in the ^{61}V PID gate. Black triangles, blue circles, and red squares denote levels in ^{61}Cr, ^{60}Cr, and ^{61}Mn respectively.

first excited state to the ground state, second excited state and the direct to ground state transitions respectively (Fig. 3.22). Strictly speaking, there is a possibility that the second excited state might populate the first excited state by γ decay, but this transition is not expected to play a role because of its low energy of 33 keV. Once the sub-templates are generated, a χ^2 minimisation was performed using MINUIT to determine the contribution of each sub-template to the sum of segments spectrum from data when gated on the 224 keV sum peak (Fig. 3.23).

Once the decay branchings of the 224 keV state have been determined, it can be used to generate a template of the decay of the 224 keV state and used to fit the decay of the

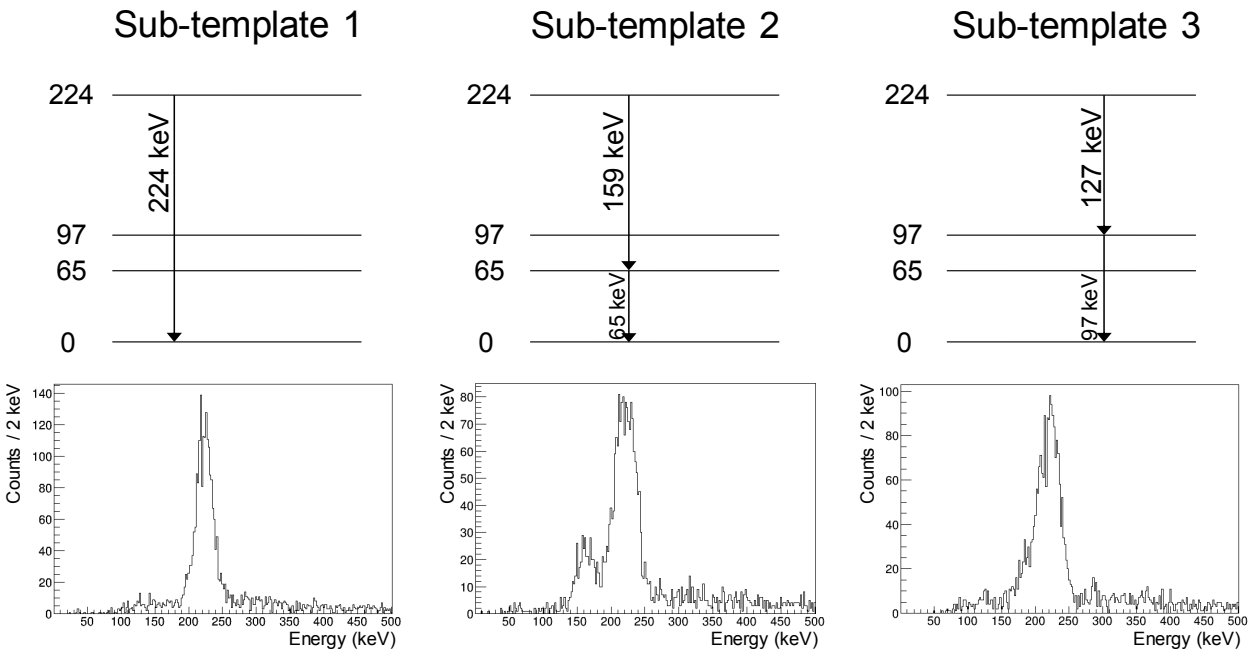

Figure 3.22: The sub-templates representing the three different γ decay cascades from the 224 keV state.

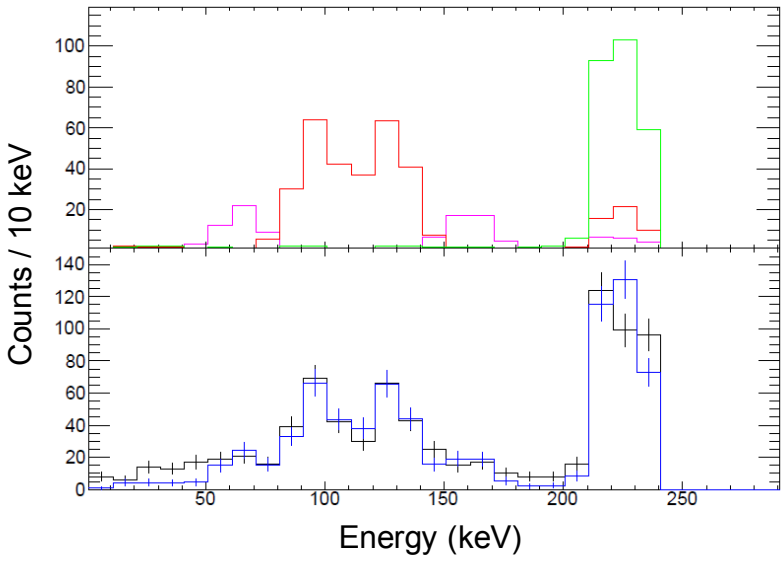

Figure 3.23: Top: Contributions of individual templates of the decay to the ground state (green), through the first excited state (magenta), and through the second excited state (red). Bottom: Comparison between the best fit of the templates (blue) and the data (black).

next excited state at 402 keV through the 224 keV state. A comprehensive template for an known entry state that implements all possible decay cascades, using the prior determined branchings, is then generated to represent the spectrum for the γ decay when that state is populated by β decay. This procedure is done for all 12 excited states identified in [36].

3.5.2 Generating templates of the decay of unknown states with DICEBOX

β decay of ^{61}V can populate states in ^{61}Cr up to the decay Q-value. In this case, the level scheme of ^{61}Cr is known only up to 2.26 MeV, whereas the Q-value is 11.97(90) MeV. While the decay strength to each of these unknown states could be small, the total decay strength to states above 2.26 MeV could be substantial and must be considered. In lieu of complete knowledge of the excitation scheme of ^{61}V, levels above 2.26 MeV are treated as a quasi-continuum, with pseudolevels inserted every 50 keV up to 3.2 MeV, every 100 keV up to 3.95 MeV and every 200 keV up to the Q-value. Because of the coarse resolution of SuN, it is impossible to separate total absorption peaks to within 6%, and so each pseudolevel represents all states within the band given by the difference in energy between pseudolevels.

The decay scheme of each pseudolevel is simulated using the DICEBOX statistical code. A detailed explanation of the DICEBOX code can be found in [67], but the main procedure of the code is as follows: The DICEBOX code adopts a dichotomous approach to generating decay cascades. For levels below a energy cut-off termed $E_{\mathrm{crit}} = 2.262$ MeV, the decay scheme is determined by known excitation energies, spins and parities, and decay branchings (taken as input to the code, in this case, the results from the the procedure in section 3.5.1). For levels above E_{crit}, the levels (and their spins and parities) are distributed according

to an input level density prescription [53]. The first step of DICEBOX discretises the level density function, generating a set of states (here-after referred to as a nuclear realisation) between an input energy E_e, termed the entrance energy, and $E_{\rm crit}$. Transitions between levels are governed by input photon strength functions (PSFs), with the assumption that the only radiation multipolarities that present are electric dipole (E1), magnetic dipole (M1), and electric quadupole (E2) radiation. The total decay scheme for decay for a given entry state at energy E_e, with spin and parity J^π, is then generated by a Monte Carlo simulation using these parameters. For each nuclear realisation, a sufficiently large number of Monte Carlo steps have to be used to ensure that the set of generated cascades is statistically representative of the input distributions.

For each Monte Carlo step, the state at E_e is populated, and is allowed to decay to a secondary state of lower energy. The cascade continues following the PSFs, if the intermediate level is still above $E_{\rm crit}$, or the input branching ratios, if the intermediate level is below $E_{\rm crit}$. This procedure is repeated for all pseudolevels, and spin/parity combinations for allowed transitions from the ^{61}V ground state ($J^\pi = 3/2^-$), and the decay scheme for each pseudo-level is given by a simple average of the three spin/parity combinations for an allowed transition ($J^\pi = 1/2^-$, $3/2^-$, and $5/2^-$).

Once the templates were generated, a least squares fit was performed to determine the contribution of each template to the total absorption spectrum. This was done with MINUIT [68] in the ROOT C++-based data analysis toolkit [69,70]. The resulting co-efficients of the fit, when properly normalised, will give the β feeding intensities. The results of this fit are discussed in the following chapter.

Chapter 4

Results

4.1 β Decay of ^{61}V

4.1.1 Half-life

The correlated β decay events using a correlation window of 500 ms and gated on ^{61}V in the PID are shown in the decay curve in Fig 4.1. The total fit includes contributions from: (1) the decay of ^{61}V; (2) the decay of the daughter ^{61}Cr ($t_{1/2}$ = 237±11 ms); (3) the decay of the neutron daughter ^{60}Cr ($t_{1/2}$ = 490±10 ms); (4) the decay of the grand-daughter ^{61}Mn ($t_{1/2}$ = 709±8 ms); (5) the decay of the neutron grand-daughter ^{60}Mn ($t_{1/2}$ = 280±20 ms); and (6) a flat background.

The contributions of the decaying nuclei were modelled using the Bateman equations (Section 2.2), using the experimentally-known half-lives for the set of daughters and grand-daughters, as well as the P_{n} obtained from the NERO data (disucssed later). The magnitude of the background is also not a free parameter, as it is determined from reverse-time correlation (Section 3.3.2) over the same correlaton interval of 500 ms.

The half-lives from these fits are 46 ± 3 ms and 44 ± 3 ms for the SuN miniDSSD and BCS DSSD data respectively. The error in the extracted half-lives have both systematic and statistical components. The systematic component arises from the uncertainties in the half-lives of the nuclei in the decay chain (listed above) and the uncertainty in the P_{n} value, and

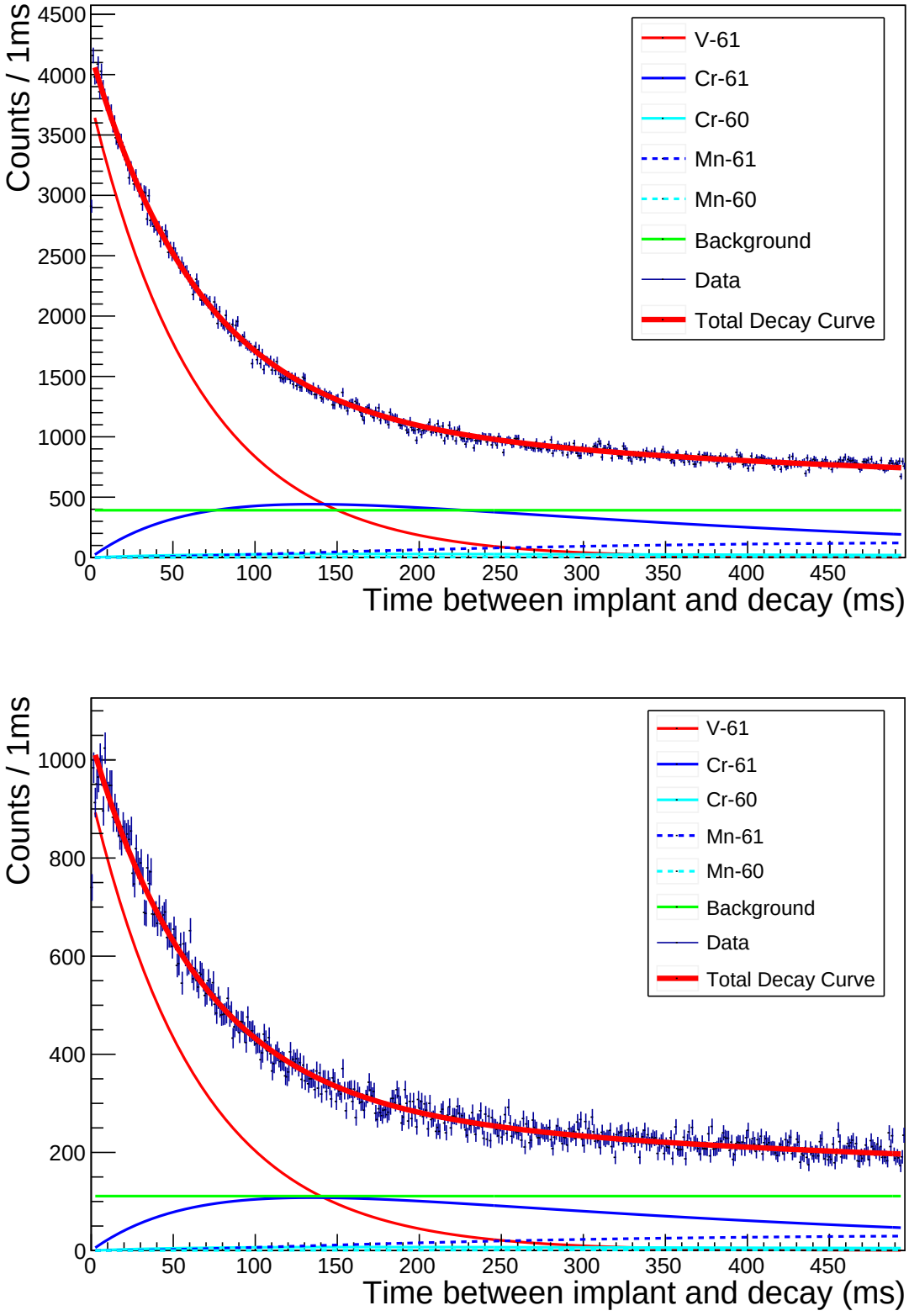

Figure 4.1: Top: Decay curve fit for the SuN miniDSSD. Bottom: Decay curve fit for the BCS DSSD.

was evaluated by a Monte Carlo calculation. For each Monte Carlo instance, the half-lives of the decay chain nuclei were varied within their uncertainties and the decay curve was fit. The systematic error was then extract from the distribution of the half-life of ^{61}V from the fits. The statistical error was determined from the error in the fit co-efficients, derived from the statistical error of each bin.

For the SuN portion of the experiment, γ rays were detected in coincidence with β decay signals. By gating on a γ ray associated with the decay of ^{61}V to an excited state in ^{61}Cr, the half-life of ^{61}V can be determined more accurately than the total fits. In this case, the gated decay curve will have only an exponential contribution from the decay of ^{61}V and a flat background, eliminating all contributions from nuclei in the decay chain. This eliminates all systematic errors associated with the error bars of the daughter/grand-daughter half-lives. The β decay curve gated on total absorption γ cascades from the decay of ^{61}V is shown in Fig. 4.2. The extracted half-life from this fit is 49(2) ms, in agreement with the previously measured values (Tab. 4.1).

For the NERO portion of the experiment, neutrons were detected in coincidence with β decay signals. Similar to gating on a γ ray, a gate on β decay events that produce a neutron will reduce the complexity of the fit. The predicted β-delayed neutron emission branches of the nuclei in the ^{61}V decay chain are small or zero ($P_{\mathrm{n}}(^{61}\mathrm{Cr}) = 0.6\%$, $P_{\mathrm{n}}(^{60}\mathrm{Cr}) = 0.00\%$, $P_{\mathrm{n}}(^{61}\mathrm{Mn}) = 0.01\%$, $P_{\mathrm{n}}(^{60}\mathrm{Mn}) = 0.00\%$ [71, 72]), such that the neutron-gated decay curve should only contain contributions from a flat background, an exponential background, and the parent decay. The flat background arises from background neutrons arriving close in time to falsely correlated decay events, and the exponential background arises from β-delayed neutrons arriving in coincidence with falsely correlated decay events or from background neutrons arriving in coincidence with true β decay events. The β decay curve gated on

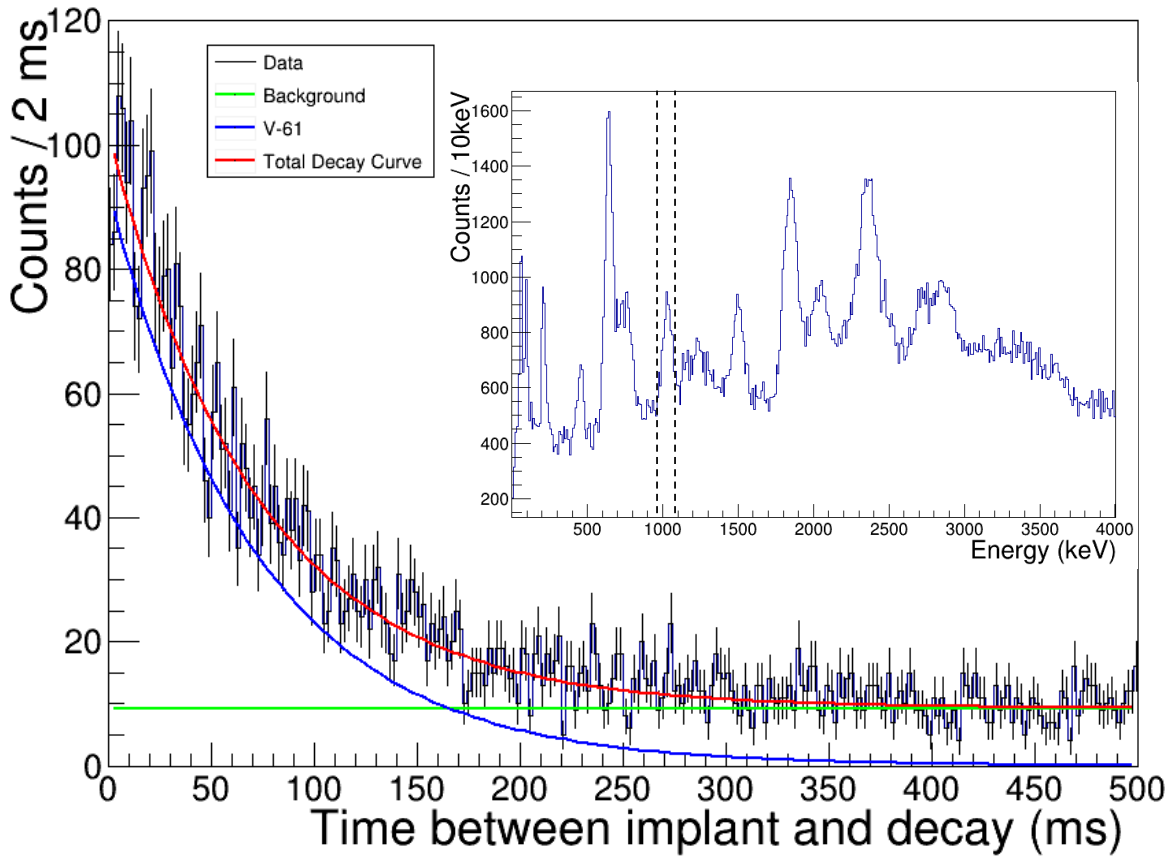

Figure 4.2: Decay curve from the SuN miniDSSD when gated on the 1028 keV cascade (inset) from the corresponding state in ^{61}Cr

coincident neutrons is shown in Fig. 4.3. The extracted half-life from this fit is 48(1) ms.

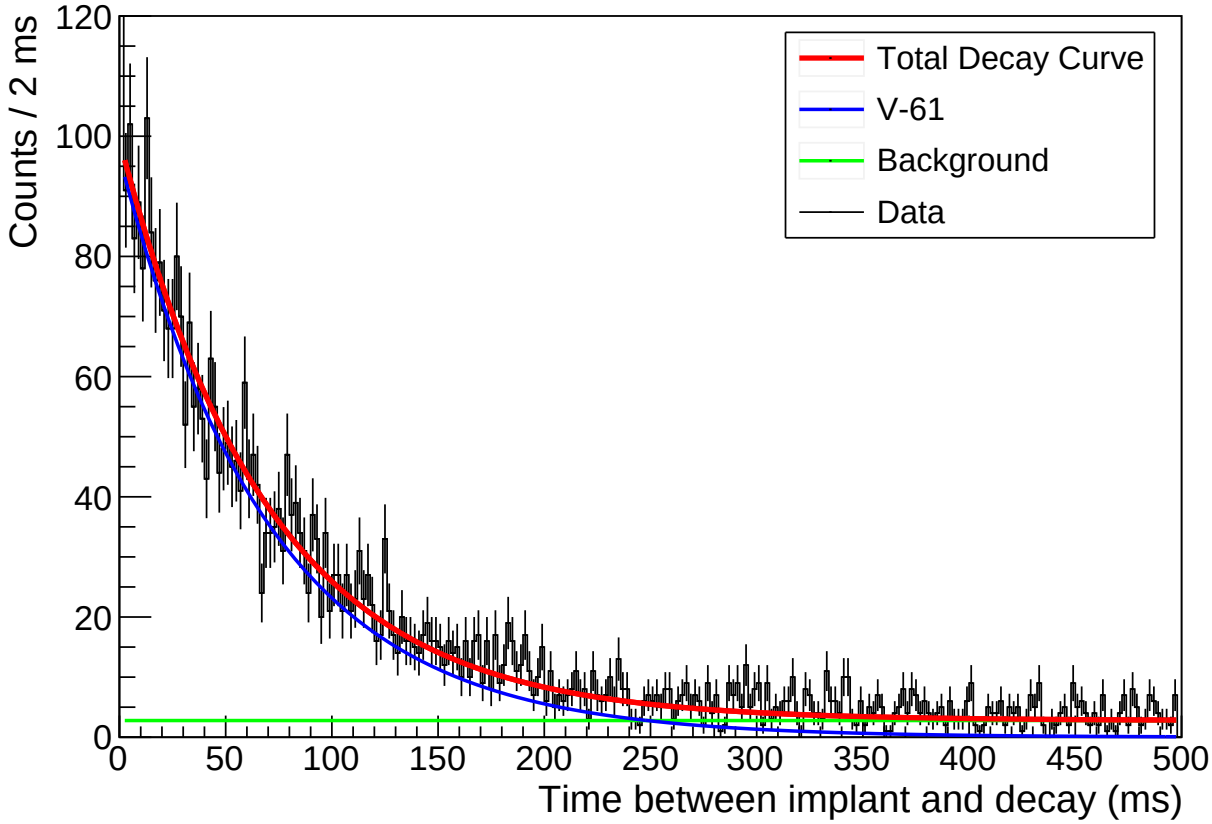

Figure 4.3: Decay curve from the BCS DSSD when gated on coincident neutrons.

Reference	Half-life (ms)
Sorlin *et al.* 1999 [73]	43 ± 7
Sorlin *et al.* 2003 [74]	47.0 ± 1.2
Gaudefroy *et al.* 2005 [75]	47 ± 1
Daugas *et al.* 2011 [76], Matea 2002 [77]	52.6 ± 4.2
Suchyta *et al.* 2014 [36]	49 ± 1
This work (BCS DSSD)	46 ± 3
This work (SuN miniDSSD)	47 ± 3
This work (BCS DSSD gated on neutrons)	48 ± 1
This work (SuN miniDSSD gated on γ ray)	49 ± 2

Table 4.1: Comparison of measured values in this work with previously measured values of the half-life of ^{61}V.

4.1.2 β-delayed neutron branch

The β-delayed neutron branch of ^{61}V was determined using

$$P_{\mathrm{n}} = \frac{N_{\beta n} - B_n}{\epsilon_n N_\beta} \tag{4.1}$$

where $N_{\beta n}$ is the number of neutrons detected in coincidence with β decays, B_n is the number of background β-neutron coincidences, N_β is the total number of correlated β decays, and ϵ_n is the neutron detection efficiency of NERO. Here, the assumption is made that the β correlation efficiency is the same for β decays to states above and below the neutron emission threshold, supported by the analysis in section 3.3.1.

The energies of β-delayed neutrons can range from zero to Q_β -S_n ($\sim$ 8 MeV in this case), where S_n is the neutron separation energy of ^{61}Cr (3880 $\pm$ 220 keV [65]). As discussed in [57], the expected neutron energy distribution favours low energy neutrons below 1 MeV, and it is likely that most of the neutrons are below 500 keV where the efficiency of NERO is fairly constant. This is supported by QRPA calculations which predict that the strongest transitions to states above the neutron separation threshold in ^{61}Cr lie below 5 MeV that emit neutrons of up to 1.1 MeV. Therefore, similar to [57], a flat efficiency of $37 \pm 5\%$ was assumed for NERO, and a P_{n} value of 14.5 $\pm$ 2.0 % was determined. The dominant source of error in the P_{n} value is the systematic error associated with the efficiency of NERO and the lack of knowledge of the neutron energy distribution.

4.1.3 β feeding intensities

The β feeding intensity to a state in ^{61}Cr, or the number of times that a state in ^{61}Cr is populated by 100 β decays of ^{61}V, was determined from the strength of the total absorption

peak at the energy of the state as measured by SuN. To minimise the contribution of unwanted γ rays from background and other decays (e.g. daughter and grand-daughter decays) to the γ ray spectra, three things were done (illustrated in the first three rows of Fig. 4.4 respectively). Firstly, the γ ray spectra from the backwards time correlation were subtracted from the spectra from the forward time correlation. This eliminates the contribution from randomly correlated background (the green lines in panels (a) and (i) in Fig. 4.4). Secondly, the spectra that were fit were gated to include only events where the time difference between the implant and decay was less than 50 ms ($\sim$ one half-life of ^{61}V) indicated by the solid line in panel (b) of Fig. 4.4. This limits the contribution (relative to the number of ^{61}V decays) of decays of the ^{61}Cr daughter nucleus to 6.97%, producing the magenta spectrum in panel (ii) in Fig. 4.4; and lastly, the spectra from a later time (60-80.98 ms) in the correlation time plot were subtracted to eliminate the contribution of the decays of ^{61}Cr and ^{60}Cr completely (panels (c) and the grey line (iii) in Fig. 4.4). The grand-daughters contributed only at the 0.01% level, and were ignored. The end result is the red spectrum shown in panel (iv) of Fig. 4.4.

The best fit (reduced $\chi^2 = 1.3$) of the GEANT4-generated templates to the background subtracted total absorption spectrum is shown in Fig. 4.5, along with the corresponding sum of segments spectrum. Within the resolution of the SuN detector, the observed peaks in the total absorption spectrum can be matched to the level scheme in [36] (see Fig. 3.21). The single exception is the 565 keV state that is not detectable above background in the total absorption spectrum, but was reported to have a 1.5% branching by [36].

To assess the error in the β-feeding intensities extracted from the fit, a Monte Carlo was performed where all the fit co-efficients were simultaneously varied using a lognormal distribution. A lognormal distribution was chosen to provide fine-grained sampling of the

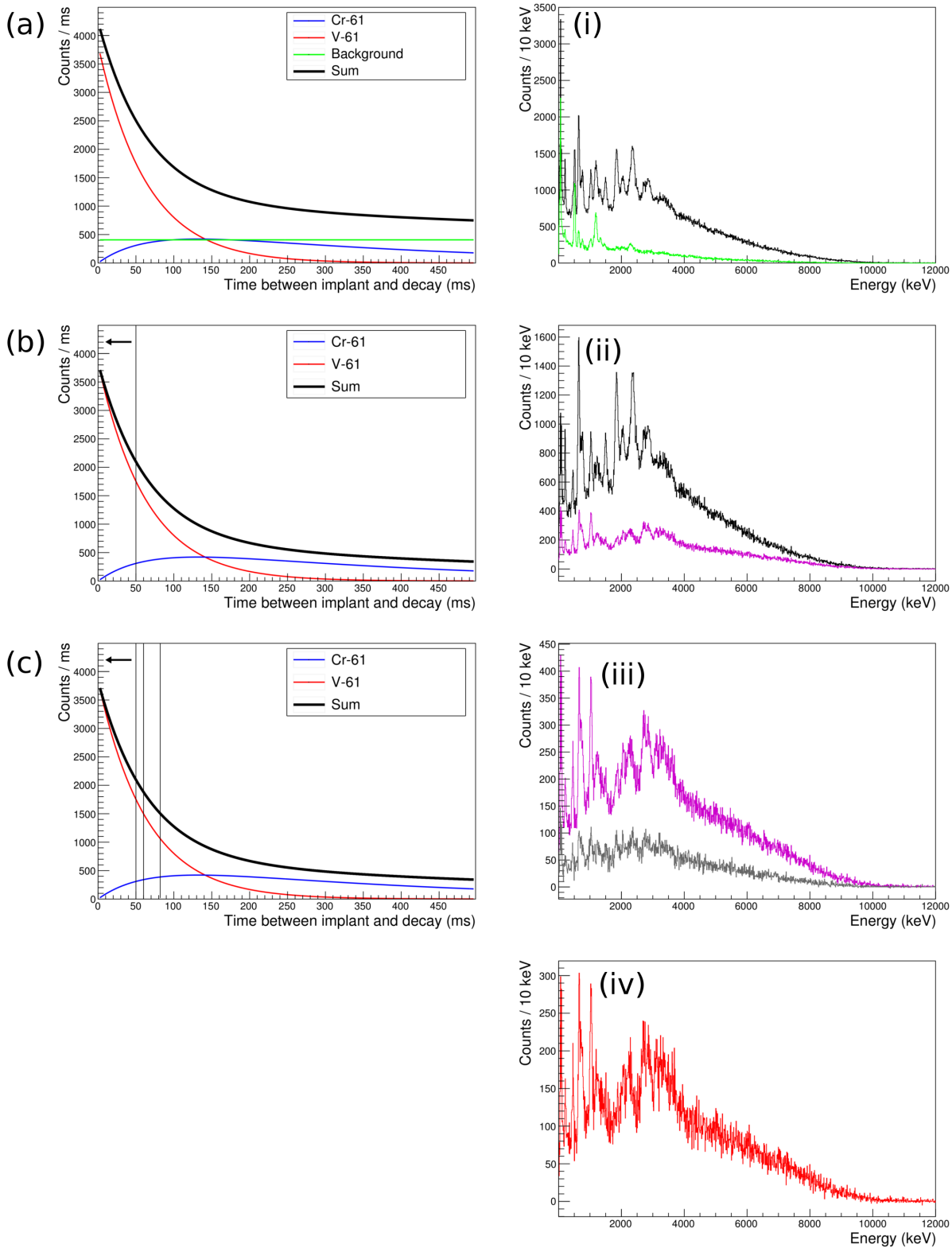

Figure 4.4: Panels (a)-(c) show the components of the decay curve still remaining in the corresponding TAS spectra shown in panels (i)-(iii). Panel (iv) shows the background-subtracted total absorption spectrum used for fitting.

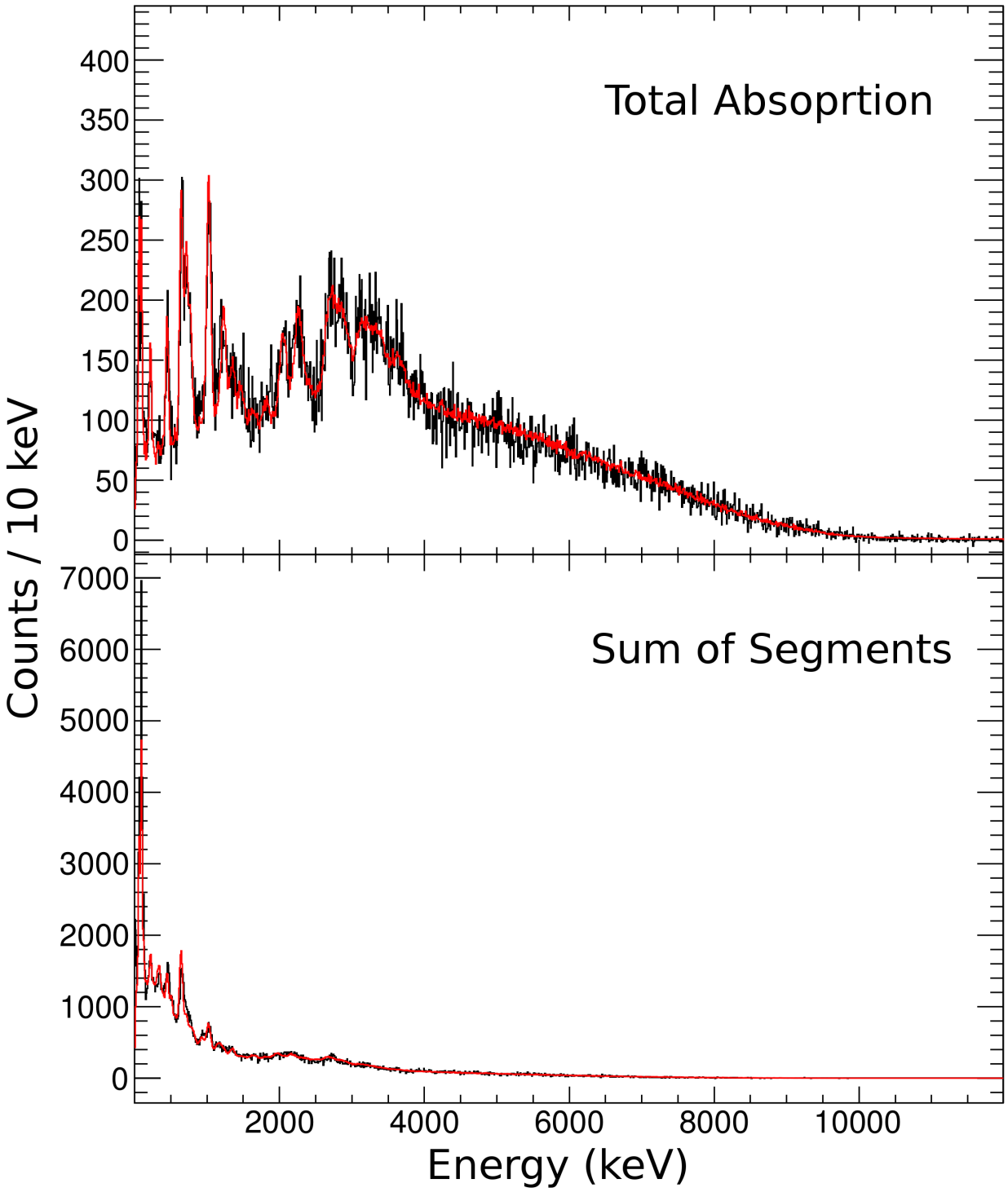

Figure 4.5: Data (black) and best fit from GEANT4 simulated templates (red) for the total absorption spectrum (top) and the sum of segments spectrum (bottom).

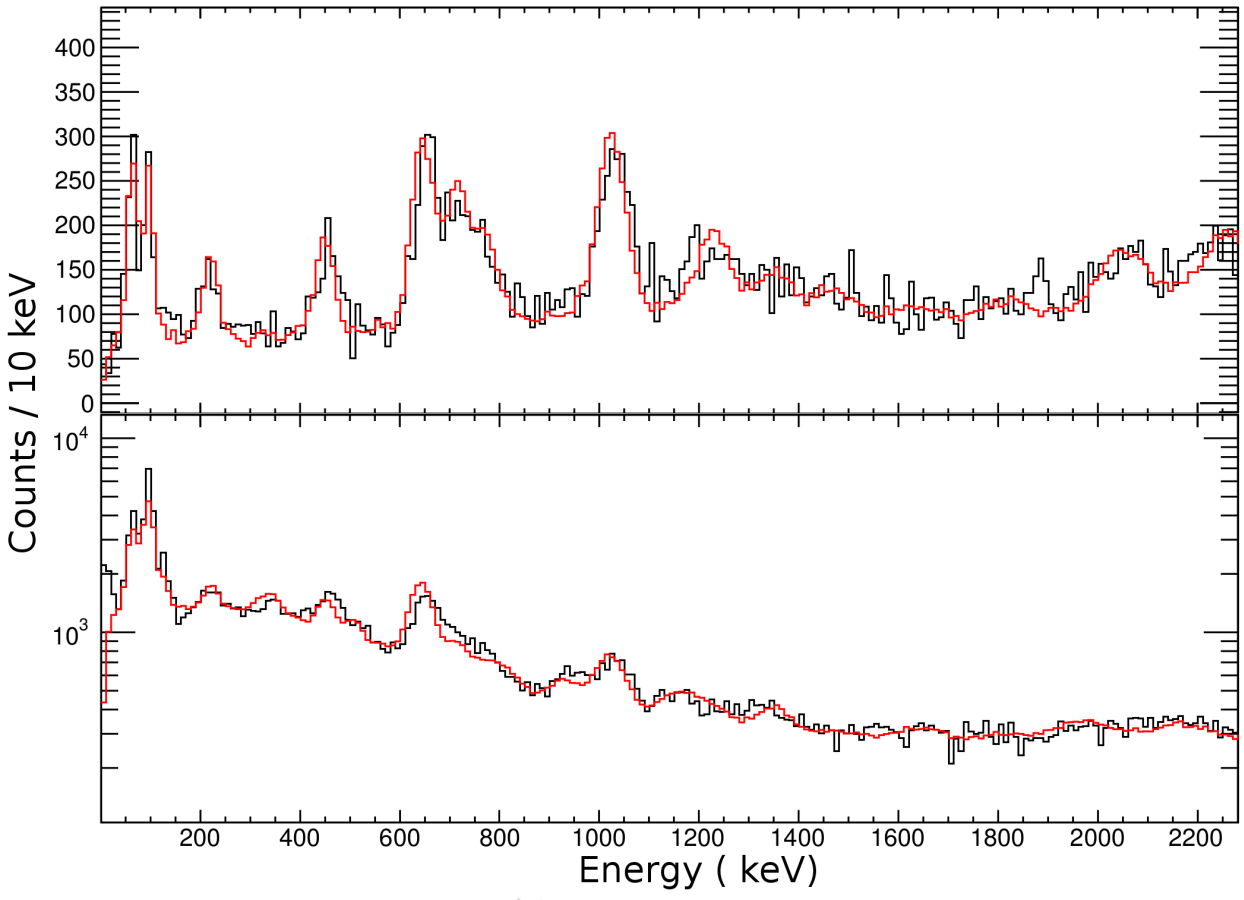

Figure 4.6: Data (black) and best fit from GEANT4 simulated templates (red) for the total absorption spectrum (top) and the sum of segments spectrum (bottom) up to $E_{\text{crit}} = 2270$ keV.

reasonable values for the fit co-efficients. The width of the distribution was set so that the reduced χ^2 boundary of the fit was located definitively. A uniform distribution varying each co-efficient from 0 to 10^4 was also used to demonstrate that the location of the reduced χ^2=2 boundary is independent of the shape or width of the input distribution used in the Monte Carlo.

The NERO P_n result of 14.5 (2.0) % was also used to narrow the distributions of the extracted β feeding intensities. A 1-σ cut of 12.5 % $\leq \sum$(I$_\beta$(^{60}Cr g.s.) + I$_\beta$(^{60}Cr 644 keV) + I$_\beta$(^{60}Cr 1460 keV) + I$_\beta$(^{60}Cr 1819 keV))$\leq$ 16.5 % was imposed on the results of the Monte Carlo. The results from the best fit and Monte Carlo, along with a comparison to the inferred β feedings from [36] are given in Tab. 4.2.

The results from this work demonstrate the Pandemonium effect in the results from the previous β decay study. The β feedings to low-lying excited states in ^{61}Cr obtained using the TAGS method are systematically lower than those from [36], where HPGe detectors were used. It is only at higher energies, above 1 MeV, where the feedings from this study exceed those from the previous study.

There exist several degeneracies between certain templates which lead to particularly large uncertainties in feeding for the states represented by those templates. Firstly, between the templates of the decays to ground states of ^{61}Cr and ^{60}Cr, as neither of them have distinct γ rays. Even though the Q-values of each of the transitions is different ($Q_{\beta-}$(^{61}V) = 11969 (900) keV and $Q_{\beta-n}$(^{61}V) = 8092 (915) keV) [65], and the electron spectrum measured by SuN should be different, it is still expected that the templates are to some extent degenerate as the shapes are fairly similar. Another degeneracy is that of the 632 keV state in ^{61}Cr and the 644 keV first excited state in ^{60}Cr. To assess the degeneracy within these two sets of templates, a Monte Carlo simulation was performed where the fit co-

State (keV)	This work (%)	Suchyta *et al.* [29, 36] (%)
0	$7.4^{+13.8}_{-5.8}$	<40
65	$2.6^{+3.7}_{-1.8}$	6.0 (1.2)
97	$2.1^{+2.6}_{-1.6}$	10 (6)
224	$2.0^{+2.8}_{-1.5}$	7.1 (1.1)
402	$0.3^{+0.3}_{-0.26}$	1.7 (0.5)
451	$3.0^{+3.1}_{-2.2}$	5.7 (0.7)
564	$0.3^{+0.9}_{-0.2}$	1.5 (0.4)
632	$0.3^{+0.3}_{-0.3}$	1.7 (0.7)
716	$4.3^{+4.0}_{-3.2}$	6.1 (0.8)
774	$3.0^{+3.7}_{-2.4}$	3.2 (0.7)
1028	$8.8^{+5.3}_{-4.2}$	8.4 (0.8)
1233	$4.5^{+4.0}_{-3.1}$	1.4 (0.3)
2055	$4.1^{+4.9}_{-3.4}$	2.2 (0.7)
2262	$5.6^{+5.6}_{-4.2}$	2.5 (0.8)
Quasi-continuum	$31.9^{+27.8}_{-17.2}$	-

Table 4.2: List of β feeding intensities to the identified states in the ^{61}Cr excitation scheme from [36], and the corresponding apparent β feedings deduced by [29] from [36].

efficients for each set templates were varied (separately) while all other co-efficients were held constant at the values obtained by the χ^2 minimisation performed by MINUIT.

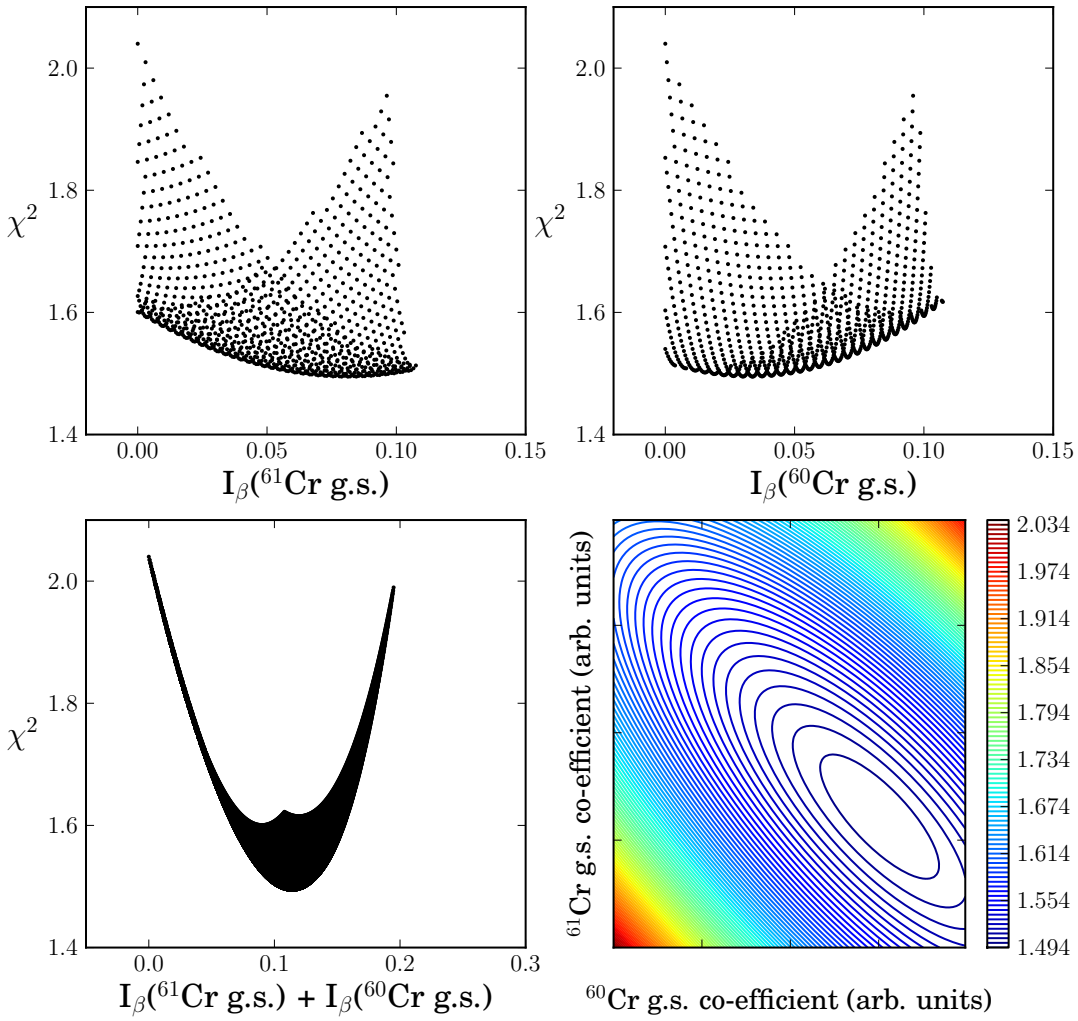

Figure 4.7: Beginning bottom left, clockwise: Reduced χ^2 as a function of (i) the sum of the two ground state transition intensities; (ii) $I_\beta(^{61}$Cr ground state); (iii) $I_\beta(^{60}$Cr ground state); and (iv) contour plot demonstrating the correlation between the two parameters. The increasing warmth of the colour denotes increasing χ^2.

The Monte Carlo results demonstrate that the goodness-of-fit is most strongly dependent on variations of the sum of the parameters, and is less dependent on variations of the indi-

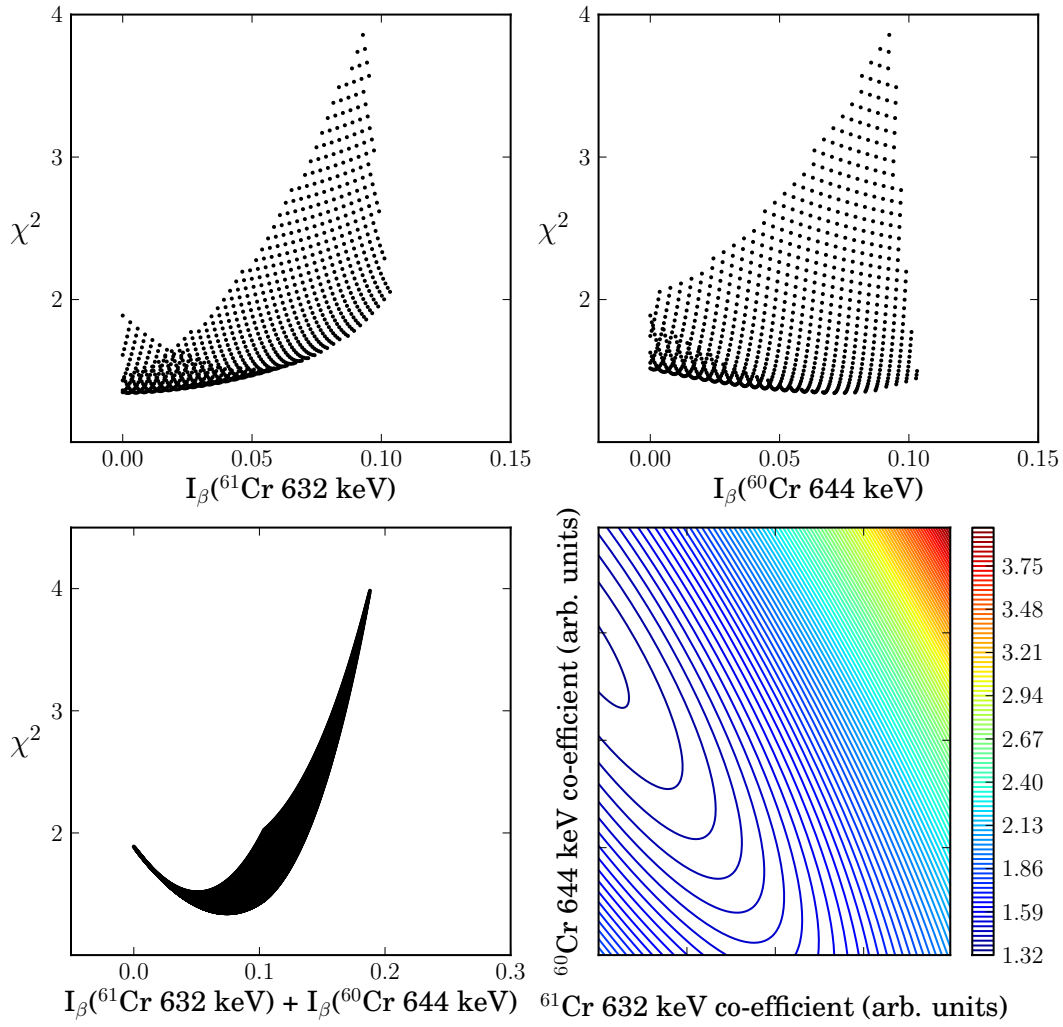

Figure 4.8: Beginning bottom left, clockwise: Reduced χ^2 as a function of (i) the sum of the two transition intensities; (ii) $I_\beta(^{61}Cr\ 632\ keV)$; (iii) $I_\beta(^{60}Cr\ 644\ keV)$; and (iv) contour plot demonstrating the correlation between the two parameters. The increasing warmth of the colour denotes increasing χ^2.

vidual parameters themselves. The contour shape of the χ^2 as a function of two parameters is linked to the correlation between the two parameters. If there were no or only a weak correlation, the contour would be more circular, whereas the high ellipticity of the contours in Fig. 4.8 and 4.7 are indicative of a strong correlation between the two parameters.

4.1.4 ft-value and Urca strength

With the determined I_β of the transitions, the log ft values for the lowest transitions were calculated using a $Q_\beta = 11.969$ MeV. Tab. 4.3 summarises the log ft values for all known excited states as well as the intrinstic Urca luminosity L_{34} of the ground state and the 65 keV first excited state in ^{61}Cr. The value found experimentally for the ground state transition is higher than the value calculated by QRPA of 4.35.

State	log ft	L_{34}
Ground state	$5.5^{+0.8}_{-0.6}$	507
65 keV	$6.0^{+0.6}_{-0.6}$	34
97 keV	$6.1^{+0.7}_{-0.5}$	
224 keV	$6.1^{+0.7}_{-0.5}$	
402 keV	$6.9^{+1.0}_{-0.5}$	
451 keV	$5.8^{+0.8}_{-0.4}$	
564 keV	$6.8^{+0.7}_{-0.8}$	
632 keV	$6.5^{+\infty}_{-0.2}$	
716 keV	$5.6^{+0.8}_{-0.4}$	
774 keV	$5.8^{+0.8}_{-0.5}$	
1028 keV	$5.3^{+0.4}_{-0.4}$	
1233 keV	$5.5^{+0.7}_{-0.4}$	
2055 keV	$5.4^{+0.9}_{-0.5}$	
2262 keV	$5.0^{+1.0}_{-0.3}$	

Table 4.3: Table of log ft values for the β decay from ^{61}V to the known states in ^{61}Cr. The L_{34} values are only given for the ground state and the first excited state because β decay to the higher-lying excited states is highly suppressed and do not occur in Urca cycling.

Chapter 5

Astrophysics

We can now implement the new ground state to ground state log ft value for the decay of ^{61}V into a model for an accreted neutron star crust and determine the strength of crust Urca cooling from the ^{61}V-^{61}Cr pair.

The ground state to ground state log ft value of $5.5^{+0.8}_{-0.6}$ is higher than the QRPA prediction of 4.35. Prior to the measurement, the upper limit of 40% estimated by [36] would impose a lower limit on the log ft value of 4.6. To assess cooling strength of the ^{61}Cr-^{61}V pair, crust calculations similar to those in [22] were performed using the 1-σ range of the log ft value deduced from the experimental results.

The simulation, same as that used in [22], follows a fluid element in the crust as it travels deeper into the crust such that the electron chemical potential increases. A nucleosynthesis network was run with a starting composition of ^{61}Ni, and allowed to evolve for $\sim 10^{10}$s, corresponding to a column depth of $\sim 2\times10^{15}$ g/cm^2 and a mass density of $\sim 10^{10}$ g/cm^3, at a temperature of 0.5 GK. At this depth, neutrons become abundant enough to enable neutron capture and neutron-emitting reactions that transform nuclei from one mass chain to another, effectively eliminating the possibility of Urca cooling. Masses (and therefore Q-values) were taken from AME2016 [65], and the measured log ft values for the ground state to ground state β decays of ^{61}Fe, ^{61}Mn, ^{61}Cr, and ^{61}V were used. Electron capture transitions were assumed to have the same ft value as the β-decay transitions.

To evaluate the cooling impact of an isobaric chain, the time-integrated nuclear energy release per accreted nucleon $Q_{\rm nuc}$ (Eqn. 5.1) was calculated. The effects of compressibility and lattice energy due to changes in density are not included in $Q_{\rm nuc}$ to isolate the effect arising solely from nuclear reactions.

$$Q_{\rm nuc} = \sum (Y \Delta M + \mu_e dY_e - \epsilon_\nu) \tag{5.1}$$

The steps in the cooling profile (Fig. 5.1) indicate transitions between isobars, as indicated in the abundance plot in the upper panel of Fig 5.1. The abundance plot shows that the electron capture transition between nuclei does not occur at a sharp boundary, but instead occurs over a range of depth due to the finite temperature.

The experimental results presented in this work establish the ^{61}V-^{61}Cr pair as a major cooling mechanism in accreting neutron stars with crusts that contain $A = 61$ nuclei. Within our uncertainties, the cooling from ^{61}V-^{61}Cr is at least as strong as more shallower transitions, and likely much stronger. About 20% of the uncertainty in the log ft value arises from the large uncertainty in the mass of ^{61}V and therefore the uncertainty in the β decay Q-value. An improvement in the precision of the mass measurement would thus help further decrease the uncertainty in cooling strength.

The other experimentally-measured ground state to ground state β decay log ft values characterising the shallower Urca cooling pars in the mass 61 chain (^{61}Fe, ^{61}Mn, and ^{61}Cr) were performed either with high-purity germanium detectors or with small-angle NaI detectors and are likely subject to the Pandemonium effect. Hence, as suggested in the original works [26–28], these log ft values should be considered as lower limits. A true assessment of the cooling strength of this mass chain (as with another other) is predicated upon realistic

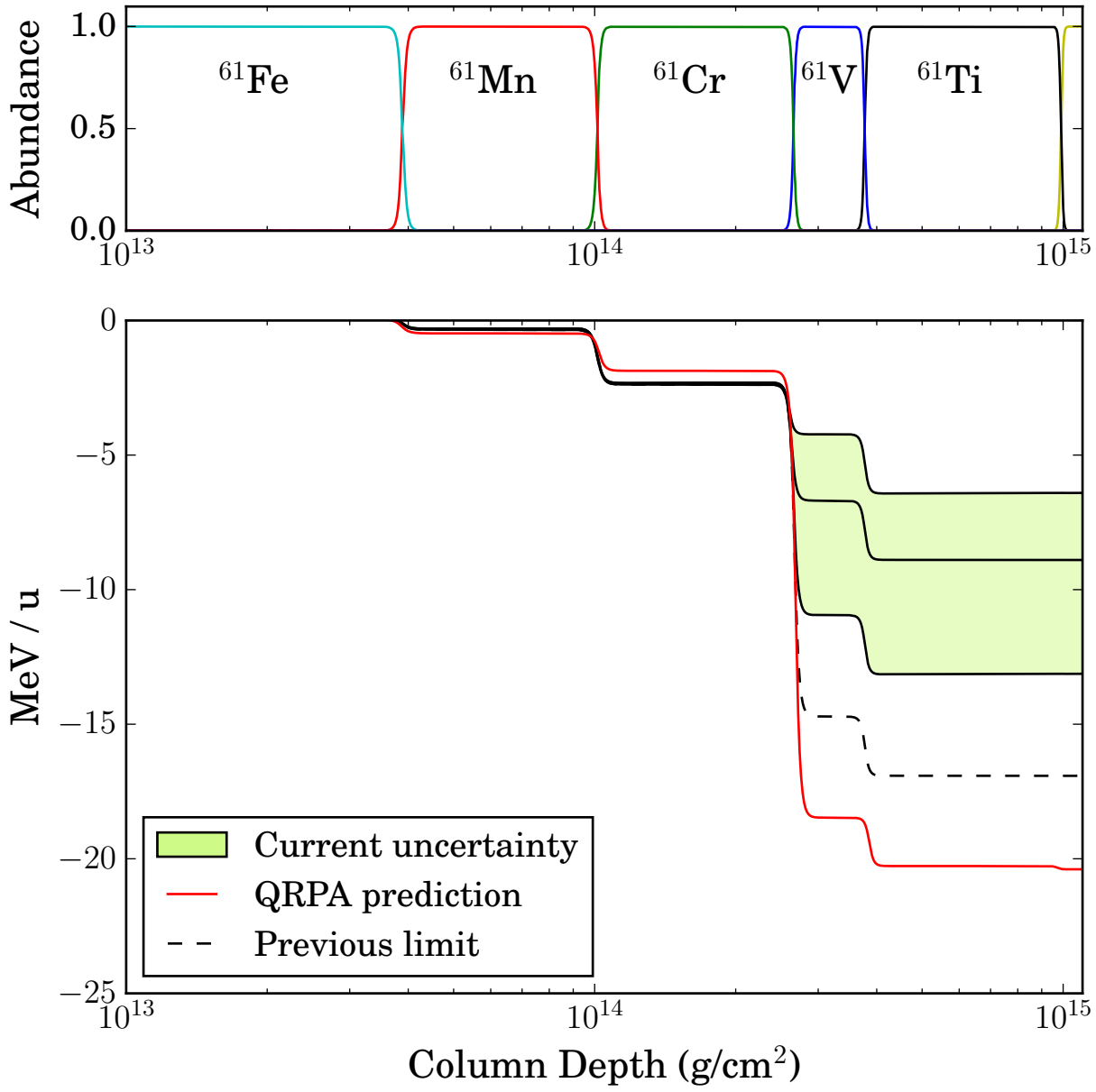

Figure 5.1: Top: Abundance plot of A = 61 nuclei as a function of column depth. Bottom: Cooling profile as a function of column depth. The grey band shows the uncertainty in the cooling profile prior to the experiment and the green band shows the uncertainty following the experiment. The uncertainty bands shown only reflect the uncertainty in the ^{61}V-^{61}Cr transitions.

error bars for these transition strengths, which can be obtained by using the method presented in this work. The subsequent pair of ^{61}Ti-^{61}V is another potential cooling pair (with a QRPA prediction for the log ft value of 5.9), and should be also experimentally measured.

5.1 Urca cooling of neutron star crusts

It is important to consider the complete picture of Urca cooling in a crust consisting of X-ray burst ashes. Several methods have been used to identify potential Urca cooling pairs amongst the majority of nuclei where ground state to ground state transition strengths have not been measured experimentally. These include using Quasiparticle Random Phase Approximation (QRPA) calculations [25], and using typical measured ft value distributions [41] together with knowledge of ground state spins. The QRPA method has been shown to be less consistent with experimental measurements of ft values than shell-model based calculations [78, 79]. However, the usage of shell model-based calculations for β decay transition strengths is still limited to certain mass regions due to the prohibitive computational challenges associated with the large configuration spaces requires for heavier nuclei far from close shells. Here, we compare QRPA predictions with the latest state of experimental knowledge of log ft values and spins.

Fig. 5.2 shows the comparison of QRPA and a simple spin-based assessment of whether a ground state to ground state transition should be allowed and therefore strong. There are 114 cases where QRPA and spins provide compatible information: 47 cases where QRPA predicts a transition from the parent ground state to the daughter ground state (or an extremely low-lying state of below 30 keV) and the spins of the parent-daughter pair enable an allowed transition; and 87 cases where QRPA does not predict such a transition and the

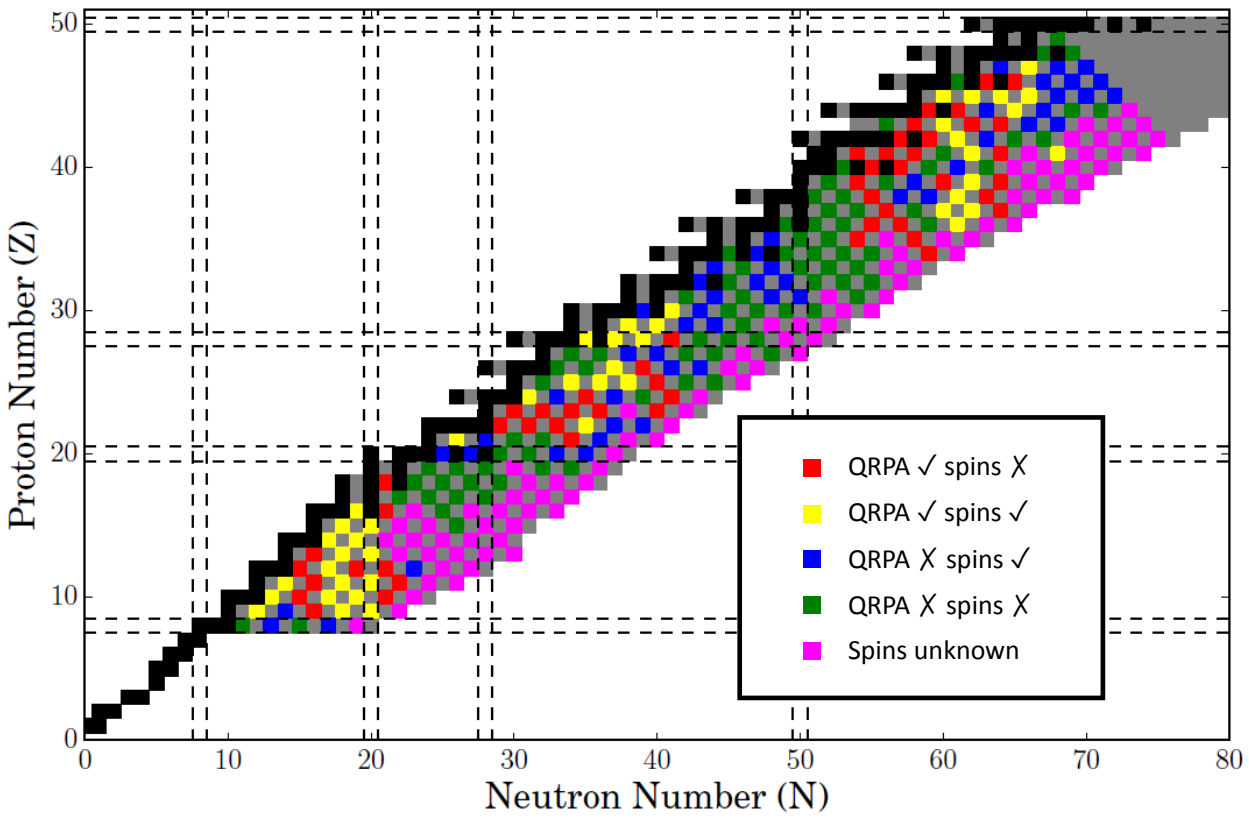

Figure 5.2: Chart of the nuclides (only odd-A nuclei are shown) showing the comparison between QRPA predictions for ground state transitions and whether allowed transitions are possible based on the experimentally-determined spins of the ground states. The red (yellow) squares denote nuclei where there is a QRPA-predicted transition and there is (is not) an allowed transition based on spins. The blue (green) squares denote nuclei where there is no QRPA-predicted transition and there is (is not) an allowed transition based on spins. Magenta squares denote nuclei where the spins have not yet been experimentally determined.

spins of the parent-daughter pair do not enable an allowed transition. There are 102 cases where QRPA and spins provide incompatible information: 50 cases where QRPA does not predict an allowed transition where the parent-daughter pair spins imply the likely existence of such a transition, and 52 cases where the opposite is true. Cases of disagreement are clustered in mid-shell regions, where QRPA typically predicts strong ground state to ground state transitions (red boxes in Fig 5.2) due to the larger nuclear deformation in these regions.

We update the list of Urca cooling chains from [22], where only QRPA calculations for

the allowed β decay and electron capture transitions were used. We follow the following prescription: (1) Experimental log ft values are used where they are available; (2) if the ground state spins of pairs of parent and daughter nuclei are known to enable an allowed transition (Δ J $\leq$ 1) and there is a QRPA prediction for the transition, then the QRPA prediction is used; (3) if the ground state spins of the pairs are known to enable an allowed transition and there is no QRPA prediction for the transition, then a ground state to ground state transition with a typical log $ft = 4.9$ is added (similar to [24]); (4) if the ground state spins of the pairs are known to forbid an allowed transition, the transition is removed regardless of whether there is a QRPA prediction or not; finally (5) if one (or both) of the spins in the pair is not known, then the QRPA prediction for whether the transition occurs is used. QRPA predictions of transitions to states with excitation energies of 30 keV or lower are treated as ground state transitions. This is to account for uncertainties in the QRPA energies or population by thermal excitation. Furthermore, even if the energies are correct, these extremely low-lying states can be significantly populated by β decays from the parent ground state at neutron star crust temperatures, and can therefore participate in Urca cycles.

To obtain a realistic estimate of the importance of various Urca cooling transitions, we calculated total heating or cooling in each mass chain independently and folded the result over a realistic crust composition with mass fractions $X(A)$, determined by thermonuclear burning near the surface of the neutron stars. Here we use the composition from the ashes of typcial mixed hydrogen and helium bursts from [80].

In the original calculations, the mass 61 chain was found to be one of the weaker cooling chains. However, newer calculations taking experimental information for the shallower cooling pairs into account suggest that it is still significant. Inclusion of the result from this

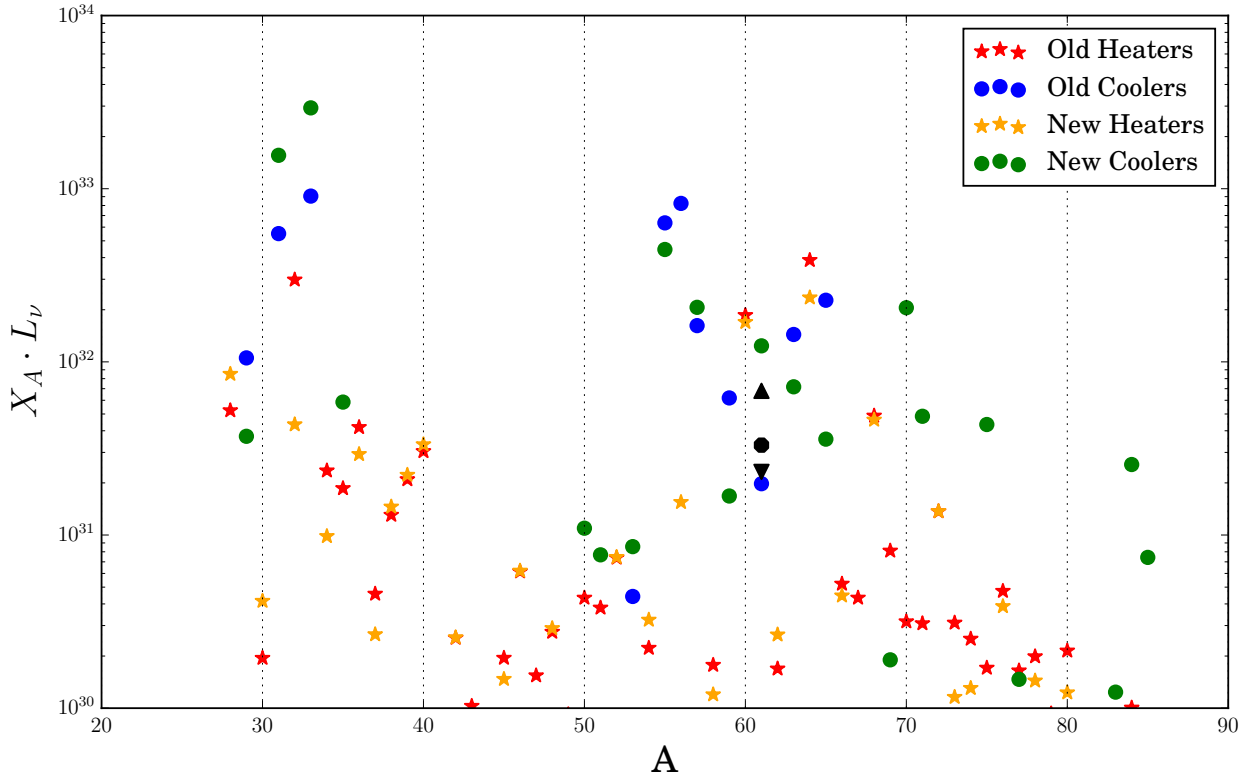

Figure 5.3: Cooling strengths of individual mass chains in X-ray burst ashes. 'Old' refers to the calculations presented in [22], and 'new' refers to the calculations done following the prescription described in the text, representing the state of experimental knowledge before the ^{61}V result. The new cooling strength of the mass 61 chain using the results of this experiment is given by the black octagon, with error bars (solely from the uncertainty in the ^{61}V decay strength) denoted by the up and down black triangles.

work somewhat mitigates this strength since the experimentally-determined log ft value of 5.5 is higher than the QRPA prediction of 4.35. Furthermore, many of the other transitions in strong cooling chains are either experimentally-unmeasured, or rely on experimental measurements likely heavily subject to the Pandemonium effect and maybe weaker than reported. Though the exact cooling strength depends the ash composition and therefore on the X-ray burst ignitition conditions (such as the composition of the accreted material), the abundances for the mass 50–80 region are likely to be the least condition-dependent.

Other important cooling chains for X-ray burst ashes are $A = 55$, 31 and 33. Of these,

the mass 33 chain is the most experimentally well-characterised, with β decay ground state to ground state measurements of log ft for ^{33}Na (5.2 [81]), ^{33}Mg (5.2, [82]),^{33}Al (4.3 [83]), and ^{33}Si (4.96 [83, 84]). The strongest cooling pair in the mass 31 chain is the ^{31}Na-^{31}Mg pair, with a measure log ft of 4.9 [85, 86]. The strengths of the $A = 31$ and $A = 33$ chains is highly dependent on the conditions of the X-ray burst. In scenarios the so-called extreme rp-process scenario, where there is an extended rp-process, there is very little abundance in the mass 30 region, drastically limiting the importance of the A = 31 and A = 33 chains for Urca cooling. The strength of the mass 55 chain, also extremely important for crusts made of superburst ashes [23], is almost entirely dependent on the strength of the unmeasured ^{55}Ca-^{55}Sc transition, by far the strongest cooling transition.

Chapter 6

Summary and Outlook

The experimental result presented in this work demonstrates that there is a non-negligible β-decay transition strength between the ground states of ^{61}V and ^{61}Cr of 7.4%, corresponding to a log ft value of 5.5. This is the first reporting of an ft value for a high Q-value β decay transition with realistic error bars. This result was achieved by using a combination of a high-efficiency neutron detection system and a total absorption spectrometer to mitigate the impact of the Pandemonium effect. The impact of the new measurement on the strength of Urca cooling by A = 61 ashes was investigated by incorporating the result into a reaction network calculation of a pure A = 61 neutron star crust. This revealed that the A = 61 mass chain is a moderately strong Urca cooling chain, though not one of the strongest.

However, within the errors of the ground state to ground state strength, there is still an order of magnitude uncertainty in the Urca luminosity, which casts doubt on the reliability of current predictions of Urca cooling in neutron star crusts based on measured log ft values where the Pandemonium effect may have systematically skewed the results. More experimental measurements of ground state to ground state transition strengths using the method developed in this work are required to bolster the effort towards understanding and properly quantifying the role of Urca cooling in cooling X-ray transients. With the implementation of this technique at the National Superconducting Cyclotron Laboratory, with its access to neutron-rich radioactive isotope beams, other exotic Urca pairs can be

investigated. For example, the A = 55 mass chain is predicted to be the strongest Urca cooling chain for superbursting systems [23], due to the strong ground state to ground state transition from ^{55}Ca to ^{55}Sc. A future experiment at NSCL utiilising the technique presented in this work to measure the ground state to ground state feeding of the β decay of ^{55}Ca will be conducted to determine if Urca cooling is effective in superbursting X-ray transients.

REFERENCES

REFERENCES

[1] Edward F Brown, Lars Bildsten, and Robert E Rutledge. Crustal heating and quiescent emission from transiently accreting neutron stars. The Astrophysical Journal Letters, 504(2):L95, 1998.

[2] S. Campana, M. Colpi, S. Mereghetti, L. Stella, and M. Tavani. The neutron stars of Soft X-ray Transients. Astronomy and Astrophysics Reviews, 8:279–316, 1998.

[3] Duncan K Galloway, Michael P Muno, Jacob M Hartman, Dimitrios Psaltis, and Deepto Chakrabarty. Thermonuclear (type I) X-ray bursts observed by the rossi X-ray timing explorer. The Astrophysical Journal Supplement Series, 179(2):360, 2008.

[4] RK Wallace and SoE Woosley. Explosive hydrogen burning. The Astrophysical Journal Supplement Series, 45:389–420, 1981.

[5] Hendrik Schatz, A Aprahamian, et al. End point of the rp process on accreting neutron stars. Physical review letters, 86(16):3471, 2001.

[6] ME Caplan and CJ Horowitz. Colloquium: Astromaterial science and nuclear pasta. Reviews of Modern Physics, 89(4):041002, 2017.

[7] Christiane Beyer and Dustin Figueroa. Design and analysis of lattice structures for additive manufacturing. Journal of Manufacturing Science and Engineering, 138(12):121014, 2016.

[8] E. F. Brown and A. Cumming. Mapping Crustal Heating with the Cooling Light Curves of Quasi-Persistent Transients. The Astrophysical Journal, 698:1020–1032, June 2009.

[9] Alex Deibel, Andrew Cumming, Edward F Brown, and Dany Page. A strong shallow heat source in the accreting neutron star MAXI J0556-332. The Astrophysical Journal Letters, 809(2):L31, 2015.

[10] Andrew Cumming and Lars Bildsten. Carbon flashes in the heavy-element ocean on accreting neutron stars. The Astrophysical Journal Letters, 559(2):L127, 2001.

[11] Andrew Cumming, Jared Macbeth, Dany Page, et al. Long type i x-ray bursts and neutron star interior physics. The Astrophysical Journal, 646(1):429, 2006.

[12] Andrew Cumming and Jared Macbeth. The thermal evolution following a superburst on an accreting neutron star. The Astrophysical Journal Letters, 603(1):L37, 2004.

[13] Edward F. Brown. Nuclear heating and melted layers in the inner crust of an accreting neutron star. The Astrophysical Journal, 531(2):988, 2000.

[14] Sanjib Gupta, Edward F. Brown, Hendrik Schatz, Peter Moller, and Karl-Ludwig Kratz. Heating in the accreted neutron star ocean: Implications for superburst ignition. The Astrophysical Journal, 662(2):1188, 2007.

[15] D. G. Yakovlev, K. P. Levenfish, and O. Y. Gnedin. Pycnonuclear reactions in dense stellar matter. European Physical Journal A Supplement, 25:669–672, September 2005.

[16] N Degenaar, R Wijnands, et al. Neutron star crust cooling in the terzan 5 x-ray transient swift j174805. 3–244637. Monthly Notices of the Royal Astronomical Society, 451(2):2071–2081, 2015.

[17] Rachael L Merritt, Edward M Cackett, et al. The thermal state of ks 1731-260 after 14.5 years in quiescence. The Astrophysical Journal, 833(2):186, 2016.

[18] Anthony L Piro and Lars Bildsten. Turbulent mixing in the surface layers of accreting neutron stars. The Astrophysical Journal, 663(2):1252, 2007.

[19] F. J. Fattoyev, E. F. Brown, et al. Deep Crustal Heating by Neutrinos from the Surface of Accreting Neutron Stars. ArXiv e-prints, October 2017.

[20] George Gamow and Mario Schoenberg. Neutrino theory of stellar collapse. Physical Review, 59(7):539, 1941.

[21] M. B. Aufderheide, I. Fushiki, G. M. Fuller, and T. A. Weaver. A new URCA process. The Astrophysical Journal, 424:257–262, March 1994.

[22] H. Schatz, S. Gupta, et al. Strong neutrino cooling by cycles of electron capture and β^- decay in neutron star crusts. Nature, 505:62–65, January 2014.

[23] Alex Deibel, Zach Meisel, Hendrik Schatz, Edward F Brown, and Andrew Cumming. Urca cooling pairs in the neutron star ocean and their effect on superbursts. The Astrophysical Journal, 831(1):13, 2016.

[24] Zach Meisel and Alex Deibel. Constraints on bygone nucleosynthesis of accreting neutron stars. The Astrophysical Journal, 837(1):73, 2017.

[25] Peter Möller and Jørgen Randrup. New developments in the calculation of β-strength functions. Nuclear Physics A, 514(1):1–48, 1990.

[26] H. L. Crawford, P. F. Mantica, et al. Low-energy structure of ^{61}Mn populated following β decay of ^{61}Cr. Phys. Rev. C, 79:054320, May 2009.

[27] D. Radulov, C. J. Chiara, et al. β decay of ^{61}mn to levels in ^{61}fe. Phys. Rev. C, 88:014307, Jul 2013.

[28] D. Ehrlich. Der Radioaktive Zerfall des Fe^{61}. Z.Phys., 207:268, 1967.

[29] Kazimierz Zuber and Balraj Singh. Nuclear Data Sheets for A = 61. Nuclear Data Sheets, 125(Supplement C):1 – 200, 2015.

[30] MG Van der Merwe, WA Richter, and BA Brown. Effective interactions for A= 41-66 nuclei. Nuclear Physics A, 579(1-2):173–196, 1994.

[31] G Audi, FG Kondev, et al. The nubase2012 evaluation of nuclear properties. Chinese Physics C, 36(12):1157, 2012.

[32] N Hoteling, WB Walters, et al. Rotation-aligned coupling in fe 61. Physical Review C, 77(4):044314, 2008.

[33] Morten Hjorth-Jensen, Thomas TS Kuo, and Eivind Osnes. Realistic effective interactions for nuclear systems. Physics Reports, 261(3-4):125–270, 1995.

[34] WA Richter, MG Van der Merwe, and BA Brown. Shell-model calculations for neutron-rich nuclei in the 0f1p shell. Nuclear Physics A, 586(3):445–456, 1995.

[35] Hua Jin, Yang Sun, Kazunari Kaneko, Shigeru Tazaki, et al. Shell model description with neutron g 9/2 excitation for neutron-rich 57-62 mn isotopes. Physical Review C, 87(4):044327, 2013.

[36] S. Suchyta, S. N. Liddick, et al. β decay of ^{61,63}V and low-energy level schemes of ^{61,63}Cr. Phys. Rev. C, 89:034317, Mar 2014.

[37] MB Bennett, C Wrede, et al. Classical-nova contribution to the milky way's al 26 abundance: Exit channel of the key al 25 (p, γ) si 26 resonance. Physical review letters, 111(23):232503, 2013.

[38] Georges Audi, O Bersillon, J Blachot, and AH Wapstra. The nubase evaluation of nuclear and decay properties. Nuclear physics A, 729(1):3–128, 2003.

[39] M Graefenstedt, U Keyser, et al. Nuclear structure effects in the mass region around a= 100, derived from experimental q β-values. Zeitschrift für Physik A Hadrons and Nuclei, 327(4):383–392, 1987.

[40] Enrico Fermi. An attempt of a theory of beta radiation. 1. Z. Phys., 88(UCRL-TRANS-726):161–177, 1934.

[41] B Singh, JL Rodriguez, SSM Wong, and JK Tuli. Review of logftvalues in β decay. Nuclear Data Sheets, 84(3):487–563, 1998.

[42] Harry Bateman. The solution of a system of differential equations occurring in the theory of radioactive transformations. In Proc. Cambridge Philos. Soc, volume 15, pages 423–427, 1910.

[43] Jerzy Cetnar. General solution of Bateman equations for nuclear transmutations. Annals of Nuclear Energy, 33(7):640 – 645, 2006.

[44] J. C. Hardy, L. C. Carraz, B. Jonson, and P. G. Hansen. The essential decay of pandemonium: A demonstration of errors in complex beta-decay schemes. Physics Letters B, 71:307–310, November 1977.

[45] O.B. Tarasov and D. Bazin. LISE++: Exotic beam production with fragment separators and their design. Nuclear Instruments and Methods in Physics Research Section B: Beam Interactions with Materials and Atoms, 376(Supplement C):185 – 187, 2016. Proceedings of the XVIIth International Conference on Electromagnetic Isotope Separators and Related Topics (EMIS2015), Grand Rapids, MI, U.S.A., 11-15 May 2015.

[46] D ˙ J Morrissey, BM Sherrill, M Steiner, A Stolz, and I Wiedenhoever. Commissioning the a1900 projectile fragment separator. Nuclear Instruments and Methods in Physics Research Section B: Beam Interactions with Materials and Atoms, 204:90–96, 2003.

[47] A Stolz, T Baumann, et al. Production of rare isotope beams with the nscl fragment separator. Nuclear Instruments and Methods in Physics Research Section B: Beam Interactions with Materials and Atoms, 241(1-4):858–861, 2005.

[48] J. Pereira, P. Hosmer, et al. The neutron long counter NERO for studies of β-delayed neutron emission in the r-process. Nuclear Instruments and Methods in Physics Research A, 618:275–283, June 2010.

[49] JI Prisciandaro, AC Morton, and PF Mantica. Beta counting system for fast fragmentation beams. Nuclear Instruments and Methods in Physics Research Section A: Accelerators, Spectrometers, Detectors and Associated Equipment, 505(1):140–143, 2003.

[50] Clemens Herlitzius. Improvement of the Neutron Emission Ratio Observer by an Active Cosmic Ray Shield. Master's thesis, Michigan State University, East Lansing, Michigan, USA, 2008.

[51] Judith F Briesmeister et al. Mcnptm- a general monte carlo n-particle transport code. Version 4C, LA-13709-M, Los Alamos National Laboratory, page 2, 2000.

[52] A. Simon, S.J. Quinn, et al. SuN: Summing NaI(Tl) gamma-ray detector for capture reaction measurements. Nuclear Instruments and Methods in Physics Research Section A: Accelerators, Spectrometers, Detectors and Associated Equipment, 703(Supplement C):16 – 21, 2013.

[53] Arjan Koning, Stephane Hilaire, and Stephane Goriely. Talys-1.6 a nuclear reaction program. User Manual (NRG, The Netherlands), First Edition: December, 23:2013, 2013.

[54] K Starosta, C Vaman, et al. Digital data acquisition system for experiments with segmented detectors at national superconducting cyclotron laboratory. Nuclear Instruments and Methods in Physics Research Section A: Accelerators, Spectrometers, Detectors and Associated Equipment, 610(3):700–709, 2009.

[55] CJ Prokop, SN Liddick, et al. Digital data acquisition system implementation at the national superconducting cyclotron laboratory. Nuclear Instruments and Methods in Physics Research Section A: Accelerators, Spectrometers, Detectors and Associated Equipment, 741:163–168, 2014.

[56] P. T. Hosmer. Beta-decay studies of nickel-78 and other neutron-rich nuclei in the astrophysical r-process. PhD thesis, Michigan State University, Michigan, USA, 2005.

[57] J. Pereira, S. Hennrich, et al. β-decay half-lives and β-delayed neutron emission probabilities of nuclei in the region A$<\approx$ 110, relevant for the r process. Physical Review C, 79(3):035806, March 2009.

[58] A.D. Carlson, V.G. Pronyaev, et al. International Evaluation of Neutron Cross Section Standards. Nuclear Data Sheets, 110(12):3215 – 3324, 2009. Special Issue on Nuclear Reaction Data.

[59] Karl-Heinz Schmidt, Beatriz Jurado, and Charlotte Amouroux. "general description of fission observables - gef model". Nuclear Data Sheets, 131, 06 2014.

[60] L. Ruby and J.B. Rechen. A simpler approach to the geometrical efficiency of a parallel-disk source and detector system. Nuclear Instruments and Methods, 58(2):345 – 346, 1968.

[61] S. J. Quinn. Capture cross sections for the astrophysical p process. PhD thesis, Michigan State University, 2015.

[62] F Montes. Beta decay studies in neutron rich Tc, Ru, Rh and Pd isotopes and the weak r-process. PhD thesis, Michigan State University, Michigan, USA, 2005.

[63] S. Agostinelli, J. Allison, et al. Geant4—a simulation toolkit. Nuclear Instruments and Methods in Physics Research Section A: Accelerators, Spectrometers, Detectors and Associated Equipment, 506(3):250 – 303, 2003.

[64] A. C. Dombos, D.-L. Fang, et al. Total absorption spectroscopy of the β decay of ^{76}Ga. Phys. Rev. C, 93:064317, Jun 2016.

[65] Meng Wang, G. Audi, et al. The ame2016 atomic mass evaluation (ii). tables, graphs and references. Chinese Physics C, 41(3):030003, 2017.

[66] M. Karny, K.P. Rykaczewski, et al. Modular total absorption spectrometer. Nuclear Instruments and Methods in Physics Research Section A: Accelerators, Spectrometers, Detectors and Associated Equipment, 836(Supplement C):83 – 90, 2016.

[67] F. Bečvář. Simulation of γ cascades in complex nuclei with emphasis on assessment of uncertainties of cascade-related quantities. Nuclear Instruments and Methods in Physics Research Section A: Accelerators, Spectrometers, Detectors and Associated Equipment, 417(2):434 – 449, 1998.

[68] F. James and M. Roos. Minuit - a system for function minimization and analysis of the parameter errors and correlations. Computer Physics Communications, 10(6):343 – 367, 1975.

[69] Rene Brun and Fons Rademakers. ROOT — An object oriented data analysis framework. Nuclear Instruments and Methods in Physics Research Section A: Accelerators, Spectrometers, Detectors and Associated Equipment, 389(1):81 – 86, 1997. New Computing Techniques in Physics Research V.

[70] I. Antcheva, M. Ballintijn, et al. ROOT — a C++ framework for petabyte data storage, statistical analysis and visualization. Computer Physics Communications, 180(12):2499 – 2512, 2009. 40 YEARS OF CPC: A celebratory issue focused on quality software for high performance, grid and novel computing architectures.

[71] P. MÖLLER, J.R. NIX, and K.-L. KRATZ. Nuclear Properties for Astrophysical and Radioactive Ion-Beam Applications. Atomic Data and Nuclear Data Tables, 66(2):131 – 343, 1997.

[72] Peter Moeller, Bernd Pfeiffer, and Karl-Ludwig Kratz. New calculations of gross β-decay properties for astrophysical applications: Speeding-up the classical r process. Physical Review. C, Nuclear Physics, 67(5):055802–055802, 2003.

[73] O. Sorlin, C. Donzaud, et al. Beta decay half-lives of neutron rich Ti–Co isotopes around N=40. Nuclear Physics A, 660(1):3 – 19, 1999.

[74] O. Sorlin, C. Donzaud, et al. New region of deformation in the neutron-rich ^{60}Cr and ^{62}Cr. The European Physical Journal A - Hadrons and Nuclei, 16(1):55–61, Jan 2003.

[75] L. Gaudefroy, O. Sorlin, et al. Beta-decay studies of neutron-rich Sc- Cr nuclei. The European Physical Journal A - Hadrons and Nuclei, 23(1):41–48, Jan 2005.

[76] J. M. Daugas, I. Matea, et al. β-decay measurements for N > 40 Mn nuclei and inference of collectivity for neutron-rich Fe isotopes. Phys. Rev. C, 83:054312, May 2011.

[77] I. Matea. Decroissance β et moments magnetiques comme outils pour sonder la structure nucleaire. Etude des noyaux riches en neutrons autour de N=40. PhD thesis, Universite de Caen, France, 2002.

[78] A. Cole, T. S. Anderson, et al. Comparing Experimental and Calculated Electron-capture Rates of pf-shell Nuclei in Explosive Stellar Environments. In Nuclei in the Cosmos (NIC XII), page 98, 2012.

[79] A. L. Cole, T. S. Anderson, et al. Gamow-Teller strengths and electron-capture rates for pf-shell nuclei of relevance for late stellar evolution. Physical Review C, 86(1):015809, July 2012.

[80] RH Cyburt, AM Amthor, et al. Dependence of x-ray burst models on nuclear reaction rates. The Astrophysical Journal, 830(2):55, 2016.

[81] S. Nummela, F. Nowacki, et al. Intruder features in the island of inversion: The case of ^{33}Mg. Phys. Rev. C, 64:054313, Oct 2001.

[82] Vandana Tripathi, S. L. Tabor, et al. Intruder configurations in the $a = 33$ isobars: ^{33}Mg and ^{33}Al. Phys. Rev. Lett., 101:142504, Oct 2008.

[83] A.C Morton, P.F Mantica, et al. Beta decay studies of nuclei near 32Mg: Investigating the ν(f7/2)–(d3/2) inversion at the N=20 shell closure. Physics Letters B, 544(3):274 – 279, 2002.

[84] D. R. Goosman, C. N. Davids, and D. E. Alburger. Accurate masses and β-decay schemes for ^{34}P and ^{33}Si. Phys. Rev. C, 8:1324–1330, Oct 1973.

[85] D. Guillemaud-Mueller, C. Detraz, et al. β-Decay schemes of very neutron-rich sodium isotopes and their descendants. Nuclear Physics A, 426(1):37 – 76, 1984.

[86] G. Klotz, P. Baumann, et al. Beta decay of ^{31,32}Na and ^{31}Mg: Study of the n=20 shell closure. Phys. Rev. C, 47:2502–2516, Jun 1993.